Mechanics of Electrodes in Lithium-Ion Batteries

Thesis Advisors
Zhigang Suo, Joost J. Vlassak

Author
Kejie Zhao

Mechanics of Electrodes in Lithium-ion Batteries

Abstract

This thesis investigates the mechanical behavior of electrodes in Li-ion batteries. Each electrode in a Li-ion battery consists of host atoms and guest atoms (Li atoms). The host atoms form a framework, into which Li atoms are inserted via chemical reactions. During charge and discharge, the amount of Li in the electrode varies substantially, and the host framework deforms. The deformation induces in an electrode a field of stress, which may lead to fracture or morphological change. Such mechanical degradation over lithiation cycles can cause the capacity to fade substantially in a commercial battery.

We study fracture of elastic electrodes caused by fast charging using a combination of diffusion kinetics and fracture mechanics. A theory is outlined to investigate how material properties, electrode particle size, and charging rate affect fracture of electrodes in Li-ion batteries. We model an inelastic host of Li by considering diffusion, elastic-plastic deformation, and fracture. The model shows that fracture is averted for a small and soft host—an inelastic host of a small feature size and low yield strength.

We present a model of concurrent reaction and plasticity during lithiation of crystalline silicon electrodes. It accounts for observed lithiated silicon of anisotropic

morphologies. We further explore the microscopic deformation mechanism of lithiated silicon based on first-principles calculations. We attribute to the microscopic mechanism of large plastic deformation to continuous Li-assisted breaking and reforming of Si-Si bonds. In addition, we model the evolution of the biaxial stress in an amorphous Si thin film electrode during lithiation cycle. We find that both the atomic insertion driven by the chemomechanical load and plasticity driven by the mechanical load contribute to reactive flow of lithiated silicon. In such concurrent process, the lithiation reaction promotes plastic deformation by lowering the stress needed to flow.

Li-ion battery is an emerging field that couples electrochemistry and mechanics. This thesis aims to understand the deformation mechanism, stresses and fracture associated with the lithiation reaction in Li-ion batteries, and hopes to provide insight on the generic phenomenon that involves interactive chemical reactions and mechanics.

Table of Contents

List of Figures

List of Tables

Acknowledgements

At the moment my thesis comes into final shape, I am looking back on my four years life at Harvard and feeling so lucky to have so many great teachers and friends around. They stimulate my interest, refresh my mind, and inspire wonderful ideas in my research. The completion of my thesis is accompanied with enormous help from them.

First I wish to bring my heartiest gratitude to my supervisor Professor Zhigang Suo. Zhigang is a gracious, enthusiastic and illuminative mentor. He generously admitted me into my dream school Harvard and guided me into research with enormous patience especially in my first year. Zhigang is always supportive on any research interest of students. Just to mention a few examples; Zhigang gave me unlimited freedom exploring new questions in batteries even I am finically supported by another project; He always shows excitement and encouragement in our conversations of regular meetings, although most of time my progress is consciously trivial; Once some good ideas are initiated Zhigang is willing to spend a lot of time to help me work them out – it is so unforgettable on the 10 days of intensive work on our second paper and 2 weeks of our third paper. Zhigang's vast knowledge in mechanics and materials and deep insight have inspired the entire path of my research. I was educated in three courses of Zhigang; I have found those classes most enlightening in my personal experience, by Zhigang's deep understanding of materials, intuitive illustrations and fabulous lecturing style. I also admire that Zhigang devotes

most of school time on teaching; a good teacher is crucially influential to students. In my research career, my supervisor sets the model and target.

I also wish to bring my deep gratitude to my thesis co-advisor Professor Joost J. Vlassak. I have vastly benefitted from discussions with Joost in our regular meetings. All of my research work has been advised by Joost with invaluable suggestions and feedback. Joost is a meticulous scholar; his critical way of thinking shapes my research. Joost also taught me elementary experimental mechanics which will be beneficial in my research career.

I am deeply grateful to Professor Efthimios Kaxiras who taught me skills of atomistic simulations. Prof. Kaxiras always has deep yet intuitive physical insight on problems. His drawing of local atomic structures and their effects on mechanical behavior at the macroscopic level has been very enlightening. Prof. Kaxiras extended my knowledge from continuum mechanics to the atomic level, and urged me to understand the underlying mechanisms behind the mechanical behavior of materials. I also appreciate his willingness to spend a lot of time guiding my research. It was my great pleasure to coauthor a few papers with Prof. Kaxiras.

Deep appreciation is due to other thesis committee professors, Professor David Clarke and Professor Katia Bertoldi, for their helpful suggestions and comments at various stages of my research. Their interest and appreciation gave me confidence to carry on this research. I also really appreciate considerate suggestions of the committee on the time schedule of my defense exam.

Special thanks to my buddy Matt Pharr. Matt has been my close partner in the

four years. Both of us are involved in each other's research. I am pleased to coauthor all my papers with him. Matt is a critical and high-standard researcher. His criticism often renews our ideas and stimulates more interesting questions. Furthermore, Matt has been my English teacher. His careful proof of our papers makes them correct and smooth. The supportive and persistent work of Matt brings my research coherently assembled.

I was fortunate to have many other wonderful collaborators, Dr. Weili Wang, Dr. John Gregoire, Dr. Laurence Brassart, Dr. Qiang Wan, Dr. Shengqiang Cai, Dr. Georgios Tritsaris, Lauren Hartle at Harvard, and Dr. Jianyu Huang at Sandia National Lab. Weili has taught me a lot of detailed skills of atomistic simulations. He is also a great friend; it's always pleased to talk with him. Dr. Jianyu Huang is very enthusiastic friend. He has done tremendous beautiful work on In-situ TEM experiments of Li-ion batteries. I really appreciate that he is willing to collaborate with us. All other collaborators have helped to shape my research. Their comments and feedbacks have been very valuable.

The research group of Zhigang is a wonderful family. Every person in our group is easy-going and willing to help each other. I am so glad to be immersed in such a friendly and relaxed atmosphere. I thank all these great friends, Dr. Nanshu Lu, Dr. Xuanhe Zhao, Dr. Yuhang Hu, Dr. Shengqiang Cai, Dr. Jian Zhu, Dr. Jeong-Yun Sun, Dr. Keith Choon Chiang Foo, Dr. Jiangshui Huang, Dr, Christoph Keplinger, Dr. Laurance Brassart, Lihua Jin, Widusha Illeperuma, Qihan Liu, Chao Chen, Tongqing Lu, Jiawei Yang, Pengfei Wang, Dr. Qiang Wan, Dr. Liwu Liu, Dr. Huiming Wang, Dr.

Xiangfeng Liang, Tiefeng Li, Dr. Xingzhe Wang, Dr. Hongzhong Liu and Dr. Shaoxing Qu.

Deepest love is due to my beloved family. I am grateful to my Dad and Mom; like most parents, they are persistently supportive to me and proud of me. Most importantly, I heartily appreciate my wife who came to the US with huge sacrifice. Without her support and encouragement, my thesis would never have been accomplished. My dear wife and little baby girl are always the sweetest part of my heart.

Chapter 1

Introduction

The first chapter introduces the working principles of Li-ion batteries, and outlines the structure of this thesis. Energy storage is a crucial aspect of integrating renewable energy sources in power grids, making the development of efficient high-capacity batteries an important technological challenge.[1], [2] A battery is composed of several electrochemical cells that are connected in series and/or in parallel to provide the required voltage and capacity, respectively.[3] Each cell consists of a positive and a negative electrode separated by an electrolyte solution containing dissociated salts, which enable ion transfer between the two electrodes. Once these electrodes are connected externally by conducting wires, chemical reactions proceed in both electrodes. The amount of electrical energy, expressed either per unit of weight (Wh kg^{-1}) or per unit of volume (W h l^{-1}), that a battery is able to deliver is a function of the cell potential and capacity. Among the various existing technologies, Figure 1. 1, Li-based batteries currently outperforms other systems, because of their high energy density and design flexibility.[4]

For applications that are sensitive to weight and size, such as the portable, entertainment, computing and telecommunication equipment, Li-ion batteries are the current industry standard.[5], [6] Furthermore, batteries have been identified as a key technology for a clean and secure energy future.[1], [2] Companies worldwide are racing to develop Li-ion batteries for electric cars. Battery-powered cars, plugged into an

increasingly green grid, would reduce pollution and secure energy independence, while maintaining individual mobility. A system of distributed batteries and a smart electric grid would accommodate the unpredictable nature of renewable energy sources (e.g., wind and solar), allowing energy to be stored during times of low demand, and then be drawn back to meet peak demand.[7]

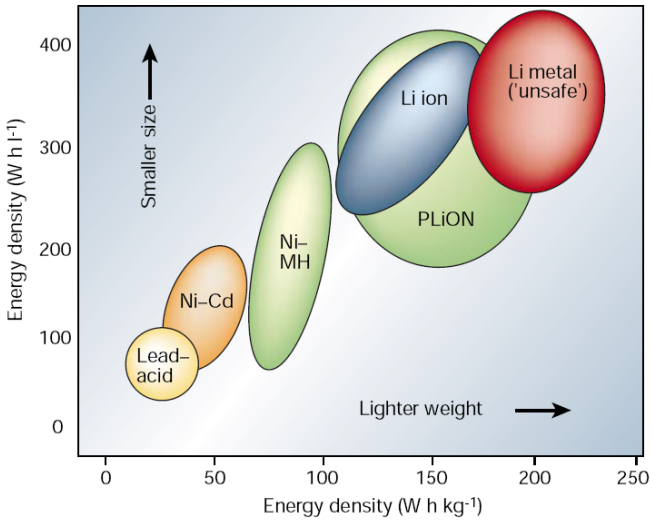

Figure 1.1. Comparison of various battery technologies in terms of volumetric and gravimetric energy density. The share of worldwide sales for Ni-Cd, Ni-MeH and Li-ion portable batteries is 23, 14, 63%, respectively.[4]

1.1 Basics of Li-ion batteries

In a Li-ion battery, it converts energy between two forms, chemical and electrical. Li can diffuse into and react with nearly all materials. A material that conducts electrons may in principle serve as an electrode. When two different electrodes are in direct contact, Li atoms diffuse from the electrode with a high chemical potential of Li (i.e., the negative electrode) to the electrode with a low chemical potential of Li (i.e., the positive electrode). The two electrodes are separated by an electrolyte, a material that conducts Li-ions but not electrons. When the battery discharges (Figure 1. 2),

the difference in the chemical potential of Li in the two electrodes drives Li-ions to diffuse out of the negative electrode, through the electrolyte, and into the positive electrode. To keep the electrodes electrically neutral, electrons flow through an external circuit from the negative to the positive electrode. Both the ionic and the electronic processes are reversed when the battery is charged by an external power source.

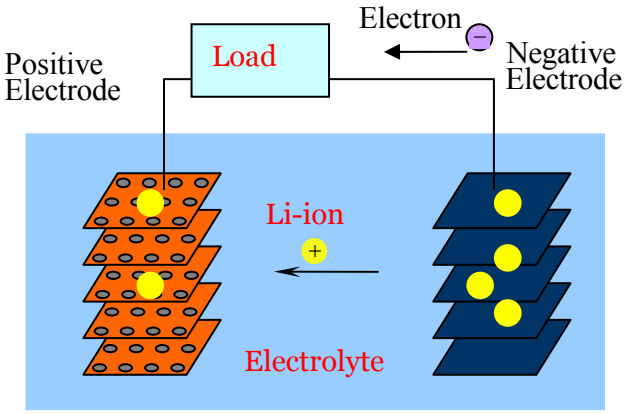

Figure 1.2. Schematics of a Li-ion battery during discharge.

1.1.1 Thermodynamics

The energy storage and power characteristics of batteries follow directly the thermodynamic and kinetic formulations for chemical reactions.[8] The basic thermodynamics for a reversible electrochemical reaction is given by

$$\Delta G = \Delta H - T\Delta S\,, \tag{1.1}$$

where ΔG is the Gibbs free energy, or the available energy in a reaction for the useful work, ΔH is the enthalpy, or the energy released by the reaction, ΔS is the entropy, and T is the absolute temperature, with $T\Delta S$ being the heat associated with the reaction. The terms ΔG, ΔH and ΔS are state functions and depend only on the

identity of the electrode materials and the initial and final states of the reactions.

The free energy ΔG represents the net useful energy available from a given reaction, thus, the net available electrical energy from a reaction in a battery cell is given by

$$\Delta G = -nFE \tag{1.2}$$

where n is the number of electrons transferred per mol of reactants, F is the Faraday constant, and E is the voltage of the cell with the specific chemical reaction. Eq. (1.2) represents a balance between the chemical and electric driving forces upon the ions under open circuit conditions, hence E refers to the open circuit potential of a cell where there is no current flowing. The voltage of the cell is unique for each reaction couple. In other words, if the electrolyte is a perfect filter that allows the passage of ionic species, but no electrons, the cell voltage is determined by the difference in the electrically neutral chemical compositions of the electrodes. The identity and properties of the electrolyte and the phenomena that occur at the electrode/electrolyte interfaces play no role. The amount of electricity produced, nF, is determined by the total amount of materials available for reactions and can be thought of as a capacity factor; the voltage can be considered to be an intensity factor.[3]

The change of free energy for a given species i defines the chemical potential. The chemical potential μ_i for species i is related to another thermodynamic quantity, the activity a_i, by the defining relation

$$\mu_i = \mu_i^0 + RT \ln a_i \tag{1.3}$$

where μ_i^0 is a constant, the value of the chemical potential of species i in its standard state. R is the gas constant, and T the absolute temperature. Consider an electrochemical cell in which the activity of species i is different in the two electrodes, $a_i(-)$ in the negative electrode, and $a_i(+)$ in the positive electrode. The difference between the chemical potential on the positive side and that on the negative side is written as $\mu_i(+) - \mu_i(-) = RT \ln\left[a_i(+)/a_i(-)\right]$. If this chemical potential difference is balanced by the electrostatic energy from Eq. (1.2), we have

$$E = -\frac{RT}{nF} \ln\left[\frac{a_i(+)}{a_i(-)}\right]. \tag{1.4}$$

The above relation is the Nernst equation, which relates the measurable cell voltage to the chemical difference across an electrochemical cell. If the activity of species i in one of the electrodes is a standard reference value, the Nernst equation provides the relative electrical potential of the other electrode.[8]

1.1.2 Kinetics

Thermodynamics described reactions at equilibrium and the maximum energy available for a given reaction. Compared to the open circuit potential at equilibrium state, the voltage drops off when current is drawn from the battery because of kinetic limitations of reactions. Figure 1. 3 shows a typical discharge curve of a battery.[3], [9] Electrochemical reaction kinetics follows the general considerations as those for bulk chemical reactions. However, the detailed mechanism of battery electrode reactions often involves a series of physical, chemical, and electrochemical steps, including charge-transfer and charge transport reactions. The rates of these individual steps

determine the kinetics of the electrode. Basically, three different kinetics effects for polarization are often considered: (1) activation polarization is related to the kinetics of the electrochemical redox (or charge-transfer) reactions taking place at the electrode/electrolyte interfaces of anode and cathode; (2) ohmic polarization is correlated to the resistance of individual cell components and to the resistance due to contact problems between the cell components; (3) concentration polarization is due to mass transport limitations during cell operation.[9]

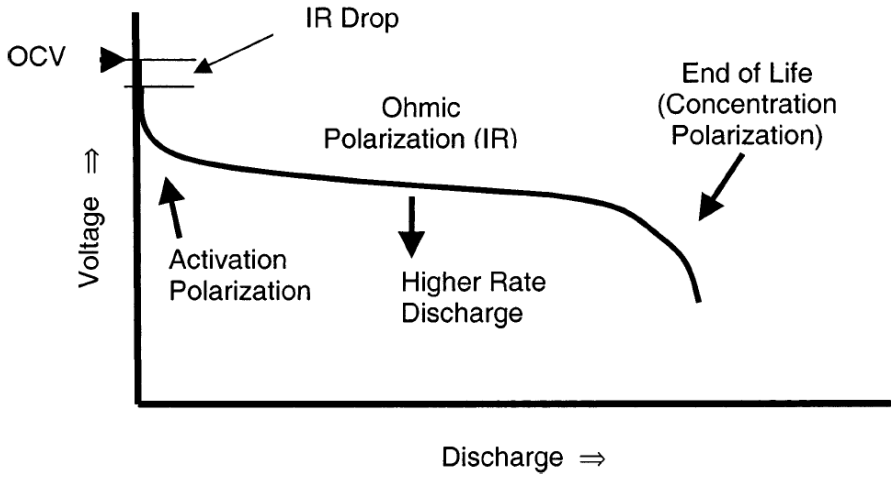

Figure 1.3. A typical discharge curve of a battery. [3]

Activation polarization arises from kinetics of the charge-transfer reaction taking place at the electrode/electrolyte interface. This type of kinetics is best understood using transition-state theory. The current flow is often described by the Butler-Volmer equation. Ohmic polarization arises from the resistance of the electrolyte, materials of constructions of the electrodes, current collectors, terminals and contact between particles of the active mass. Ohmic polarization appears or disappears instantaneously when current flows or ceases. Typically the linear Ohm's law relates the current and potential. As the redox reactions proceed, the availability

of the active species at the electrode/electrolyte interface changes. Concentrations polarization arises from limited mass transport capabilities, for example, limited diffusion of active species to and from the electrode surface to replace the reacted material to sustain the reactions. This type of polarization usually becomes the rate-limiting step at the completion of charge/discharge.

1.2 Coupling electrochemistry and mechanics in Li-ion batteries

At the heart of a Li-ion battery is a problem coupling electrochemistry and mechanics. Each electrode consists of host atoms and guest atoms (Li atoms). The host atoms form a framework, into which Li atoms are inserted.[8] During charge and discharge, the amount of Li in the electrode varies substantially, and the host framework deforms. The insertion-induced deformation in electrodes has significant consequences in Li-ion batteries.[10]-[14] The deformation is often constrained under various conditions, such as crystalline grains of different orientations, a transient distribution of Li, mismatch between active and inactive materials, etc.[15], [16] Under such constraints, insertion of Li induces in an electrode a field of stress, which may lead to fracture (Figure 1. 4)[17]-[19] or morphological change (Figure 1. 5).[20], [21] Such mechanical degradation is a significant mechanism that over charge/discharge cycles can cause the capacity of a battery to fade.[22] While insertion-induced deformation is usually taken to be elastic, the observation of large morphological change clearly indicates that charge/discharge cycles can cause inelastic deformation.

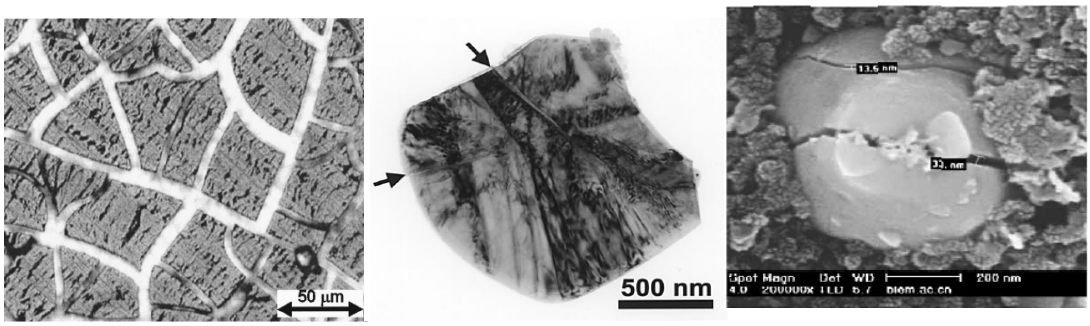

(a) SiSn thin film (b) $LiCoO_2$ particle (c) $LiFePO_4$ particle

Figure 1.4. (a) SiSn thin film is cracked after the first few cycles of lithiation and delithiation.[17] (b) Microfracture in a $LiCoO_2$ particle after 50 cycles.[18] (c) A $LiFePO_4$ particle is cracked into parts after 60 cycles.[19]

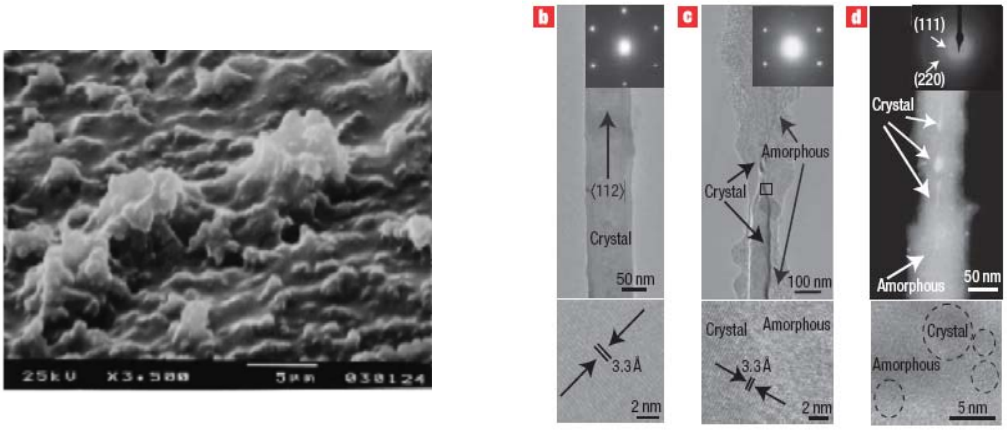

(a) Amorphous Si thin film (b) Crystalline Si nanowire

Figure 1.5. (a) An initially flat amorphous Si thin film electrode develops surface undulation after 1000 cycles of lithiation and delithiation.[20] (b) Crystalline Si nanowires change the surface morphology during cycles.[21]

Furthermore, insertion-induced deformation places a limit on the choice of materials for future high-density batteries.[23][25] For example, the negative electrodes in commercial Li-ion batteries today are graphite, where every six carbon atoms accommodate one Li atom. By comparison, every Si atom accommodates 4.4 Li atoms in theory. While the large capacity for Si to absorb Li has motivated intense research, such absorption causes volumetric swelling of about 400%, leading to fracture and morphological change (Figure 1. 5). Likewise, mechanics significantly

influences the chemistry of lithiation in a Li-ion battery. The mechanical energy contributes to the free energy associated with the reaction. In particular, the effect of stress on chemistry is pronounced, examples include the reactions at the interface of electrode/electrolyte,[26] the diffusion of Li in active material particles,[27] and phase transformations of the electrodes.[28]

The technology of batteries is in a state of flux: new materials, new configurations, and new applications constantly emerge. Challenges to the technology of batteries have been traditionally understood in terms of electrochemistry of materials and economics of applications. While these understandings will continue to be important, it has become increasingly evident that a complementary understanding of how electrodes sustain insertion-induced deformation without degradation holds a great promise for future high-density batteries.

1.3 The goal and outline of this thesis

The goal of this thesis is to understand the deformation mechanism, stress and fracture of electrodes in Li-ion batteries. It is organized as follows. Chapter 2 studies fracture of elastic electrodes caused by fast charging using a combination of diffusion kinetics and fracture mechanics. A theory is outlined to investigate how material properties, electrode particle size, and charge/discharge rate affect fracture of electrodes in Li-ion batteries. Chapter 2 introduces inelastic hosts for high-capacity electrodes. We model such an inelastic host of Li by considering diffusion,

elastic-plastic deformation, and fracture. Chapter 4 formulates a theory that couples lithiation and large elastic-plastic deformation, and analyzes the homogeneous lithiation and deformation in a small material element using non-equilibrium thermodynamics. Through a numerical example of a spherical particle subject to a constant rate of Li insertion, we explore the effect of plastic yielding, stress on the lithiation reaction, and charging rates. Chapter 5 and 6 considers two promising designs of nanostructured Si anodes. Stress fields in these structures are calculated and mechanical failure caused by fracture and debonding is discussed. Chapter 7 studies lithiation mechanism of crystalline Si. A model of concurrent lithiation reaction and plastic deformation is developed. Chapter 9 and 10 explore the deformation mechanism of plasticity based on first-principles computational methods. The plastic deformation of lithiated silicon is attributed to Li-assisted breaking and reformation of Si-Si bonds. Furthermore, reactive flow of lithiated silicon is simulated. The lithiation reaction promotes plastic deformation by lowering the stress needed to flow.

Chapter 2

Fracture of elastic electrodes by fast charging

2.1 Introduction

Batteries are a key to the commercialization of clean and secure energy.[1], [2] Essential roles of batteries include leveling loads on power grids and storing energy from renewable sources. Furthermore, batteries are ubiquitous in all forms of electronics and transportation. For applications sensitive to weight and size, such as portable electronics and electric cars, the technology of choice is Li-ion batteries.[29]

A Li-ion battery contains an electrolyte and two electrodes. Each electrode is an atomic framework that hosts mobile Li. During charging or discharging of the battery, Li ions are extracted from one electrode, migrate through the electrolyte, and are then inserted into the other electrode. Meanwhile electrons flow from one electrode to the other through an external metallic wire. Extraction or insertion of Li induces in the electrodes stresses that may cause fracture[10] or morphological change.[22] The loss of structural integrity may reduce electric conductance, causing the capacity of the battery to fade.

Lithiation-induced damage is a bottleneck in developing batteries of high energy density. For example, the ability of silicon to absorb a large amount of lithium has motivated intense research,[23] but such absorption causes volumetric swelling of ~400%, leading to fracture. The mechanical failure has so far prevented silicon

from serving as a viable electrode. Fracture has also been observed in commercial electrodes that undergo small deformation, such as $LiCoO_2$, $LiMn_2O_4$ and $LiFePO_4$.[30]-[33]

Lithiation-induced deformation and stress have been studied in recent years. For example, Christensen and Newman calculated swelling and stress,[12], [13] Sastry and co-workers simulated the stress generation during lithiation under galvanostatic control,[14] Cheng and co-workers calculated the strain energy under both potentiostatic and galvanostatic operations in spherical particles.[34], [35] Lithiation-induced stress in silicon has been calculated.[36], [37] Several recent papers have studied lithiation-induced fracture by applying fracture mechanics.[15], [39][41]

While a conceptual framework to analyze lithiation-induced deformation, stress and fracture is emerging, limited work has been published that predicts fracture of practical systems by using actual material data. This paper attempts to predict fracture in a widely used material for cathode, $LiCoO_2$. A commercial electrode often takes the form of active particles embedded in a binding matrix (Figure 2. 1). The distribution of Li in the particle is inhomogeneous. The gradient of this inhomogeneity is large if the battery is charged at a rate faster than Li can homogenize in the particle by diffusion. We calculate the distributions of Li and stress in a $LiCoO_2$ particle, and then calculate the energy release rates for the particle containing preexisting cracks. These calculations predict the critical rate of charging and size of the particle, below which fracture is averted.

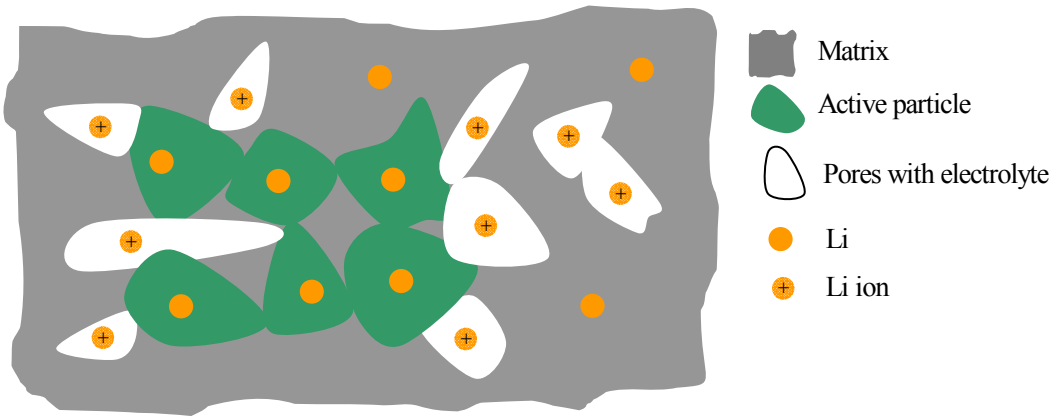

Figure 2. 1. A schematic of the microstructure of the cathode. The cathode is composed of active particles, a matrix, and pores containing the electrolyte.

2.2 Theory and scaling

In a battery, the electrolyte conducts Li ions but not electrons. When the battery discharges, the difference in the chemical potential of Li in the two electrodes drives Li ions to diffuse out of the anode, through the electrolyte, and into the cathode. To keep the electrodes electrically neutral, electrons flow from the anode to the cathode through the external metallic wire. Both the ionic and the electronic processes are reversed when the battery is charged by an external power source. As illustrated in Figure 2. 1, an electrode in commercial Li-ion batteries is usually a composite, consisting of active particles, a matrix composed of polymer binders and additives, and pores filled with the electrolyte.[33] Migration of Li in the electrolyte is fast, so that diffusion of Li in the active particles limits the rate of charging and discharging. Because of the porosity of the composite and the compliance of the binder, stress in an active particle is often due primarily to the mismatch created by an inhomogeneous distribution of Li within the particle.

The degree of the inhomogeneity depends on the competition between the rate of discharging and the rate of diffusion. Denote τ as the time to discharge the battery, D a representative value of diffusivity of Li in the particle, and L the characteristic size of the particle. These quantities form a dimensionless group:

$$\chi = \frac{L}{\sqrt{D\tau}} \tag{2.1}$$

The parameter χ measures the relative rate of discharging and diffusion. If χ is large, the battery is discharged at a rate faster than Li can homogenize in the particle by diffusion. Consequently, Li is crowded in the outer shell of the particle, causing a large stress in the particle (Figure 2.2 (a)). By contrast, if χ is small, the battery is discharged at a rate slow enough for Li in the particle to maintain nearly a homogeneous distribution. Consequently, lithiation causes the particle to swell or contract, but the particle is nearly unstressed (Figure 2.2 (b)).

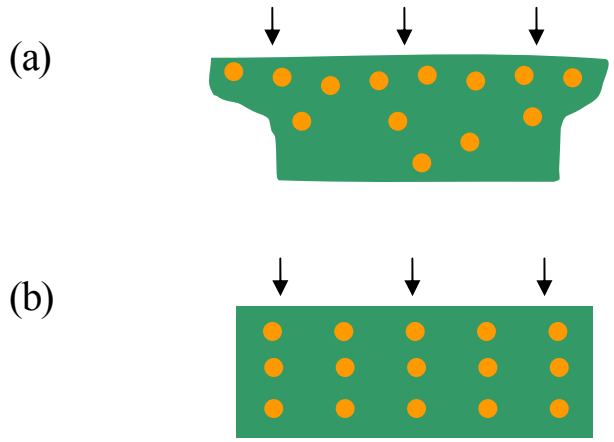

Figure 2. 2. (a) When the rate of discharging is high, the distribution of Li in the active particle is inhomogeneous, which causes a field of stress in the particle. (b) When the rate of discharging is low, the distribution of Li in the particle is nearly homogenous, and the magnitude of the stress in the particle is negligible. The arrows indicate the direction of Li insertion.

Crack-like flaws are assumed to preexist in the active particles.[33] We ask if the lithiation-induced stress will cause any of the flaws to grow. The elastic energy in the particle reduces when a crack advances. The reduction of the elastic energy in the particle associated with the crack advancing a unit area defines the energy release rate G. Dimensional considerations dictate that the energy release rate should take the form

$$G = ZE\varepsilon_m^2 L, \tag{2.2}$$

where E is Young's modulus of the particle, L a characteristic size of the particle, and ε_m a characteristic mismatch strain, defined as

$$\varepsilon_m = \frac{l_1 - l_0}{l_0} \tag{2.3}$$

Here l_0 and l_1 are the lattice parameters in the initial state and in the fully lithiated state, respectively. At a given time, the distribution of the stress in the particle is determined by solving the diffusion equation, and the dimensionless coefficient Z is determined by solving the elastic boundary-value problem. Once the geometry of the particle and the location of the crack are given, Z can only vary with the length of the crack, the dimensionless parameter χ, and time. We note this functional dependence in a normalized form:

$$Z = f\left(\frac{a}{L}, \chi, \frac{t}{\tau}\right), \tag{2.4}$$

where a denotes the length of the crack. Figure 2. 3 is a schematic of the energy release rate as a function of the length of the crack at a fixed value of χ and a fixed time. When the crack is very short, the elastic energy in the particle does not change

appreciably when the crack grows, and the energy release rate is small. Likewise, when the crack is very long, the elastic energy is nearly fully relaxed because the crack introduces larger constraint-free area, and the energy release rate is also small. In between these two limits, the energy release rate reaches the maximum value $G_{\max}$ for a crack of a certain length. Let Γ be the fracture energy of the particle. No preexisting flaws will advance if the maximum energy release rate is below the fracture energy of the particle

$$G_{\max} < \Gamma . \tag{2.5}$$

To ensure no preexisting flaws will advance, $G_{\max}$ stands for the energy release rate maximized for all configurations of the flaws and for all time. This approach has been used to analyze many systems, such as polycrystals,[42] composites,[43] and thin films.[44]

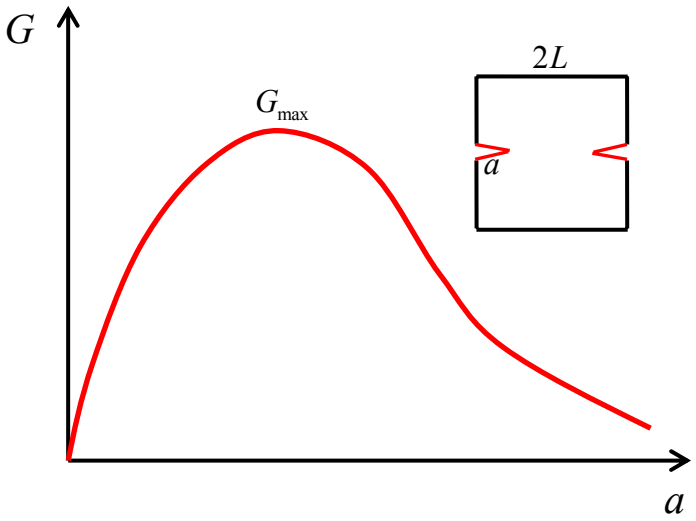

Figure 2. 3. Trend of the energy release rate as a function of the length of preexisting cracks for a fixed discharge rate.

The comparison between the energy release rate and the fracture energy defines another dimensionless parameter

$$\Lambda = \frac{E\varepsilon_m^2 L}{\Gamma}. \tag{2.6}$$

When Λ is small, the elastic energy is insufficient to cause fracture. Therefore, a particle with small stiffness, small size, and large fracture energy is more resistant to fracture. This statement is consistent with recent experimental observation that the electrochemical cycling behavior is significantly improved if the size of active particles is small.[45], [46]

The dimensionless groups χ and Λ characterize the fracture behavior of the active particles. In the case of a highly inhomogeneous distribution of Li ions, to prevent fracture it is necessary to decrease the particle size, decrease the rate of discharging, and/or enhance the fracture energy. This concept is sketched schematically in Figure 2. 4 in terms of χ and Λ. The red line delineates an upper boundary to the safe regime in which no fracture occurs.

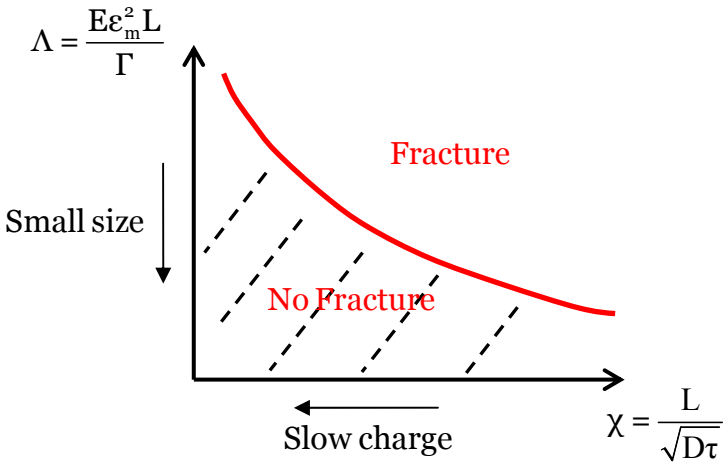

Figure 2. 4. Criteria to avoid fracture of an electrode particle in terms of the non-dimensional quantities Λ and χ.

2.3 Numerical results for $LiCoO_2$

Following the above theory, we perform calculations for a $LiCoO_2$ particle. As illustrated in Figure 2. 5 (a), $LiCoO_2$ has a layered crystalline structure, where oxygen ions form close-packed planes in an ABCABC sequence, and cobalt and Li ions occupy alternating layers of octahedral sites between the oxygen layers. Li diffuses in the plane perpendicular to z axis. The oxygen ions cause repulsion between the neighboring layers. These oxygen layers are attracted to the Li atoms inserted between them. Thus, during discharge the insertion of the Li ions decreases the repulsion between the CoO2 sheets and leads to a volume contraction of ~2% .[47] The lattice parameter dependence on Li concentration is shown in Figure 2. 5 (b).

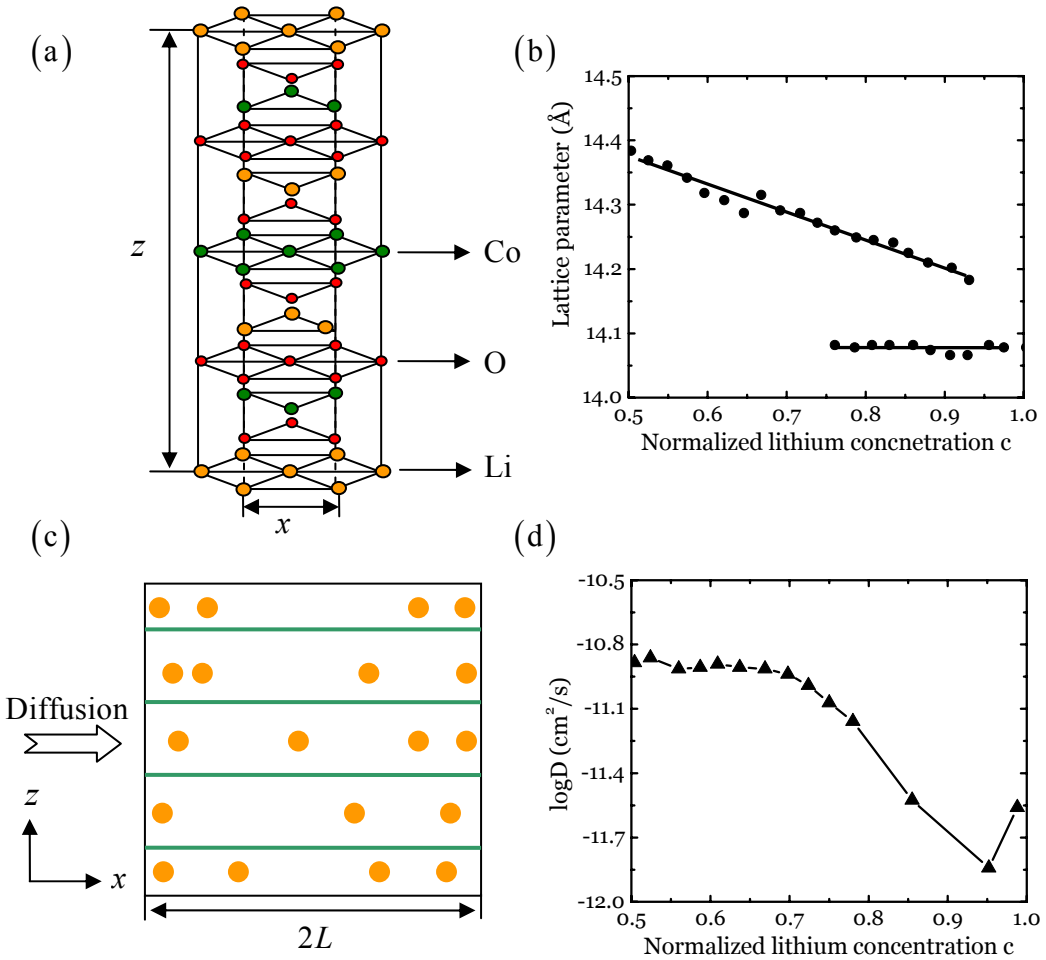

Figure 2. 5. (a) The layered structure of LiCoO2. (b) Variation of lattice parameter along the z axis with normalized Li concentration (Reproduced from reference [47]). The lattice

Figure 2.5 (Continued) parameter along the axis is nearly a constant. (c) 1D diffusion model used in the numerical simulation. Li diffusion is along the axis, towards the center of the particle. (d) The Li diffusivity as a function of the normalized Li concentration (Reproduced from reference [48]).

In practical applications, the size of a $LiCoO_2$ electrode particle is on the order of microns or smaller. At such a small scale, the particle is often a single crystal or at most consists of a few grains.[18] In the numerical simulation, the electrode is assumed to be a single crystal with a 2D geometry. Li ions only diffuse along the x axis. The model is shown in Figure 2. 5 (c), in which L characterizes the particle size. The diffusion of Li in the particle is governed by the partial differential equation

$$\frac{\partial c}{\partial t} = \nabla \cdot \left[D(c) \nabla c \right], \tag{2.7}$$

where c denotes the normalized Li concentration in the host–the actual Li concentration divided by the concentration of Li in the fully lithiated state, $LiCoO_2$. In practice, the working regime for lithium cobalt oxide is in the range of $0.5 \le c \le 1$. Experiments show that the diffusivity D decreases one order of magnitude when the normalized Li concentration increases from 0.5 to 1.[48] Here we reproduce the experimental diffusivity dependence on Li concentration in Figure 2. 5 (d). In the simulation we have allowed the diffusivity to vary with concentration, a dependence that is usually neglected in other works. Note that the concentration gradient serves as the primary driving force for diffusion. The stress effect has been explored in reference,[14] the concentration difference due to the stress effect, which is at maximum around 7%, is negligible for fracture analysis.

The initial and boundary conditions are given by

$$
\begin{aligned}
&t = 0; && c{=}0.5 \\
&x = 0;\ t > 0 && \frac{\partial c}{\partial x} = 0 \\
&x = L;\ t > 0 && -D(c)\nabla c = \text{constant}
\end{aligned}
\tag{2.8}
$$

The constant in Eq. (2.8) is given by the discharge current density under galvanostatic (constant current) operation. Thus, in the simulation the discharge rate is controlled by changing the flux constant. Discharge is completed once the normalized concentration of Li at the outside surface reaches a value of unity. The concentration profile of Li inside the particle is obtained by solving the diffusion equation in COMSOL Multiphysics.

Figure 2. 6 (a) and Figure 2. 6 (b) show the distributions of Li at several times, at discharge rates of 0.5C and 2C respectively. Here the discharge rates are reported in the C-rate convention given by C/τ, where the value of τ is calculated as the theoretical capacity (~140 mAh/g) divided by the discharge current. It is evident from the figures that, in both cases, the Li concentration gradient increases with discharge time. This behavior is a direct consequence of the decrease in effective diffusivity with increasing Li content (See Figure 2. 5 (d)). As the discharge rate increases from 0.5C to of 2C, the Li distribution inside the host particle becomes less homogeneous, in agreement with the schematics in Figure 2. 2.

This inhomogeneous distribution of Li results in a large deformation mismatch. The strain along *z* direction (see Figure 2. 5 (a)) in the host particle is given by

$$
\varepsilon = \frac{l(c) - l_0}{l_0} \tag{2.9}
$$

where $l(c)$ is the lattice parameter at a given Li concentration, l_0 is the lattice

parameter at the initial normalized Li concentration c = 0.5. Here we use the experimental values for the $LiCoO_2$ lattice parameter as a function of concentration to calculate the strain.[47] The inhomogeneous distribution of Li leads to a non-uniform strain field inside the particle and thus a stress field in the particle.

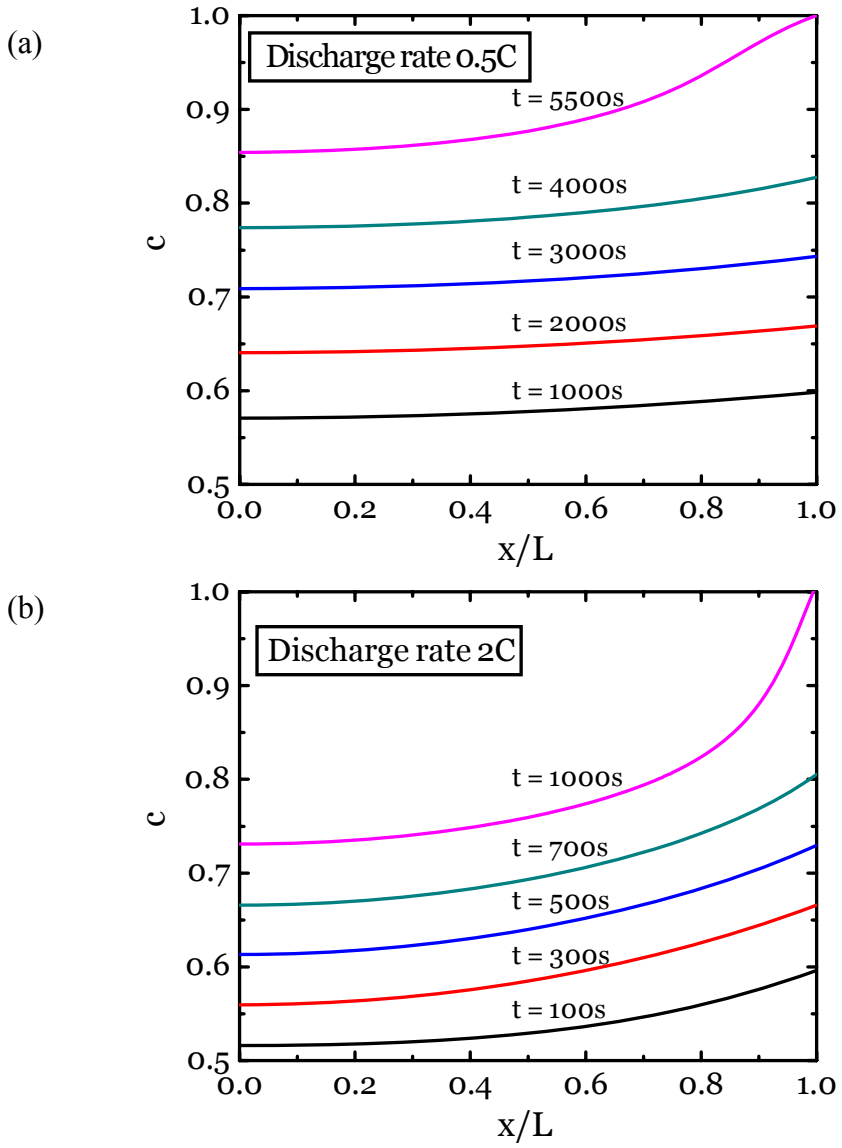

Figure 2. 6. Li distribution with time for a $LiCoO_2$ particle at (a) discharge rate of 0.5C, (b) discharge rate of 2C. Here $x/L=0$ represents the center of the particle, and $x/L=1$ represents the outside surface.

The stress field is calculated by solving the elastic boundary value problem. Since

deformation is much faster than diffusion, mechanical equilibrium is established during lithiation. Traction-free boundary conditions are prescribed. The boundary value problem is solved with the finite element software ABAQUS. An orthotropic material model is employed with stiffness coefficients taken from atomistic simulations.[49] The input strain field is simulated by imposing a thermal strain, equal to the concentration induced mismatch strain; the stress field is obtained as the output. In this configuration, the stress component σ_{zz} is the tensile stress responsible for the crack propagation. Figure 2. 7 (a) and Figure 2. 7 (b) plot the internal mismatch strains and the normalized stress distributions as a function of the dimensionless distance at discharge rates of 0.5C and 2C, respectively. We represent E as $C_{22} = 375\text{GPa}$ used for the normalization. It can be seen that the outer shell (near $x/L = 1$) of the particle is under tension, while the core (near $x/L = 0$) is under compression during Li insertion. The tensile stress in the outer shell may drive a preexisting crack to grow. The driving force is much larger for the faster discharge of rate 2C because of the highly inhomogeneous distribution of Li.

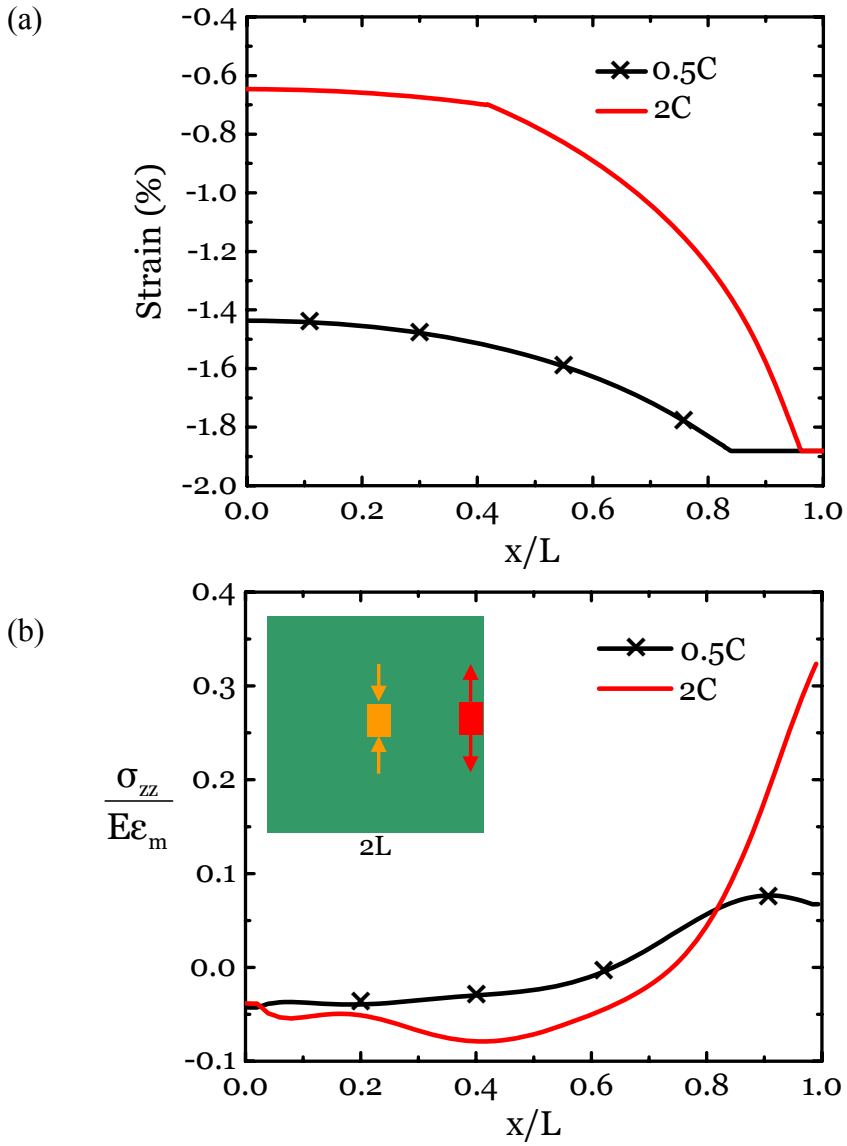

Figure 2. 7. (a) Mismatch strain profile (b) Normalized stress distribution at various discharge rates when the normalized Li concentration at the outer surface reaches unity. The center of the particle is under compression, and the outside surface is under tension.

To calculate the energy release rate, a crack of length a is assumed to preexist inside the particle. In the simulation, we fix the particle size and the location of the preexisting crack, and we vary the preexisting crack length and discharge rate. In each case, we use the stress distribution at the end of discharge. The J-integral is used to calculate the energy release rate. Figure 2. 8 gives the normalized energy release rate dependence on the crack length to the particle size ratio, for discharge

rates of 2C, 4C and 6C. The energy release rates are maximized at normalized lengths of 0.11, 0.09 and 0.07, respectively.

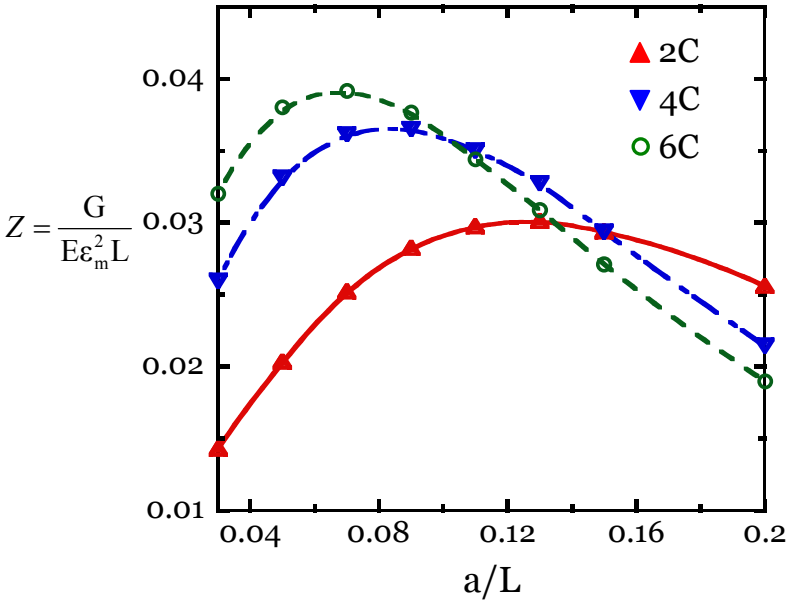

Figure 2. 8. Energy release rate as a function of crack size at various discharge rates.

As pointed out in section II, no preexisting crack can advance if the maximum energy release rate is smaller than the fracture energy. This condition defines a critical particle size

$$L_c = \frac{\Gamma}{Z_{\max} E \varepsilon_m^2}, \tag{2.10}$$

where Z is found from Figure 2. 8. When the particle is smaller than the critical value, no preexisting crack in the particle can advance. The critical particle size as a function of discharge rate is illustrated in Figure 2. 9. Here we have used approximate fracture energy of 1 J/m^2 for $LiCoO_2$. From the figure, decreasing the electrode particle size can effectively prevent fracture during fast charging.

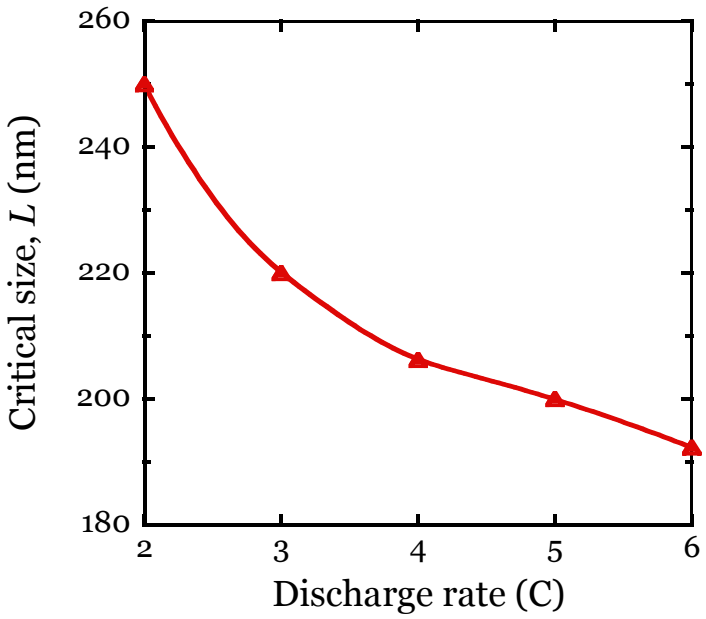

Figure 2. 9. Critical $LiCoO_2$ particle size to avoid crack propagation as a function of discharge rate.

Experimental observations of cracked $LiCoO_2$ particles in the literature are limited. Crack damage is reported for an average particle size of 300~500nm after 50 cycles.[18] The model presented here shows that fracture can be prevented by decreasing the electrode particle size and/or discharge rate. To further test the accuracy of the model, more data for fracture of particles of different sizes and for a range of discharge rates are needed. Finally, it should be noted we used stiffness coefficients derived from atomistic simulations and estimated fracture energy to calculate the critical particle size. These values may vary with Li concentration,[50] and should be ascertained by further experiments.

2.4 Summary

Using a combination of diffusion kinetics and fracture mechanics, we have outlined a theory to study how material properties, particle size, and discharge rate

affect fracture of electrodes in Li-ion batteries. We characterize the discharge rate relative to diffusion rate by a dimensionless parameter χ. We characterize the magnitude of the elastic energy relative to the fracture energy by a dimensionless parameter Λ. A "fracture map," demonstrating criteria for fracture, can be constructed in terms of the non-dimensional parameters Λ and χ. To illustrate the theory, a numerical example of a $LiCoO_2$ particle is presented. We calculate the distribution of Li and stress at different discharge rates. We also calculate the energy release rates for preexisting flaws of different sizes. When the maximum energy release rate is smaller than the fracture energy, no pre-existing cracks can advance. This approach enables us to calculate the critical particle size and discharge rate necessary to avoid fracture.

Chapter 3

Inelastic hosts as high-capacity electrodes

3.1 Introduction

In Li-ion batteries, lithiation-induced deformation and fracture is a bottleneck in developing batteries of high capacity. For example, of all known materials for anodes, silicon offers the highest theoretical specific capacity—each Si atom can host up to 4.4 Li atoms. By comparison, in commercial anodes of graphite, every six carbon atoms can host up to one Li atom. Silicon is not used in anodes in commercial Li-ion batteries, mainly because after a small number of cycles the capacity fades, often attributed to lithiation-induced deformation and fracture.[17]

Recent experiments, however, have shown that the capacity can be maintained over many cycles for silicon anodes of small feature sizes, such as nanowires,[21] thin films,[20] and porous structures.[51] When silicon is fully lithiated, the volume of the material swells by ~300%. For anodes of small feature sizes, evidence has accumulated that this lithiation-induced strain can be accommodated by inelastic deformation. For instance, cyclic lithiation causes silicon thin films and silicon nanowires to develop undulations. [20], [21] Furthermore, the stress in a silicon thin film bonded on a wafer has been measured during charge and discharge, showing that the film deforms plastically upon reaching a yield strength.[52]

Existing models of lithiation-induced deformation and fracture have assumed that the electrodes are elastic.[11]-[15], [34]-[41] Here we model inelastic electrodes by

considering diffusion, elastic-plastic deformation, and fracture. The model shows that fracture is averted for a small and soft host of lithium—an inelastic host of a small feature size and low yield strength.

3.2 Elastic and inelastic hosts of lithium

We classify hosts of Li into two types: elastic and inelastic. For an elastic host, the host atoms recover their configurations after cycles of charge and discharge (Figure 3. 1 (a)). For example, for an electrode of a layered structure, within each layer the host atoms form strong bonds, while neighboring layers are held together by weak bonds. Li diffuses in the plane between the layers, leaving the strong bonds within each layer intact. Elastic hosts are used in commercial Li-ion batteries for both cathodes (e.g., $LiCoO_2$) and anodes (e.g., graphite). By contrast, an inelastic host does not fully recover its structure after cycles of charge and discharge (Figure 3. 1 (b)). For example, when an electrode is an amorphous solid, such as amorphous silicon, the host atoms may change neighbors after a cycle of charge and discharge.

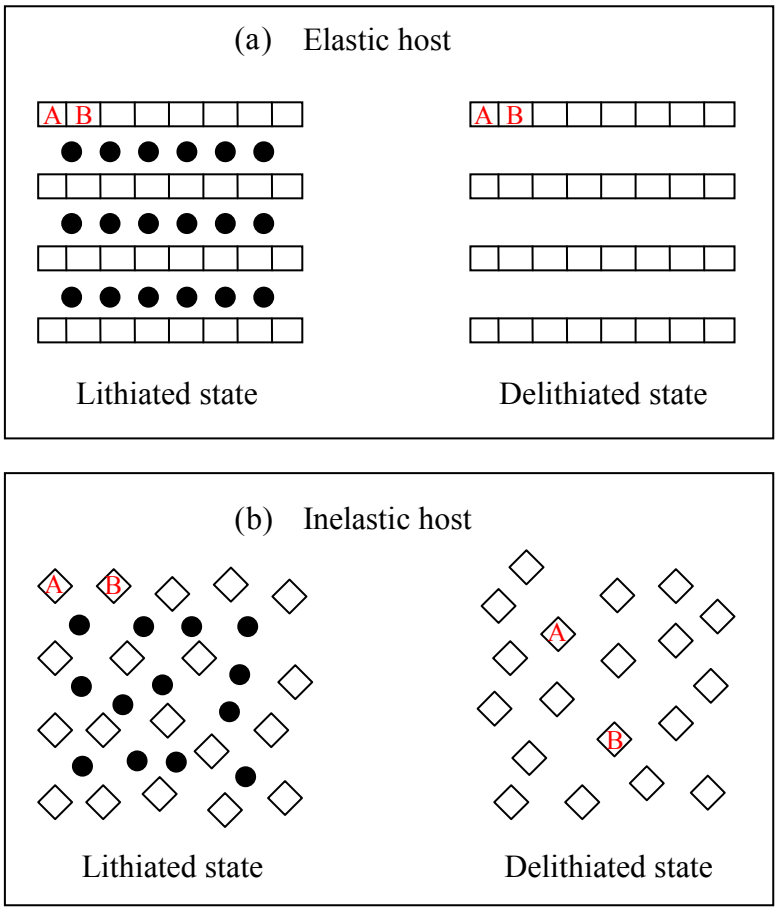

Figure 3. 1. (a) For an elastic host of Li, the host atoms recover their configurations after a cycle of lithiation. (b) For an inelastic host of Li, the host atoms may change neighbors after a cycle of lithiation. Squares represent host atoms, and circles represent Li atoms.

Whether lithiation-induced strain will cause an electrode to fracture depends on the feature size of the electrode.[10] The energy release rate G for a crack in a body of a small feature size takes the form $G = Z\sigma^2 h / E$, where h is the feature size, E Young's modulus, σ a representative stress in the body, and Z a dimensionless number of order unity.[19] Fracture is averted if G is below the fracture energy of the material, Γ. Consequently, fracture is averted if the feature size is below the critical value

$$h_c = \frac{\Gamma E}{Z\sigma^2} \tag{3.1}$$

Representative values for silicon are $\Gamma = 10$ J/m^2 and $E = 80$ GPa .[53]

If silicon were an elastic host, the lithiation-induced strain $\varepsilon = 100\%$ would cause stress on the order $\sigma \sim E\varepsilon$. Eq. (3. 1) would predict a subatomic critical size. This prediction disagrees with the experimental observations—silicon anodes of feature sizes around 100 nm do survive many cycles of charge and discharge without fracture.[20]

By contrast, for an inelastic host, lithiation-induced strain can be accommodated by inelastic deformation, and the stress scales with the yield strength. For a thin film of silicon bonded on a thick substrate, the measured yield strength is $\sigma_Y = 1.75$ GPa .[52] For a channel crack in the film, Z = 2 is a typical value.[44] Using these values, Eq. (3. 1) predicts a critical thickness of 130 nm. This prediction agrees well with available experimental observations: a 250 nm silicon thin film fractured after a few cycles,[54] while a 50 nm silicon film survived without fractures after 1000 cycles.[20] In general, for an inelastic electrode of a large capacity, fracture is averted if the feature size is small and the yield strength is low. One extreme is a liquid electrode, which accommodates the absorption-induced strain by flow, and can potentially provide ultra high capacity.[55]-[57]

During charge and discharge, the stress in an electrode is a time-dependent field. Furthermore, the magnitude of the stress may exceed the yield strength at places under triaxial constraint. To explore these effects, we describe an inelastic host of Li by adapting an elastic and perfectly plastic model.[58] The increment of the strain is defined by $d\varepsilon_{ij} = \left(du_{i,j} + du_{j,i}\right)/2$, where du_i is the increment of the displacement. The stress σ_{ij} satisfies the equilibrium equation, $\sigma_{ij,j} = 0$. The increment of the

strain is taken to be the sum of three contributions:

$$d\varepsilon_{ij} = d\varepsilon_{ij}^{e} + d\varepsilon_{ij}^{p} + d\varepsilon_{ij}^{l}, \tag{3.2}$$

where ε_{ij}^{e} is the elastic strain, ε_{ij}^{p} the plastic strain, and ε_{ij}^{l} the lithiation-induced strain. The elastic strain obeys Hooke's law:

$$d\varepsilon_{ij}^{e} = d\left(\frac{1}{E}\left[(1+\nu)\sigma_{ij} - \nu\sigma_{kk}\delta_{ij}\right]\right), \tag{3.3}$$

where ν is Poisson's ratio. $\delta_{ij} = 1$ when $i = j$, and $\delta_{ij} = 0$ otherwise. The increment of the plastic strain obeys the J_2-flow rule:

$$d\varepsilon_{ij}^{p} = \begin{cases} 0, & \sigma_e < \sigma_Y \\ 0, & \sigma_e = \sigma_Y,\ d\sigma_e < d\sigma_Y \\ \lambda s_{ij}, & \sigma_e = \sigma_Y,\ d\sigma_e = d\sigma_Y \end{cases}, \tag{3.4}$$

where $s_{ij} = \sigma_{ij} - \sigma_{kk}\delta_{ij}/3$ is the deviatoric stress and $\sigma_e = \sqrt{3s_{ij}s_{ij}/2}$ the equivalent stress. Within the perfectly plastic model, λ at each increment is a positive scalar to be determined by the boundary-value problem. The yield strength σ_Y can be a function of the concentration of Li. The lithiation-induced strain is proportional to the concentration of Li:

$$d\varepsilon_{ij}^{l} = d\left(\frac{\beta c}{3}\right)\delta_{ij}, \tag{3.5}$$

where β is a constant analogous to the coefficient of thermal expansion, and c denotes the normalized Li concentration in the host–the actual Li concentration divided by the concentration of Li in the fully lithiated state.

The concentration of Li in an electrode is a time-dependent field, taken to be governed by the diffusion equation, $\partial c/\partial t = D\nabla^2 c$. For simplicity, here we assume that the diffusivity D is a constant independent of the concentration and stress, and

that diffusion is driven by the gradient of concentration alone.

As an illustration of the model, consider a thin film of amorphous silicon bonded on a substrate. Let h be the thickness of the film, and τ the time used to complete charge or discharge. We consider the limit $h << \sqrt{D\tau}$, where the film is so thin that the concentration of Li is homogeneous throughout the thickness of the film. The stresses in the film are given by $\sigma_{xx} = \sigma_{yy} = \sigma, \quad \sigma_{zz} = 0$, where x and y represent the in-plane directions, and z represents the out-of-plane direction. The magnitude of the stress σ is homogenous in the film, but varies during the progression of lithiation. The increment of the elastic strain is $d\varepsilon^e_{xx} = d\varepsilon^e_{yy} = (1-\nu)d\sigma / E$. The in-plane deformation of the thin film is constrained by the substrate, namely, $d\varepsilon_{xx} = d\varepsilon_{yy} = 0$. In the elastic stage, the increment of the plastic strain vanishes, so that

$$\frac{d\sigma}{dc} = -\frac{\beta E}{3(1-\nu)}. \tag{3.6}$$

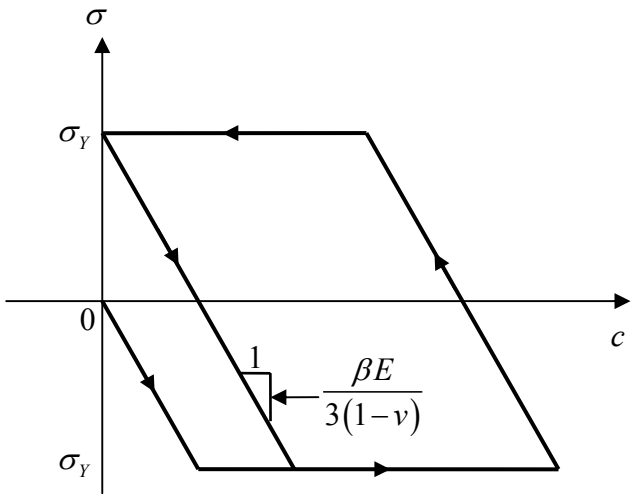

Figure 3. 2. Evolution of stress in a thin film of an inelastic host during cyclic lithiation and delithiation.

Figure 3. 2 plots the stress evolution as a function of Li concentration c. The

lithiation starts from pure silicon. Initially the film deforms elastically, and develops a compressive stress, with the slope given by Eq. (3. 6). When the magnitude of compressive stress reaches the yield strength σ_Y, the film deforms plastically. For simplicity, the yield strength is taken to be a constant, independent of the concentration of Li. Upon delithiation, the film unloads elastically, develops a tensile stress, and then deforms plastically in tension. The fully lithiated state causes a volume expansion about 300%,[6] so that $\beta = 3$. Take the representative values for silicon, $E = 80$ GPa and $\nu = 0.22$.[53] Equation (3. 6) gives the slope $d\sigma / dc = -103$GPa, which may be compared to the measured value -75 GPa in Ref. [52].

3.3 Stresses in a spherical particle of silicon

In the thin film, the stress can be induced by the constraint imposed by the substrate. By contrast, a particle, a nanowire, or a porous structure is almost unconstrained by other materials, and the stress is mainly induced by the inhomogeneous distribution of Li.[16] Consequently, the stress is small when the feature size and charge rate are small.

To explore the effect of inelastic deformation, we study the evolution of the stress field in a spherical particle of silicon. We use the "Thermal-Structural Interaction" module in COMSOL to solve the combined diffusion and elastic-plastic problem. The lithiation-induced strain is simulated by imposing a thermal strain. The particle is initiated as pure silicon, and is charged and discharged at a constant

current. The dimensionless charge and discharge rate is set to be $i_n a / DC_{\max} = 0.206$, where a is the radius of the particle, i_n is the current density for charge and discharge, and $C_{\max}$ is the theoretical capacity of fully lithiated silicon. This dimensionless rate corresponds to $i_n = 0.176 \text{A/m}^2$ for representative values $a = 1\ \mu\text{m}$, $D = 1\times10^{-16}\ \text{m}^2/\text{s}$ [59] and $C_{\max} = 8.52\times10^{9}\ \text{Coulomb/m}^3$.[60] At this rate, silicon could be charged to its full theoretical capacity in about 4.5 hours.

Fig 3. 3 (a) shows the distribution of Li at several times during lithiation, while Figs. 3. 3 (b), (c) and (d) show the distributions of the equivalent, radial and hoop stresses. The equivalent stress is bounded in the interval $0 \le \sigma_e \le \sigma_Y$. The traction-free boundary-condition requires the radial stress at the surface of the particle to vanish at all times. As more Li is inserted, the particle expands more near the surface than near the center, resulting in tensile radial stresses. The hoop stress is compressive near the surface, and tensile near the center. For the spherical particle, the yield condition takes the form $\left|\sigma_{\theta\theta} - \sigma_{rr}\right| = \sigma_Y$. Due to the triaxial constraint at the center, the radial stress and hoop stress can exceed the yield strength. Additional calculations (not shown here) indicate that faster charging rates result in even larger values of the radial and hoop stresses. These large tensile stresses may cause fracture. Also, large values of hydrostatic stress may cause an inelastic material to grow cavities,[58] although we are unaware of any experimental observation of lithiation-induced cavitation at this writing.

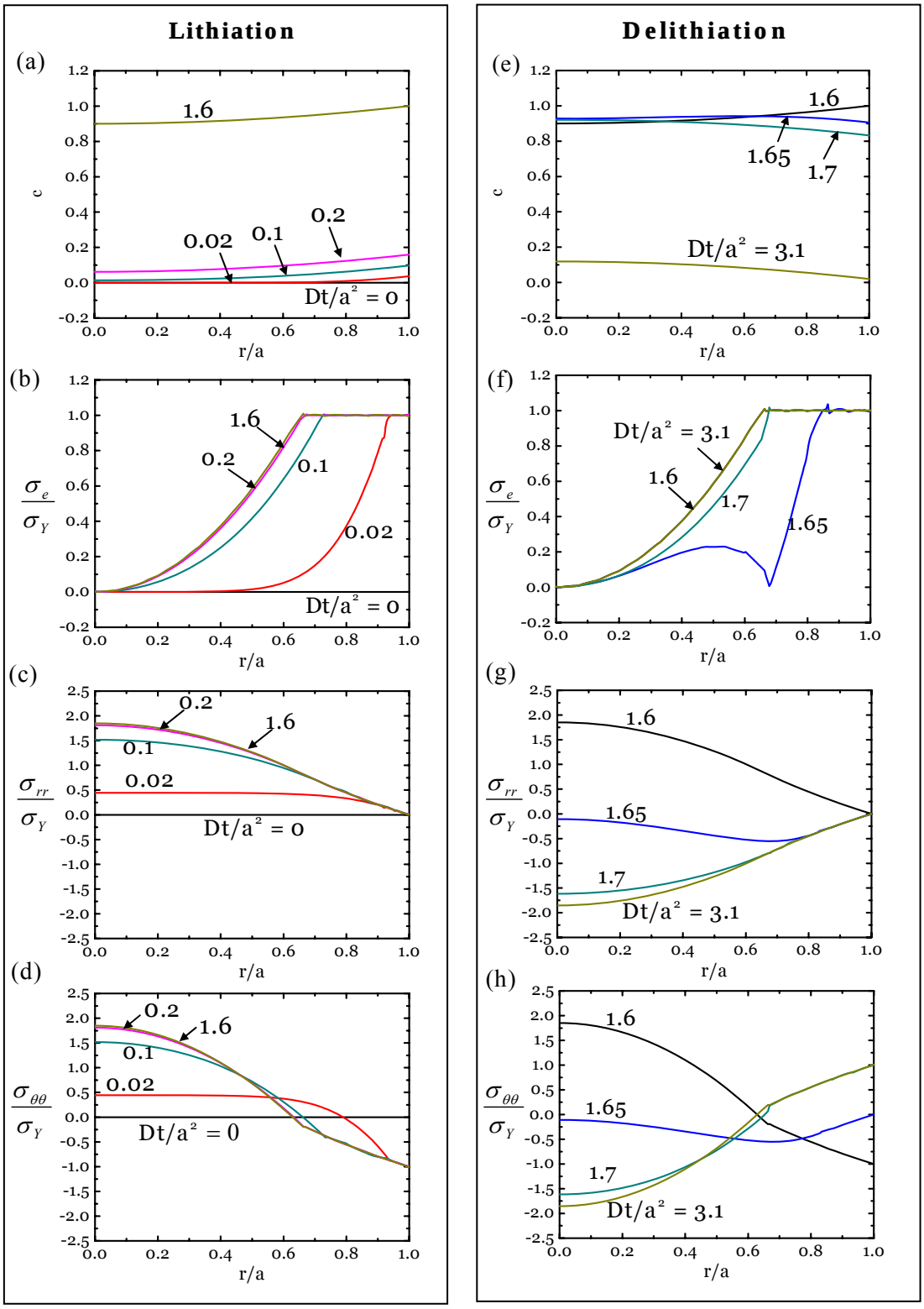

Figure 3. 3. The evolution of (a) concentration of Li, (b) equivalent stress, (c) radial stress and (d) hoop stress in a spherical particle of silicon during lithiation. The evolution of (e) concentration of Li, (f) equivalent stress, (g) radial stress and (h) hoop stress during delithiation.

The stress field builds up by the dimensionless time $Dt/a^2 = 0.2$, and remains nearly unchanged upon further lithiation. This phenomenon occurs because the stress field is induced by an inhomogeneous distribution of Li in the spherical particle. The inhomogeneity of the distribution of Li depends on the competition between charge rate and diffusion rate, but is insensitive to the total number of Li atoms inserted.[16]

The Li concentration at the surface reaches a value of unity at time $Dt/a^2 = 1.6$. At this point, we reverse the electric current and start delithiation. Figure 3. 3 (e) shows the distribution of Li at several times during delithiation, while Figs. 3. 3 (f), (g) and (h) show the equivalent, radial and hoop stresses. As Li desorbs, the radial stress evolves from tension to compression. Also, the hoop stress at the surface becomes tensile with magnitude σ_Y. This tensile stress may result in the propagation of surface flaws. Similar to a thin film, the sphere can avert fracture if the radius is small and the yield strength is low.

3.4 Summary

We develop a model of an inelastic host of Li by considering diffusion, elastic-plastic deformation, and fracture. The model allows us to simulate the distribution of concentration and stress in the host during charge and discharge. For an electrode of a small feature size and low yield strength, inelastic deformation can prevent fracture.

Chapter 4

Large plastic deformation caused by charge and discharge

4.1 Introduction

Li-ion batteries are being intensely developed to achieve safe operation, high capacity, fast charging, and long life. Each electrode in a Li-ion battery is a host of lithium. If a particle of the electrode material is charged or discharged slowly, unconstrained by other materials, the distribution of Li in the particle is nearly homogeneous, and the particle expands or contracts freely, developing no stress. In practice, however, charge and discharge cause a field of stress in the particle when the distribution of Li is inhomogeneous,[16] or the host contains different phases,[15] or the host is constrained by other materials.[10] The stress may cause the electrode to fracture, which may lead the capacity of the battery to fade.

Lithiation-induced fracture not only occurs in commercial Li-ion batteries, but is also a bottleneck in developing future Li-ion batteries. For example, of all known materials for anodes, silicon offers the highest theoretical specific capacity. Silicon is not used in anodes in commercial batteries, mainly because the capacity fades after a small number of cycles—a mode of failure often attributed to lithiation-induced fracture.

Recent experiments, however, have shown that the capacity can be maintained over many cycles for silicon anodes of small feature sizes. When silicon is

fully lithiated, the volume of the material swells by ~300%. For anodes of small feature sizes, evidence has accumulated recently that this lithiation-induced strain can be accommodated by plastic deformation. For instance, cyclic lithiation causes silicon thin films and silicon nanowires to develop undulations.[20], [21] Furthermore, when cyclically charged and discharged, a thin film of silicon bonded on a wafer deforms plastically upon reaching a yield strength.[52] Cyclic lithiation and delithiation can also cause silicon to grow cavities.[61]

This chapter develops a theory of finite plastic deformation of electrodes caused by charge and discharge. Plastic deformation has not been considered in most existing theories of lithiation-induced deformation.[11]-[16], [34]-[41] The works that do include plasticity have been limited to small deformation.[61], [62] Here we analyze the homogeneous lithiation and deformation in a small element of an electrode within nonequilibrium thermodynamics, stipulating equilibrium with respect to some processes, but not others. The element is assumed to undergo plastic deformation when the state of stress reaches a yield condition. We then combine large plastic deformation and diffusion to analyze the lithiation of a spherical particle of an electrode. When a small particle is charged and discharged slowly, the stress is small. When the particle is charged and discharged quickly, the stress is high, potentially leading to fracture or cavitation.

4.2 Nonequilibrium thermodynamics of coupled lithiation and deformation

Figure 4. 1 illustrates an element of an electrode subject to a cycle of charge and discharge. The element is small in size, so that fields in the element are homogeneous. In the reference state (Figure 4. 1 (a)), the element is a unit cube of a host material, free of Li and under no stress. When the element is connected to a reservoir of Li at chemical potential μ and is subject to stresses s_1, s_2 and s_3, as illustrated in Figure 4. 1 (b), the element absorbs a number C of Li atoms, becomes a block of sides λ_1, λ_2 and λ_2, and gains in free energy W.

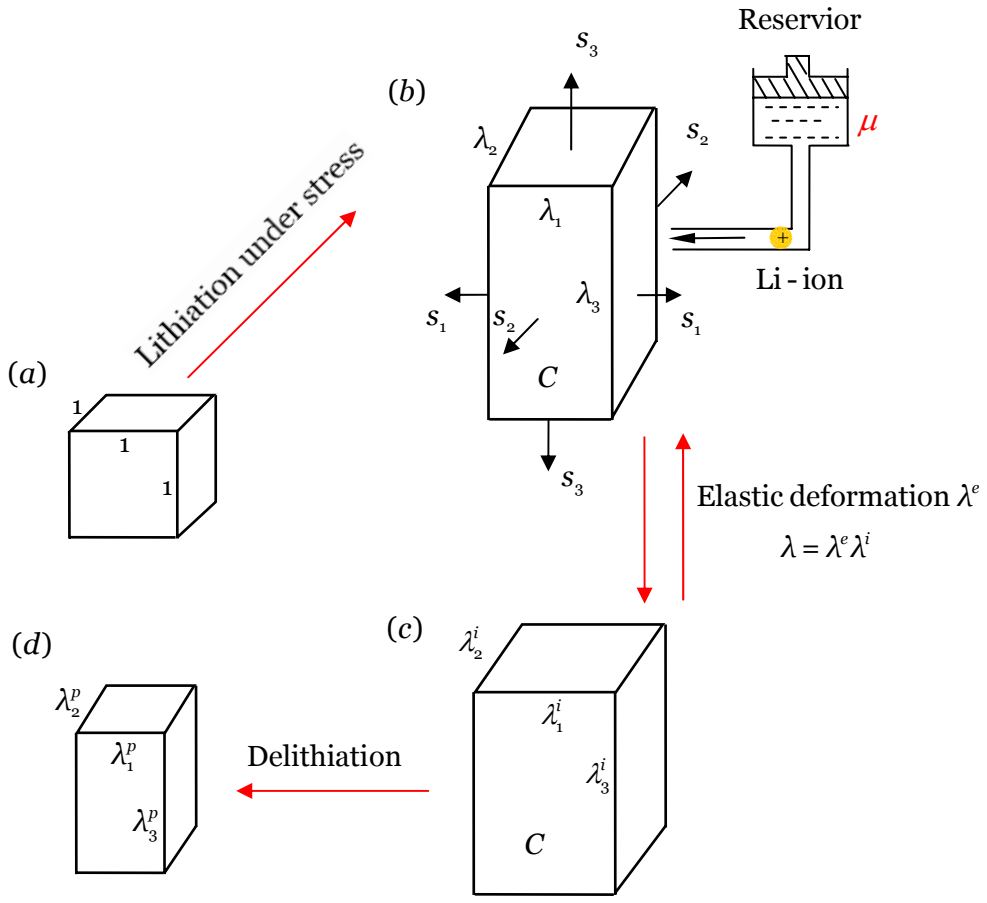

Figure 4. 1. After a cycle of lithiation and delithiation, an electrode material may not recover its initial shape. (a) In the reference state, an element of an electrode material is a Li-free and stress-free unit cube. (b) Subject to forces and connected to a reservoir of Li, the material element absorbs Li, and undergoes anisotropic deformation. (c) When the stresses are removed and the reservoir of Li is disconnected, the material element unloads elastically, and the remaining inelastic deformation is anisotropic. (d) After the material element desorbs Li under no stress, the Li-free host becomes a rectangular block.

By definition, s_1, s_2 and s_3 are nominal stresses—forces acting on the element in the current state divided by the areas of the element in the reference state. The true stresses, σ_1, σ_2 and σ_3, are forces per unit areas of the element in the current state. The true stresses relate to the nominal stresses by $\sigma_1 = s_1/(\lambda_2\lambda_3)$, $\sigma_2 = s_2/(\lambda_3\lambda_1)$ and $\sigma_3 = s_3/(\lambda_1\lambda_2)$.

Associated with small changes in the stretches, $\delta\lambda_1$, $\delta\lambda_2$ and $\delta\lambda_3$, the forces do work $s_1\delta\lambda_1 + s_2\delta\lambda_2 + s_3\delta\lambda_3$. Associated with small change in the number of Li atoms, δC, the chemical potential does work $\mu\delta C$. Thermodynamics dictates that the combined work should be no less than the change in the free energy:

$$s_1\delta\lambda_1 + s_2\delta\lambda_2 + s_3\delta\lambda_3 + \mu\delta C \geq \delta W \tag{4.1}$$

The work done minus the change in the free energy is dissipation. The inequality (4. 1) means that the dissipation is nonnegative with respect to all processes. The object of this section is to examine the large amounts of lithiation and deformation by constructing a theory consistent with the thermodynamic inequality (4. 1).

As illustrated in Figure 4. 1 (b), when the unit cube of the host is lithiated under stresses, the deformation is anisotropic: the unit cube will change both its shape and volume. For example, a thin film of an electrode constrained on a stiff substrate, upon absorbing Li, deforms in the direction normal to the film, but does not deform in the directions in the plane of the film.

The material deforms by mechanisms of two types: inelastic and elastic. Inelastic deformation involves mixing and rearranging atoms. Elastic deformation involves small changes of the relative positions of atoms, retaining the identity of

neighboring atoms as well as the concentration of Li. When the stresses are removed and the reservoir of Li is disconnected, the material element will retain part of the anisotropic deformation (Figure 4. 1 (c)). The phenomenon is reminiscent of plasticity of a metal. The remaining deformation is characterized by three stretches λ_1^i, λ_2^i and λ_3^i, which we call inelastic stretches. The part of deformation that disappears upon the removal of the stresses is characterized by three stretches λ_1^e, λ_2^e and λ_3^e, which we call elastic stretches. The total stretches are taken to be the products of the two types of the stretches

$$\lambda_1 = \lambda_1^e \lambda_1^i, \quad \lambda_2 = \lambda_2^e \lambda_2^i, \quad \lambda_3 = \lambda_3^e \lambda_3^i. \tag{4.2}$$

Similar multiplicative decomposition is commonly used to describe elastic-plastic deformation of metals[63] and polymers,[64] as well as growth of tissues.[65]

We characterize the state of the material element by a total of seven independent variables: λ_1^e, λ_2^e, λ_3^e, λ_1^i, λ_2^i, λ_3^i and C. Plasticity of a metal and inelasticity of an electrode differ in a significant aspect. While plastic deformation of a metal changes shape but conserves volume, inelastic deformation of an electrode changes both volume and shape. We decompose the inelastic stretches by writing

$$\lambda_1^i = \Lambda^{1/3} \lambda_1^p, \quad \lambda_2^i = \Lambda^{1/3} \lambda_2^p, \quad \lambda_3^i = \Lambda^{1/3} \lambda_3^p. \tag{4.3}$$

Here Λ is the volume of the material element after the removal of the stresses, namely,

$$\lambda_1^i \lambda_2^i \lambda_3^i = \Lambda. \tag{4.4}$$

Inelastic shape change of the material element is described by λ_1^p, λ_2^p, and λ_3^p (Figure 4. 1 (d)). By the definition of (4.3) and (4.4), the plastic stretches do not

change volume, namely,

$$\lambda_1^p \lambda_2^p \lambda_3^p = 1. \tag{4.5}$$

We will call λ_1^p, ,λ_2^p and λ_3^p the plastic stretches. In our terminology, inelastic deformation includes the changes in both volume and shape, while plastic deformation involves only the change in shape.

A combination of (4.2) and (4.3) gives $\lambda_1 = \lambda_1^e \lambda_1^p \Lambda^{1/3}$. Taking logarithm on both sides of this equation, we write $\log \lambda_1 = \log \lambda_1^e + \log \lambda_1^p + \log \Lambda^{1/3}$. The quantity $\log \lambda_1$ is the natural strain, $\log \lambda_1^e$ the elastic part of the natural strain, and $\log \lambda_1^p$ the plastic part of the natural strain.

Most existing theories of lithiation-induced deformation do not consider plasticity. In effect, these theories assume that, after a cycle of lithiation and delithiation, the material element recovers its initial shape. Such an assumption disagrees with experimental observations of lithiation of large-capacity hosts, such as silicon, as discussed in the Introduction. This chapter will allow plasticity, and will describe rules to calculate large plastic deformation.

The state of the element can be characterized by an alternative list of seven independent variables: λ_1^e, λ_2^e, λ_3^e, λ_1^p, λ_2^p, Λ and C. To progress further, we make the following simplifying assumptions. The inelastic expansion of the volume is taken to be entirely due to the absorption of Li, and is a function of the concentration of Li:

$$\Lambda = \Lambda(C). \tag{4.6}$$

This function is taken to be characteristic of the material, and is independent of the

elastic and plastic stretches. Equation (4.6) eliminates Λ from the list of independent variables, so that the state of the material element is characterized by six independent variables: λ_1^e, λ_2^e, λ_3^e, λ_1^p, λ_2^p and C.

Following the theory of plasticity, we assume that the free energy of the material element is unaffected by the plastic stretches. Thus, the free energy is a function of four variables:

$$W = W\left(\lambda_1^e, \lambda_2^e, \lambda_3^e, C\right). \tag{4.7}$$

This assumption is understood as follows. The plastic stretches characterize inelastic shape change, involving rearranging atoms without changing the concentration of Li. This rearrangement of atoms may dissipate energy, but does not alter energy-storing microstructure. The situation is reminiscent of shear flow of a liquid of small molecules—no matter how much the liquid has flowed, the free energy is stilled stored in the same molecular bonds, independent of amount of flow. For a work-hardening metal, however, plastic strain creates energy-storing changes in the microstructure, such as creating more dislocations. Thus, assuming (4.7) amounts to a stipulation that plastic strains do not create any energy-storing changes in the microstructure.

Rewriting the inequality (4.1) in terms of the changes in the six independent variables, λ_1^e, λ_2^e, λ_3^e, λ_1^p, λ_2^p and C, we obtain that

$$\begin{aligned}
&\left(\sigma_1\lambda_1\lambda_2\lambda_3 - \frac{\partial W}{\partial \log \lambda_1^e}\right)\delta \log \lambda_1^e + \left(\sigma_2\lambda_1\lambda_2\lambda_3 - \frac{\partial W}{\partial \log \lambda_2^e}\right)\delta \log \lambda_2^e \\
&+\left(\sigma_3\lambda_1\lambda_2\lambda_3 - \frac{\partial W}{\partial \log \lambda_3^e}\right)\delta \log \lambda_3^e + \left(\mu - \frac{\partial W}{\partial C} + \Omega\sigma_m\right)\delta C \qquad , \\
&+\lambda_1\lambda_2\lambda_3\left[\left(\sigma_1 - \sigma_3\right)\delta \log \lambda_1^p + \left(\sigma_2 - \sigma_3\right)\delta \log \lambda_2^p\right] \geq 0
\end{aligned} \tag{4.8}$$

where $\sigma_m = (\sigma_1 + \sigma_2 + \sigma_3)/3$ is the mean stress, and $\Omega = \lambda_1^e \lambda_2^e \lambda_3^e d\Lambda(C)/dC$ is the volume per Li atom in the host.

Each of the six independent variables represents a process to evolve the material. The processes take place at different rates. We will adopt a commonly used simplifying approach. Say that we are interested in a particular time scale. Processes taking place faster than this time scale are assumed to be instantaneous. Processes taking place slower than this time scale are assumed to never occur. In the present problem, the particular time scale of interest is the time needed for a particle of an electrode material of a finite size to absorb a large amount of Li. This time is taken to be set by the diffusion time scale.

Elastic relaxation is typically much faster than diffusion. We assume that the material element is in equilibrium with respect to the elastic stretches, so that in (4.8) the coefficients associated with $\delta\lambda_1^e$, $\delta\lambda_2^e$ and $\delta\lambda_3^e$ vanish:

$$\sigma_1 = \frac{\partial W}{\lambda_1\lambda_2\lambda_3 \partial \log \lambda_1^e}, \quad \sigma_2 = \frac{\partial W}{\lambda_1\lambda_2\lambda_3 \partial \log \lambda_2^e}, \quad \sigma_3 = \frac{\partial W}{\lambda_1\lambda_2\lambda_3 \partial \log \lambda_2^e}. \tag{4.9}$$

We further assume that the material element is in equilibrium with respect to the concentration of Li, so that in (4.8) the coefficient of δC vanishes:

$$\mu = \frac{\partial W(\lambda_1^e, \lambda_2^e, \lambda_3^e, C)}{\partial C} - \Omega\sigma_m. \tag{4.10}$$

Since elastic deformation is small, we adopt the free energy of the form:

$$W = W_0(C) + \Lambda G\left[(\log\lambda_1^e)^2 + (\log\lambda_2^e)^2 + (\log\lambda_3^e)^2 + \frac{\nu}{1-2\nu}(\log\lambda_1^e\lambda_2^e\lambda_3^e)^2\right], \tag{4.11}$$

where G is the shear modulus, and ν Poisson's ratio. A combination of (4.11) into (4.9) shows that the stresses relate to the elastic strains as

$$\begin{aligned}\sigma_1 &= 2G\left(\log\lambda_1^e + \frac{\nu}{1-2\nu}\log\lambda_1^e\lambda_2^e\lambda_3^e\right)\\ \sigma_2 &= 2G\left(\log\lambda_2^e + \frac{\nu}{1-2\nu}\log\lambda_1^e\lambda_2^e\lambda_3^e\right).\\ \sigma_3 &= 2G\left(\log\lambda_3^e + \frac{\nu}{1-2\nu}\log\lambda_1^e\lambda_2^e\lambda_3^e\right)\end{aligned} \tag{4.12}$$

A combination (4.11) and (4.9) expresses the chemical potential of Li as

$$\mu = \frac{dW_0(C)}{dC} - \Omega\sigma_m . \tag{4.13}$$

In writing (4.12) and (4.13), we have neglected the terms quadratic in the elastic strains.

The material element, however, may not be in equilibrium with respect to plastic stretches. Consequently, the inequality (4.8) is reduced to

$$(\sigma_1 - \sigma_3)\delta\log\lambda_1^p + (\sigma_2 - \sigma_3)\delta\log\lambda_2^p \geq 0 \tag{4.14}$$

This thermodynamic inequality may be satisfied by many kinetic models—creep models that relate the rate of plastic strains to stresses. For simplicity, here we adopt a particular type of kinetic model: the model of time-independent plasticity. A material is characterized by a yield strength. When the stress is below the yield strength, the rate of the plastic strain is taken to be so low that no additional plastic strain occurs. When the stress reaches the yield strength, the rate of plastic strain is taken to be so high that plastic strain increases instantaneously.

To calculate plastic deformation, we adopt the J_2 flow theory.[58] Recall that the plastic stretches preserve the volume, $\lambda_1^p\lambda_2^p\lambda_3^p = 1$. Consequently, (4.14) may be written in a form symmetric with respect to the three directions:

$$(\sigma_1 - \sigma_m)\delta\log\lambda_1^p + (\sigma_2 - \sigma_m)\delta\log\lambda_2^p + (\sigma_3 - \sigma_m)\delta\log\lambda_3^p \geq 0 . \tag{4.15}$$

The J_2 flow theory is prescribed as

$$\begin{aligned}\delta \log \lambda_1^p &= \alpha\left(\sigma_1 - \sigma_m\right),\\ \delta \log \lambda_2^p &= \alpha\left(\sigma_2 - \sigma_m\right),\\ \delta \log \lambda_3^p &= \alpha\left(\sigma_3 - \sigma_m\right),\end{aligned} \tag{4.16}$$

where α is a nonnegative scalar. This flow theory is symmetric with respect to the three directions, satisfies $\lambda_1^p \lambda_2^p \lambda_3^p = 1$, and is consistent with the thermodynamic inequality (4.15). In numerical calculations later, we will assume that the material is perfectly plastic. Let σ_Y be the yield strength measured when the material element is subject to uniaxial stressing. The yield strength is taken to be a function of concentration alone, $\sigma_Y(C)$. When the material element is under multiaxial stressing, the equivalent stress is defined by

$$\sigma_e = \sqrt{\frac{3}{2}\left[\left(\sigma_1 - \sigma_m\right)^2 + \left(\sigma_2 - \sigma_m\right)^2 + \left(\sigma_3 - \sigma_m\right)^2\right]}. \tag{4.17}$$

The material element yields under the von Mises condition: $\sigma_e = \sigma_Y(C)$. The value of α is specified by the following rules

$$\begin{cases}\alpha = 0, & \sigma_e < \sigma_Y\\ \alpha = 0, & \sigma_e = \sigma_Y,\ \delta\sigma_e < \delta\sigma_Y\\ \alpha > 0, & \sigma_e = \sigma_Y,\ \delta\sigma_e = \delta\sigma_Y\end{cases}. \tag{4.18}$$

4.3 A numerical example of a spherical particle

We now apply the theory to a spherical particle of an electrode material (Figure 4. 2). We have previously solved this problem using a theory of small plastic deformation.[61] Here we will allow large deformation. Before absorbing any Li, the particle is of radius *A*, and is stress-free. This Li-free particle is taken to be the reference configuration. At time *t*, the particle absorbs some Li, the distribution of

which may be inhomogeneous in the radial direction, but retains spherical symmetry. The inhomogeneous distribution of Li induces in the particle a field of stress, and the particle swells to a radius a.

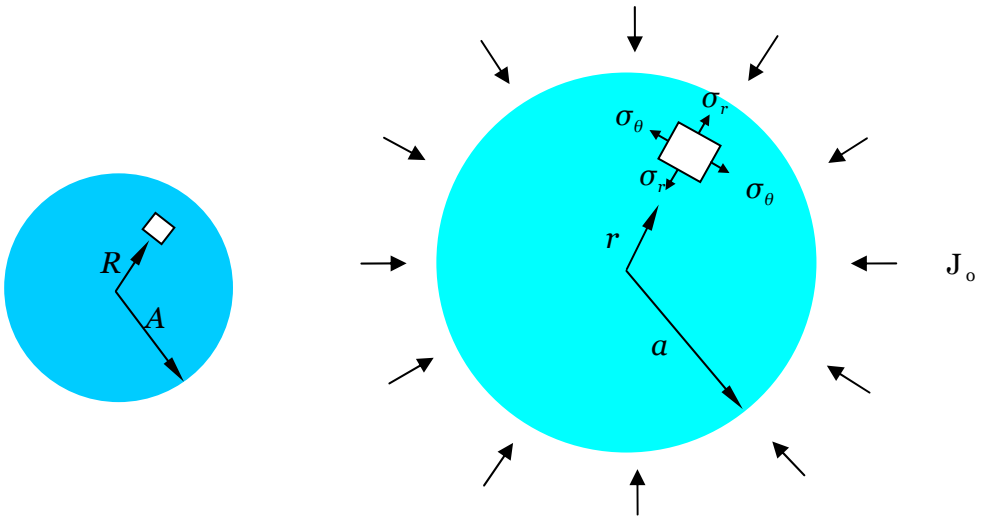

(a). Reference state (b). Current state

Figure 4. 2. (a) In the reference state, a spherical particle of an electrode is Li-free and stress-free. (b) In the current sate, the particle is partially lithiated, and develops a field of stress.

The kinematics of the large deformation is specified as follows. The spherical particle consists of a field of material elements. A material element a distance R from the center in the reference configuration moves, at time t, to a place a distance r from the center. The function $r(R,t)$ specifies the deformation of the particle. In representing a field, we may choose either r or R as an independent variable. One variable can be changed to the other by using the function $r(R,t)$. We will indicate our choice in each field explicitly when the distinction is important. The radial stretch is

$$\lambda_r = \frac{\partial r(R,t)}{\partial R}. \tag{4.19}$$

The hoop stretch is

$$\lambda_\theta = \frac{r}{R}. \tag{4.20}$$

The kinematics of Li is specified as follows. Let C be the nominal concentration of Li (i.e., the number of Li atoms per unit volume of pure silicon in the reference state). The distribution of Li in the particle is specified by the function $C(R,t)$. Due to the spherical symmetry, Li diffuses in the radial direction. Let J be the nominal flux of Li (i.e., the number of Li atoms per unit reference area per unit time). The nominal flux is also a time-dependent field, $J(R,t)$. Conservation of the number of Li atoms requires that

$$\frac{\partial C(R,t)}{\partial t} + \frac{\partial\left(R^2 J(R,t)\right)}{R^2 \partial R} = 0. \tag{4.21}$$

Later we will also invoke the true concentration c (i.e., the number of Li atoms per unit volume in the current configuration), and the true flux j (i.e., the number of Li atoms per current area per time). These true quantities relate to their nominal counterparts by $J = j\lambda_\theta^2$ and $C = c\lambda_r\lambda_\theta^2$.

Write the radial stretch λ_r and the hoop stretch λ_θ in the form

$$\lambda_r = \lambda_r^e \lambda_r^p \Lambda^{1/3}, \qquad \lambda_\theta = \lambda_\theta^e \lambda_\theta^p \Lambda^{1/3}. \tag{4.22}$$

We will mainly consider high-capacity hosts that undergo large deformation by lithiation, and will neglect the volumetric change due to elasticity, setting $\lambda_r^e\left(\lambda_\theta^e\right)^2 = 1$. Consistent with this assumption, we set Poison's ratio $\nu = 1/2$, and set Young's modulus $E = 3G$. Recall that by definition the plastic stretches preserve volume, $\lambda_r^p\left(\lambda_\theta^p\right)^2 = 1$.

In the spherical particle, each material element is subject to a state of triaxial stresses, $(\sigma_r, \sigma_\theta, \sigma_\theta)$, where σ_r is the radial stress, and σ_θ the hoop stress. The

state of elastic-plastic deformation is taken to be unaffected when a hydrostatic stress is superimposed on the element. In particular, as illustrated in Figure 4. 3 (a), superimposing a hydrostatic stress $(-\sigma_\theta,-\sigma_\theta,-\sigma_\theta)$ to the state of triaxial stresses $(\sigma_r,\sigma_\theta,\sigma_\theta)$ results in a state of uniaxial stress $(\sigma_r-\sigma_\theta,\ 0,\ 0)$. The state of elastic-plastic deformation of the element subject to the triaxial stresses is the same as the state of plastic deformation of the element subject to a uniaxial stress $\sigma_r-\sigma_\theta$.

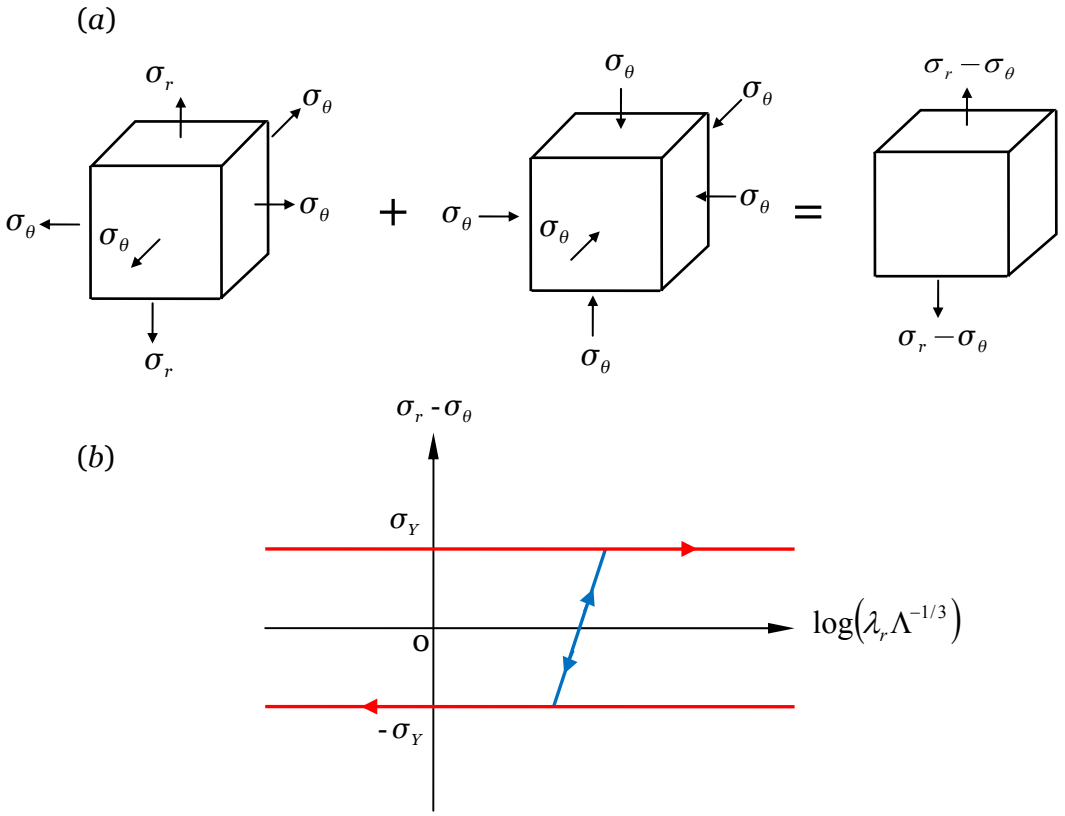

Figure 4. 3. (a) The state of elastic-plastic deformation of the element subject to the triaxial stresses $(\sigma_r,\sigma_\theta,\sigma_\theta)$ is the same as that of the element subject to a uniaxial stress $(\sigma_r-\sigma_\theta)$. (b) The uniaxial stress-strain relation in terms of the stress $(\sigma_r-\sigma_\theta)$ and the true elastic-plastic strain $\log(\lambda_r\Lambda^{-1/3})$.

We represent the uniaxial stress-stretch relation by the elastic and perfectly plastic model. Figure 4. 3 (b) sketches this stress-strain relation in terms of the stress $\sigma_r-\sigma_\theta$ and the elastic-plastic part of the true strain, $\log(\lambda_r^e\lambda_r^p)=\log(\lambda_r\Lambda^{-1/3})$.

The yield strength in the state of uniaxial stress, σ_Y, is taken to be a constant independent of the plastic strain and concentration of Li.

In the spherical particle the stresses are inhomogeneous, represented by functions $\sigma_r(R,t)$ and $\sigma_\theta(R,t)$. The balance of forces acting on a material element requires that

$$\frac{\partial \sigma_r(R,t)}{\lambda_r \partial R} + 2\frac{\sigma_r - \sigma_\theta}{\lambda_\theta R} = 0 \tag{4.23}$$

We specify a material model of transport as follows. We assume that each material element is in a state of local equilibrium with respect to the reaction between Li atoms and host atoms, so that we can speak of the chemical potential of Li in the material element. We further assume that the chemical potential of Li in the material element takes the form:

$$\mu = \mu^0 + kT\log(\gamma c) - \Omega\sigma_m, \tag{4.24}$$

where μ^o is a reference value, γ the activity coefficient, and c the true concentration of Li.

If the distribution of Li in the particle is inhomogeneous, the chemical potential of Li is a time-dependent field, $\mu(r,t)$, and the particle is not in diffusive equilibrium. The gradient of the chemical potential drives the flux of Li. We adopt a linear kinetic model:

$$j = -\frac{cD}{kT}\frac{\partial \mu(r,t)}{\partial r}. \tag{4.25}$$

This relation has been written in a conventional form, in terms of the true flux j and the true concentration c. Note that kT is the temperature in the unit of energy, and that (4. 25) may be regarded as a phenomenological definition of the diffusivity D.

Recall that the flux relates to the drift velocity of Li in the host by $j = cv_{drift}$. Thus, D/kT is the mobility of Li in the host. The diffusivity may depend on concentration and stress.

The particle is subject to the following boundary conditions. Due to symmetry, $r(0,t) = 0$ and $J(0,t) = 0$. On the surface of the particle, the radial stress vanishes at all time, $\sigma_r(A,t) = 0$. The particle is charged and discharged by prescribing on the surface of the particle a constant flux J_0, namely, $J(A,t) = \pm J_0$. The signs differ for charge and discharge.

4.4 Numerical results and discussions

We solve the initial-boundary value problem numerically, as described in Appendix A. This section describes the numerical results, and discusses their implications. For simplicity, we set $\gamma = 1$ and assume that Ω, E, σ_Y and D are constant. The initial-boundary value problem has three dimensionless parameters: $\Omega E/kT$, σ_Y/E, and $J_0 A\Omega/D$. For Li in amorphous silicon, representative values are $\Omega = 1.36\times10^{-29}\,\mathrm{m}^3$,[66] $E = 80\,\mathrm{GPa}$, $\sigma_Y = 1.75\,\mathrm{GPa}$,[52] and $D = 10^{-16}\,\mathrm{m}^2/\mathrm{s}$,[59] giving $\Omega E/kT = 263$ and $\sigma_Y/E = 0.022$. The parameter $J_0 A\Omega/D$ is a dimensionless measure of the charging rate, and may be interpreted as follows. Let $C_{\max}$ be the maximum theoretical concentration of Li. When the spherical particle of radius A is charged by a constant flux J_0, the nominal time τ needed to charge the particle to the theoretical maximum concentration is given by $4\pi A^2 J_0 \tau = (4\pi A^3/3) C_{\max}$. For silicon, the volume of fully lithiated state swells by

about 300%, so that $\Omega C_{\max} \approx 3$. For a particle of radius $A = 1\mu\text{m}$, $\tau = 1\text{hour}$ corresponds to $J_o A\Omega / D = 2.8$. Following convention, we speak of τ in terms of the C-rate; for example, 2C means 2 charges per hour, or $\tau = 0.5\text{hours}$. We normalize time as Dt / A^2. For a particle of radius $A = 1\mu\text{m}$, the diffusion time scale is $A^2 / D = 10^4 \text{s}$.

Figure 4. 4 shows the evolution of the fields in the spherical particle lithiated at the rate of 1C. The simulation is initiated when the particle is Li-free, and is terminated when the concentration at the surface of the particle reaches the full capacity, $\Omega C_{\max} = 3$, and the interior of the particle is still much below the full capacity (Figure 4. 4 (a)). At all time, $r(R,t) > R$, indicating all material elements in the particle move away from the center of the particle (Figure 4. 4 (b)). The ratio $\lambda_r / \lambda_\theta$ measures the anisotropy of the deformation (Figure 4. 4 (c)). The deformation is highly anisotropic near the surface of the particle, but is isotropic at the center of the particle. Plastic deformation occurs near the surface of the particle, but is absent at the center of the particle (Figure 4. 4 (d)). The chemical potential of Li in the particle is inhomogeneous, driving Li to diffuse from the surface of the particle toward the center (Figure 4. 4 (e)).

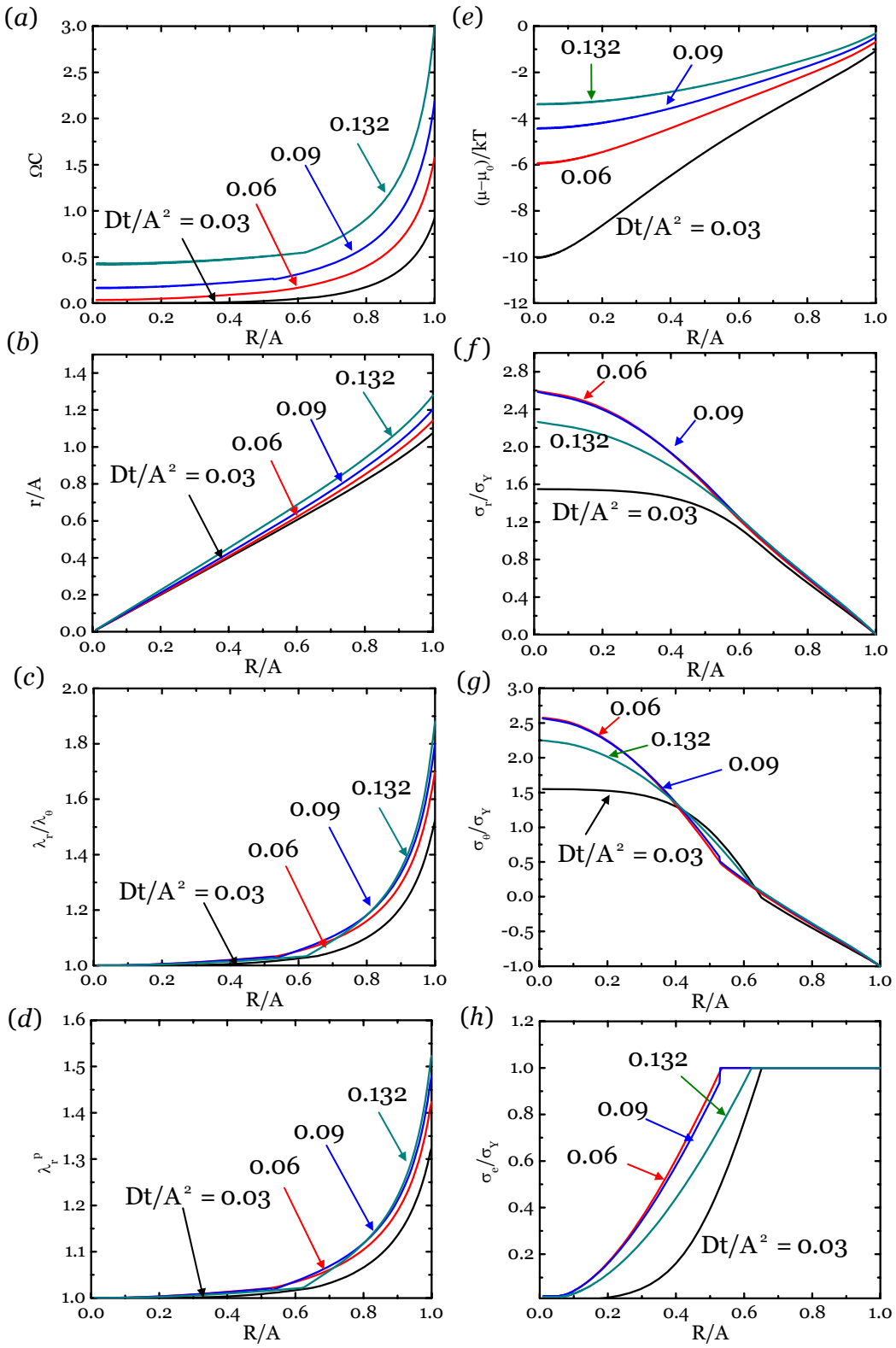

Figure 4. 4. As a spherical particle is being lithiated at the rate of 1C, various fields evolve: (a) concentration of Li, (b) deformation field, (c) ratio of the radial stretch to the hoop stretch, (d) plastic stretch in the radial direction, (e) chemical potential of Li, (f) radial stress, (g) hoop stress, and (h) equivalent stress.

Figs 4. 4 (f), (g) and (h) show the distributions of the radial, hoop and

equivalent stresses. The traction-free boundary-condition requires that the radial stress at the surface of the particle should vanish at all times. Because the distribution of Li in the particle is inhomogeneous, the particle expands more near the surface than at the center, resulting in tensile radial stresses inside the particle. The hoop stress is compressive near the surface, and tensile near the center. For the spherical particle, the equivalent stress is $\sigma_e = |\sigma_\theta - \sigma_r|$, which is bounded in the interval $0 \le \sigma_e \le \sigma_Y$. By symmetry, the center of the sphere is under equal-triaxial tensile stresses. Due to the triaxial constraint at the center, the radial stress and hoop stress can exceed the yield strength.

The high level of tensile stresses at the center of the sphere may generate cavities. An experimentally measured value of the yield strength is $\sigma_Y = 1.75$.[52] Our calculation indicates that the stress at the center of the particle can be several times the yield strength. Let ρ be the radius of a flaw and $\gamma_{surface}$ be the surface energy. For the flaw to expand, the stress needs to overcome the effect of the Laplace pressure, $2\gamma_{surface}/\rho$. Take $\gamma_{surface} = 1\text{J/m}^2$, and we estimate that the critical radius $\rho = 1\text{nm}$ when the stress at the center of the particle is 2GPa. Lithiation-induced cavitation has been observed in a recent experiment.[67]

To illustrate effects of yielding, Figure 4. 5 compares the two cases: $\sigma_Y = 1.75\text{GPa}$ and $\sigma_Y = \infty$ (no yielding). The fields are plotted at time $Dt/A^2 = 0.048$. As expected, yielding allows the particle to accommodate lithiation by greater anisotropic deformation, Figure 4. 5 (b). Yielding also significantly reduces the magnitudes of the stresses, Figure 4. 5 (c) and (d). This

observation implies that fracture and cavitation may be avoided for electrodes with low yield strength.

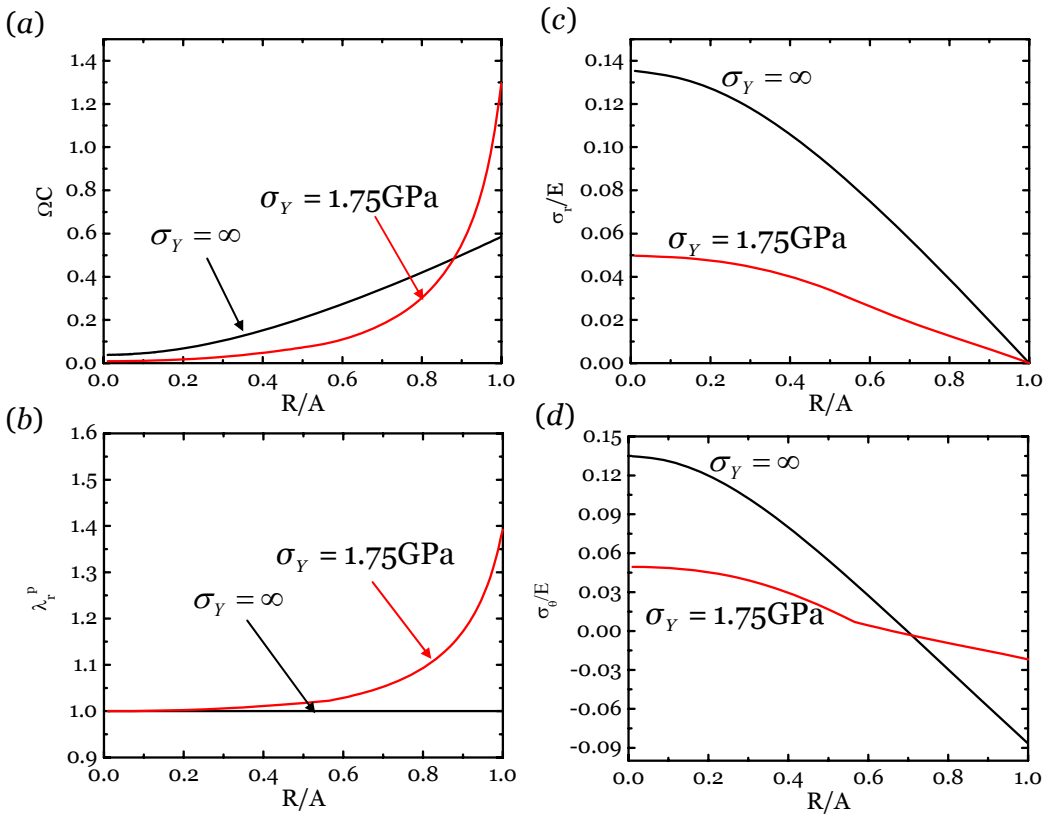

Figure 4. 5. The effect of plastic yield on various fields: (a) concentration of Li, (b) (b) plastic stretch in radial direction, (c) radial stress, and (d) hoop stress. The charging rate is 1C, and the fields are given at time $Dt / A^2 = 0.048$.

As shown by Eq. (4. 24), the chemical potential of Li depends on the mean stress. This effect of stress on chemical potential has been neglected in some of the previous models. The representative values $\Omega = 1.36 \times 10^{-29} \mathrm{m}^3$ and $\sigma_Y = 1.75\mathrm{GPa}$ give an estimate $\Omega\sigma_Y = 0.15\mathrm{eV}$, which is a value significant compared to the value of the term involving concentration in the expression of the chemical potential. Figure 4. 6 compares results calculated by including or neglecting the term $\Omega\sigma_m$ in the expression of the chemical potential (4. 24). The mean stress σ_m is compressive near the surface of the particle and tensile at the center.

Consequently, the gradient of the mean stress also motivates Li to migrate toward the center. Here we show the fields at the time when the surface of the particle attains the full capacity. The case with the mean stress included in the expression of the chemical potential absorbs more Li at the center, Figure 4. 6 (a). The stress gradient also decreases the chemical potential of Li in the particle, Figure4. 6 (b). The inclusion of the stress in the chemical potential helps to homogenize Li distribution, and consequently reduces the stress.

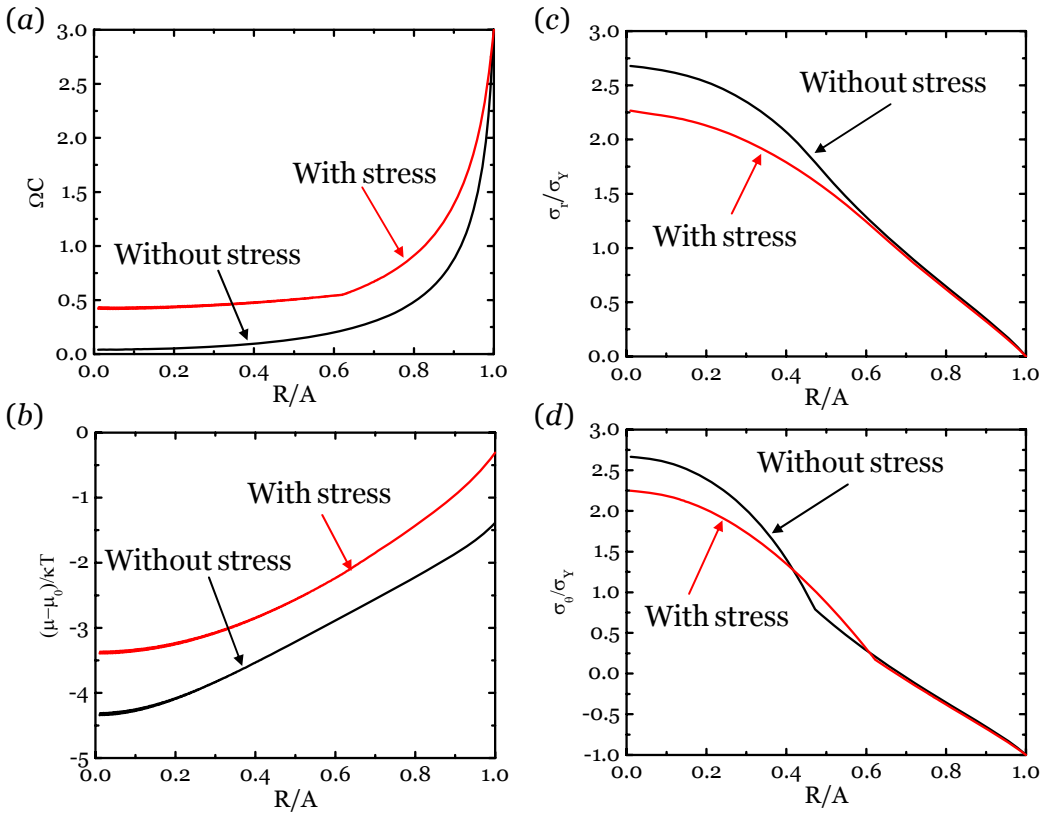

Figure 4. 6. Fields calculated with or without including the mean stress in the expression of the chemical potential of Li are compared: (a) concentration of Li, (b) chemical potential of Li, (c) radial stress, and (d) hoop stress. The charging rate is 1C, and both fields are given at the end of charge time, i.e., $Dt/A^2 = 0.132$ with stress calculation, $Dt/A^2 = 0.09$ without stress calculation.

Figure 4. 7 compares the fields for three charging rates, 0.5C, 1C, and 2C. Each simulation is terminated when the surface of the particle attains the full

capacity. The stress level is determined by the total amount of Li inserted into the particle and the degree of inhomogeneity in the distribution of this amount of Li. At a high charging rate, 2C, the distribution of Li is highly inhomogeneous, as in Figure 4. 7 (a). However, the surface of the particle reaches its full capacity very rapidly. At this time, not much Li has been inserted into the particle, so the stresses are fairly low and the deformation is anisotropic only near the surface of the particle. At such a fast charging rate, the particle will not store much Li. At an intermediate charging rate, 1C, Li has some time to diffuse toward the center of the particle, but not enough time to fully homogenize the distribution of Li. Consequently, relatively large stresses develop and the deformation is quite anisotropic. At a yet slower charging rate, 0.5C, there is enough time for diffusion to nearly homogenize the distribution of Li. At this slow charging rate, the particle is effective as an electrode in that it can store a large amount of Li before the surface of the particle reaches the full capacity. This homogenization leads to relatively low stresses and nearly isotropic deformation.

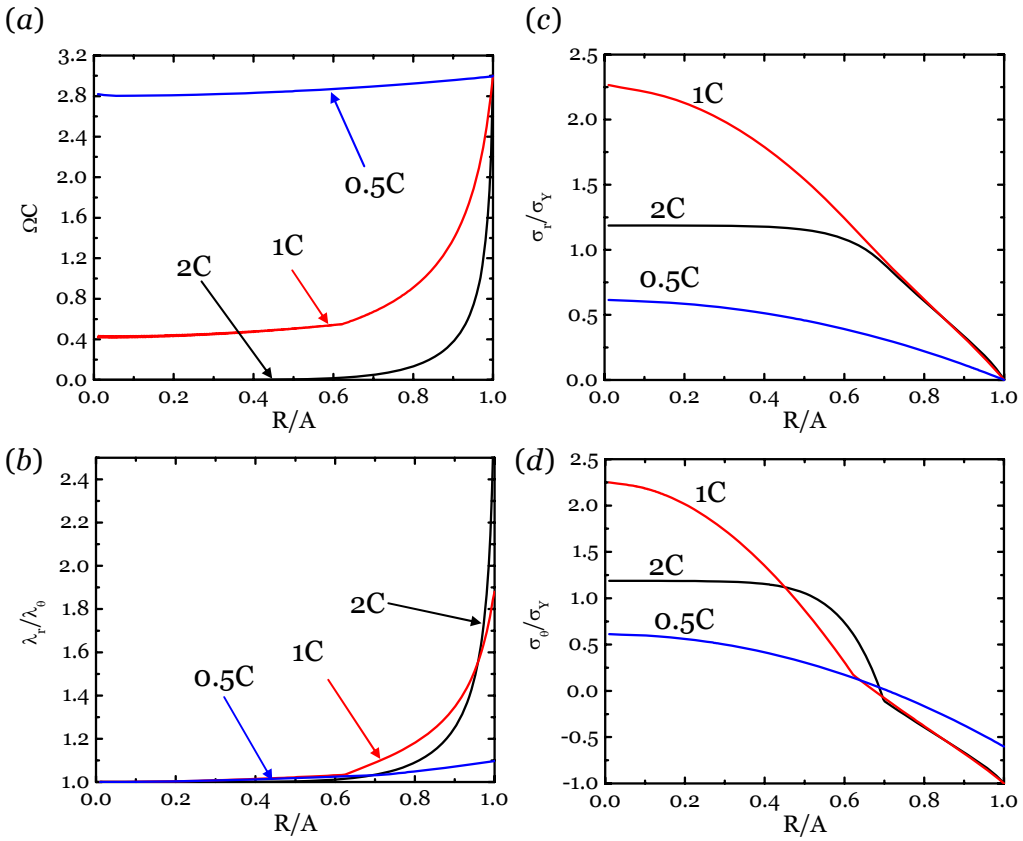

Figure 4. 7. The effect of the charging rate on various fields: (a) concentration of Li, (b) ratio of radial stretch to hoop stretch, (c) radial stress, and (d) hoop stress.

Figure 4. 8 shows the time evolution of the stress at the center of the particle for three charging rates. For a fast charging case (2C), the stress builds up until the outer surface reaches its full capacity. At an intermediate charging rate (1C), the stress builds up until it is large enough to significantly contribute to the chemical potential. At this point, both the stress gradient and concentration gradients tend to homogenize the concentration of Li, and the stress decreases. However, the charging rate is still fairly fast relative to the time for diffusion. Thus, the concentration of Li cannot be fully homogenized and the stress cannot be fully relaxed before the surface of the particle reaches the full capacity. By contrast, for the case of 0.5C, the charging rate is slow enough for diffusion to homogenize the

distribution of Li before the surface of the particle reaches the full capacity, as shown in Figure 4. 7 (a). As the distribution of Li is homogenized, the stress is relaxed, as shown in Figure 4. 8. The effect of the charging rate on the triaxial tension at the center of the particle may be used to guide future experiments to study cavitation.

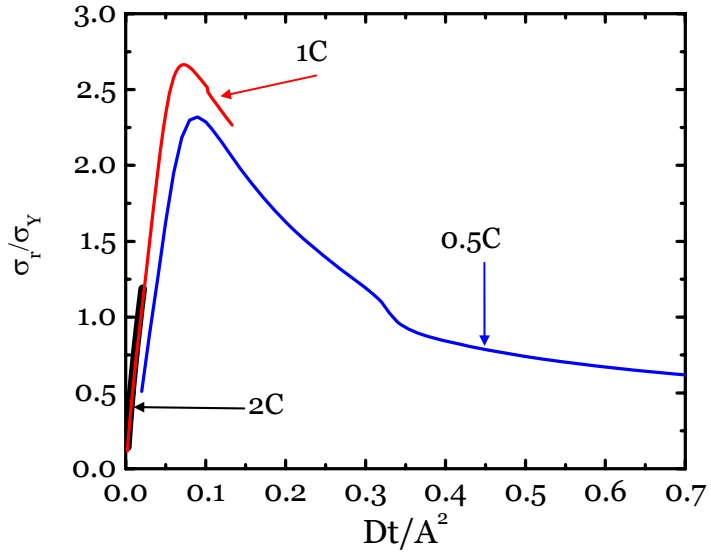

Figure 4. 8. The radial stress at the center of the sphere as a function of time at various charge rates: 0.5C, 1C and 2C.

Figure 4. 9 shows the time evolution of the Li concentration and the stress fields as Li desorbs from the spherical particle. The simulation begins when the particle is at full capacity of Li and is stress-free, and is terminated when the concentration of Li vanishes near the surface of the particle. As Li desorbs, the concentration near the surface becomes lower than it is near the center of the particle, Figure 4. 9 (a). This inhomogeneity causes the particle to contract more near the surface than at the center. Consequently, a compressive radial stress develops, Figure 4. 9 (b). The hoop stress at the surface becomes tensile with magnitude σ_Y, Figure 4. 9 (c). This tensile stress may result in the propagation of surface flaws. Because the tensile

stress is limited by the yield strength, fracture may be averted when the yield strength is low.

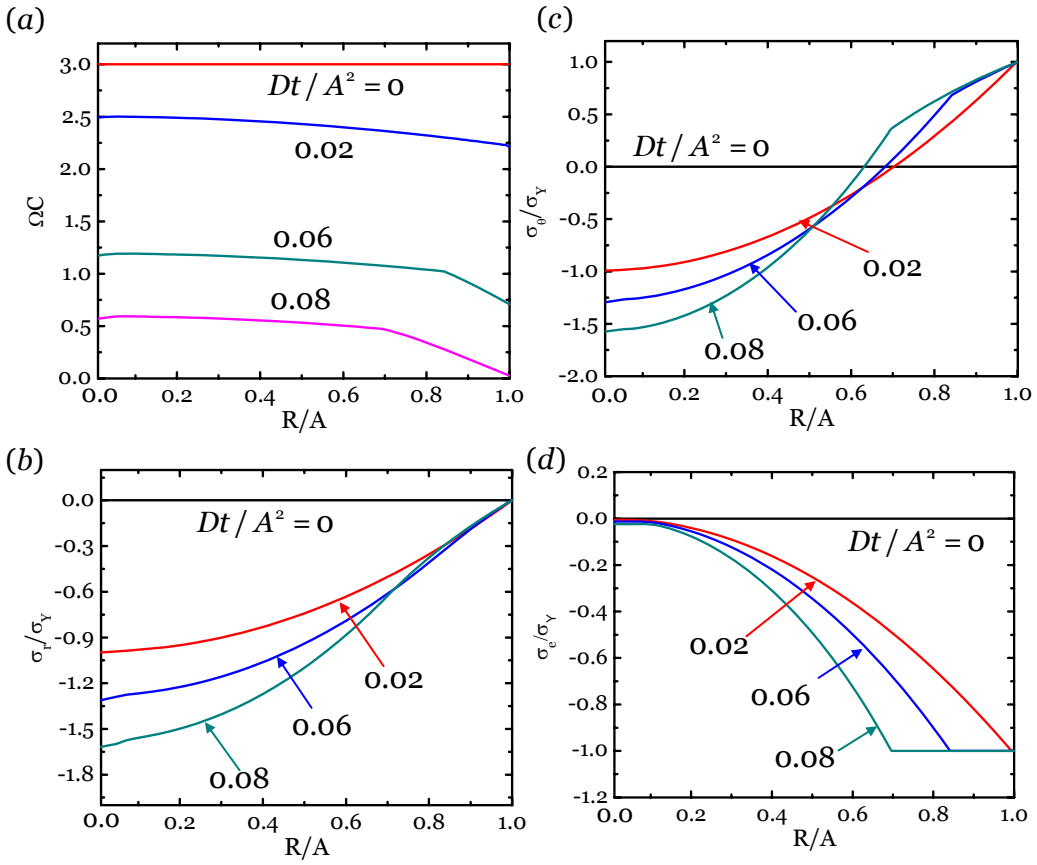

Figure 4. 9. As a spherical particle is being delithiated at the rate of 2C, various fields evolve (a) concentration of Li, (b) radial stress, (c) hoop stress, and (d) equivalent stress.

4.5 Summary

This chapter formulates a theory that couples lithiation and large elastic-plastic deformation. The homogeneous lithiation and deformation in a small material element is analyzed using nonequilibrium thermodynamics. The material is assumed to undergo plastic deformation when the state of stress reaches the yield condition. A spherical particle subject to a constant rate of charge and discharge is analyzed by coupling diffusion and large plastic deformation. The effect of plastic

yielding, stress on the chemical potential of Li, and charging rates are studied. When the charging rate is low, the distribution of Li in the particle is nearly homogeneous, and the stress is low. When the charging rate is high, the stress at the center of the particle can substantially exceed the yield strength. The developed stress gradient also greatly influences the diffusion of Li, tending to homogenize the distribution of Li in the particle. Plastic yielding can markedly reduce the magnitude of stress.

Chapter 5

Fracture and debonding in coated hollow electrodes

5.1 Introduction

High capacity Li-ion batteries are ubiquitous in portable electronics. Development of these batteries is further motivated by their potential use in electric vehicles.[7] Silicon can host a large amount of lithium, making it one of the most promising materials to replace the conventional carbon-based anodes. The commercialization of silicon anodes is mainly limited by mechanical failure and chemical degradation.[68] Mechanical failure results from the dramatic swelling and stress generated during cyclic lithiation and delithiation. The stress may cause fracture of the conductive matrix and active particles, leading to the loss of the conduction path for electrons, Figure 5. 1 (a). As a result, rapid capacity fading of silicon often occurs in the first few cycles.[10] Chemical degradation is attributed mainly to the formation of solid electrolyte interphase (SEI) resulting from the reactions between the electrode and the electrolyte.[68] The formation of the SEI consumes active materials and results in irreversible capacity loss in the first cycle, Figure 5. 1 (b). Furthermore, the repeated swelling and deswelling can cause continual shedding and re-forming of the SEI during cycling, resulting in a persistent decrease in the long-term coulombic efficiency.[24]

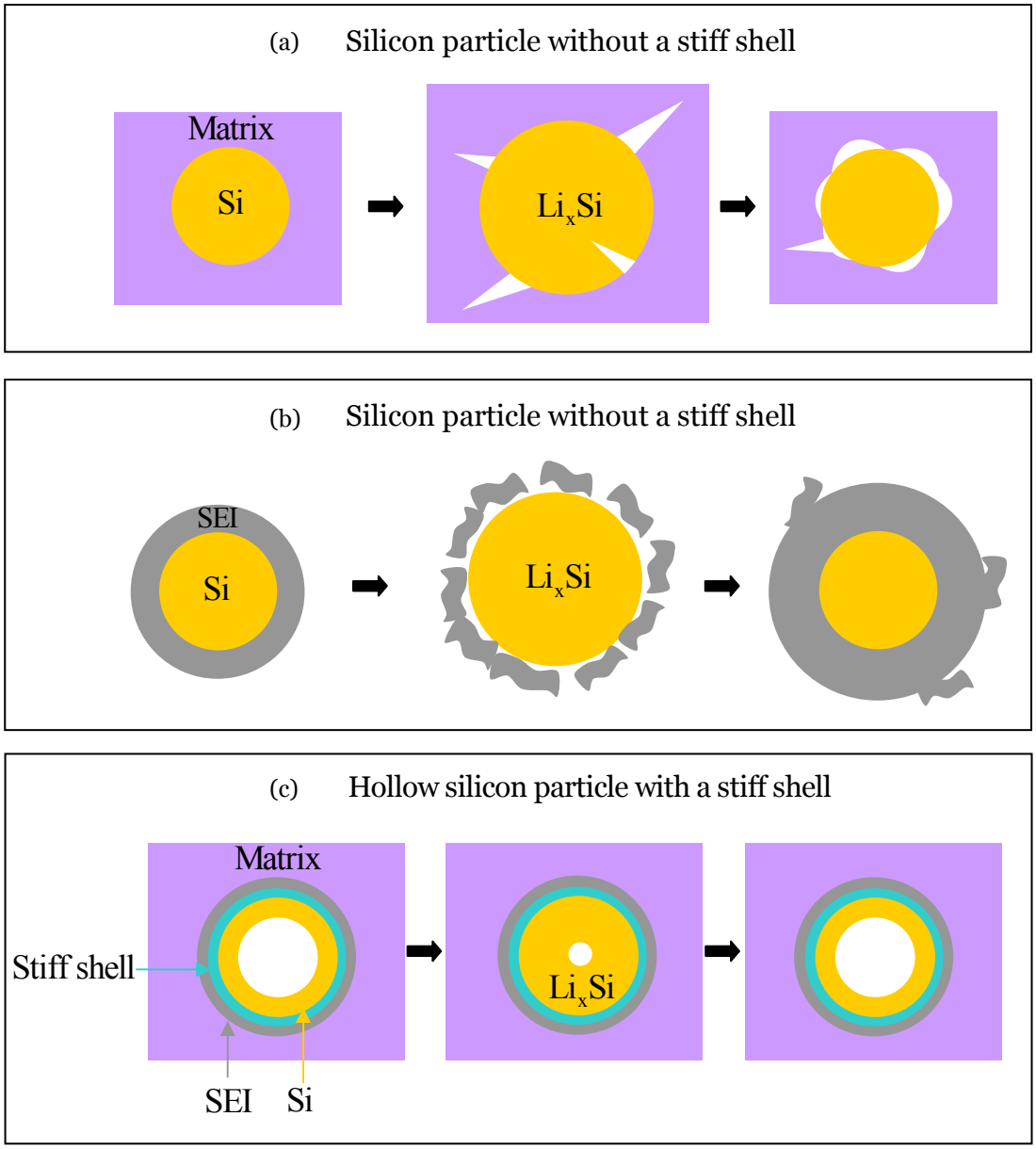

Figure 5. 1. (a). For a silicon particle without a stiff shell, the stress induced by lithiation and delithiation may cause fracture of the active particle, or debonding between the active particle and the matrix, leading to the loss of the conduction path for electrons. (b). Also for a silicon particle without a stiff shell, the deformation associated with lithiation and delithiation may cause the shedding and re-forming of the solid-electrolyte interphase (SEI), consuming active materials. (c). For a hollow silicon particle with a stiff shell, the deformation of silicon is accommodated by inward swelling, so that electric contact is maintained, and the shedding of SEI avoided.

Recent experiments show that mechanical failure can be mitigated by using nanostructured silicon anodes, such as nanowires,[21] thin films,[69]-[71] hollow nanoparticles,[72] and nanoporous structures.[51] These structures alleviate the stress

by managing the deformation through shape optimization and geometric restrictions. Furthermore, intense efforts are being dedicated to stabilizing the SEI layer during lithiation cycles. Current methods include coating a thin artificial SEI layer on the surface of silicon[73]-[79] and using electrolyte additives to avoid the continual consumption of active materials.[80]-[84]

A recent design of electrodes involves hollow core-shell nanostructures, which can enhance the mechanical and chemical stability of silicon anodes simultaneously, Figure 5. 1 (c). Such structures enable silicon electrodes to sustain over six thousand cycles with high coulombic efficiency.[85] In a hollow core-shell nanostructure, the shell separates the electrolyte and the electrode (core), and forces the core to swell into the hollow space in the interior of the structure. Because the shell restricts outward swelling of the core, the continual SEI shedding and re-forming is suppressed, and the electric contact between the electrode and the matrix is maintained. Similar designs based on encapsulating silicon nanoparticles within hollow carbon shells show promise for high-capacity electrodes with long cycle life of hundreds of cycles. [86]-[88]

Constrained lithiation and delithiation, however, induce stress in the hollow core-shell structures. During lithiation, Figure 5. 2 (a), the core is under compressive stresses, and the shell is under tensile hoop stress. Such tensile stress can initiate fracture in the shell. During delithiation, Figure 5. 2 (b), the radial stress can be tensile in both the core and the shell. Such stress may cause interfacial debonding.

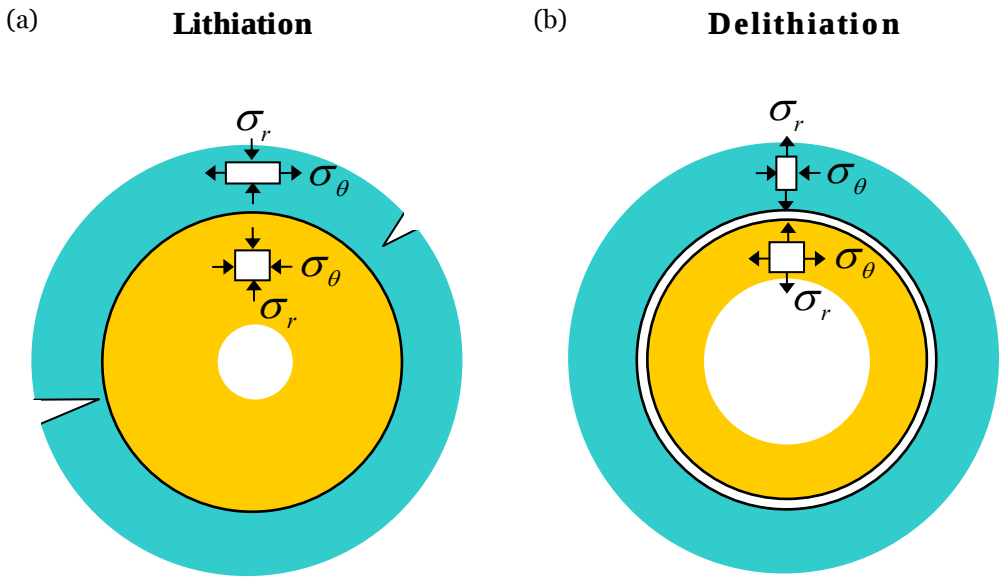

Figure 5. 2. Two potential modes of failure in a hollow silicon particle coated with a stiff shell. (a). The lithiation of the silicon particle induces tensile hoop stress in the shell, which may cause the shell to fracture. (b) The delithiation of the silicon particle induces radial tensile stress, which may cause debonding between the core and the shell.

To facilitate Li diffusion and reduce overall weight, the ideal stiff shell should be thin. However, an extremely thin shell is unable to constrain the outward expansion of the core. The insertion reaction causes large deformation in the core, but the magnitude of the stress is kept manageable by plastic flow. Here we calculate the stress field resulting from the concurrent insertion reaction and plastic flow in hollow spherical nanoparticles and nanowires of silicon coated with stiff shells. We identify conditions to avoid fracture and debonding in terms of the radius of the core, the thickness of the shell, and the state of charge. We further identify the driving forces for the lithiation reaction and discuss the effect of the stress field on the electrochemical reaction.

5.2 Stresses in coated hollow spherical particle of Si

In a hollow core-shell structure, the stiff shell forces the core to swell into the inner hollow space (Figure 5. 3). Before absorbing any Li, the inner radius of the hollow particle is *A*, and the outer radius is *B*. The particle is coated by a stiff shell of outer radius *C*. We consider the case where the rate of lithiation is slow relative to diffusion of Li in the core, so that Li atoms have enough time to homogenize in the core. To completely fill the hollow space upon full lithiation, the structure should satisfy the geometric relation:

$$\frac{A}{B}=\left(\frac{\beta-1}{\beta}\right)^{1/3}, \tag{5.1}$$

where the volumetric swelling ratio $\beta = V_f / V_i$, with V_f representing the fully lithiated volume and V_i the initial volume of the lithium-free state. Lithiation of silicon causes a volumetric swelling $\beta = 4$, so that $A/B = (3/4)^{1/3}$.[17]

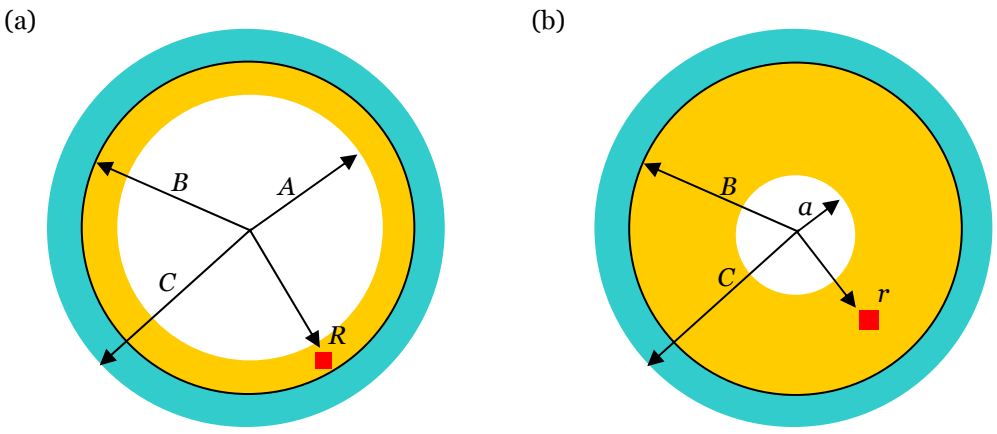

Figure 5. 3. (a). In the reference state, a hollow particle of an electrode is stress-free and Li-free. (b) In the current state, the particle is partially lithiated. The deformation of the core is accommodated by the inner hollow space. Outward deformation is restricted by the shell.

We take the stress-free and Li-free state as the reference state, Figure 5. 3 (a). At time *t*, the hollow particle absorbs some Li, retaining its spherical symmetry. We assume that the outward expansion of the core is completely constrained by the stiff

shell. Note that the elastic deformation of the shell, typically less than 1%, is much less than the lithiation-induced strain in the silicon core. With this assumption, lithiation changes only the inner radius a, and we neglect any deformation of the shell, Figure 5. 3 (b). We represent a material element in the reference state by its distance *R* from the center. At time *t*, it moves to a place a distance *r* from the center. The function *r(R, t)* specifies the kinematics of the deformation. Each material element in the hollow core is subject to a state of triaxial stresses, $(\sigma_r, \sigma_\theta, \sigma_\theta)$, where σ_r is the radial stress and σ_θ the hoop stress. The stresses are inhomogeneous, represented by functions $\sigma_r(r,t)$ and $\sigma_\theta(r,t)$. The balance of forces acting on a material element requires that

$$\frac{\partial \sigma_r(r,t)}{\partial r} + 2\frac{\sigma_r(r,t) - \sigma_\theta(r,t)}{r} = 0. \tag{5.2}$$

We adopt the commonly used idealization that plastic deformation is unaffected when a hydrostatic stress is superimposed. Furthermore, the yield strength of the lithiated silicon, σ_Y, is taken to be constant and independent of the amount of deformation and the concentration of Li. Because the elastic strain is negligible compared to the lithiation-induced strain, the elasticity of the hollow core is neglected. During lithiation, a material element of silicon is under compression in the hoop direction and is in the state $\sigma_r - \sigma_\theta = \sigma_Y$. Setting $\sigma_r - \sigma_\theta = \sigma_Y$ in Eq. (5. 2) and integrating over *r* with the traction-free boundary condition, $\sigma_r(a, t) = 0$, the radial stress in the hollow core is given by

$$\sigma_r = -2\sigma_Y \log\frac{r}{a}, \qquad a \le r \le B \tag{5.3}$$

The hoop stress in the hollow core is determined by $\sigma_r - \sigma_\theta = \sigma_Y$, giving

$$\sigma_\theta = -\sigma_Y\left(2\log\frac{r}{a}+1\right), \qquad a \le r \le B. \tag{5.4}$$

The stress fields in the elastic shell take the familiar solutions of Lamé problems,[89] with the radial stress

$$\sigma_r = -2\sigma_Y\left(\log\frac{B}{a}\right)\left(\frac{B^3}{C^3-B^3}\right)\left(\frac{C^3}{r^3}-1\right), \quad B < r \le C, \tag{5.5}$$

and the hoop stress

$$\sigma_\theta = 2\sigma_Y\left(\log\frac{B}{a}\right)\left(\frac{B^3}{C^3-B^3}\right)\left(\frac{C^3}{2r^3}+1\right), \quad B < r \le C. \tag{5.6}$$

During delithiation, a material element of the hollow core is under tension in the hoop direction, and is in the state $\sigma_r - \sigma_\theta = -\sigma_Y$. Setting $\sigma_r - \sigma_\theta = -\sigma_Y$ in Eq. (5. 2) we obtain the radial stress in the hollow core by integrating over *r*,

$$\sigma_r = 2\sigma_Y \log\frac{r}{a}, \qquad a \le r \le B, \tag{5.7}$$

and the hoop stress,

$$\sigma_\theta = \sigma_Y\left(2\log\frac{r}{a}+1\right), \qquad a \le r < B. \tag{5.8}$$

A comparison of the stress fields indicates a jump in both the radial and hoop stresses from lithiation to delithiation, as shown in Figure 5. 4. These jumps are caused by neglecting the elastic strain. Should we include the elastic strain, the stresses would make this transition from compressive to tensile yielding after the removal of a very small amount of Li.

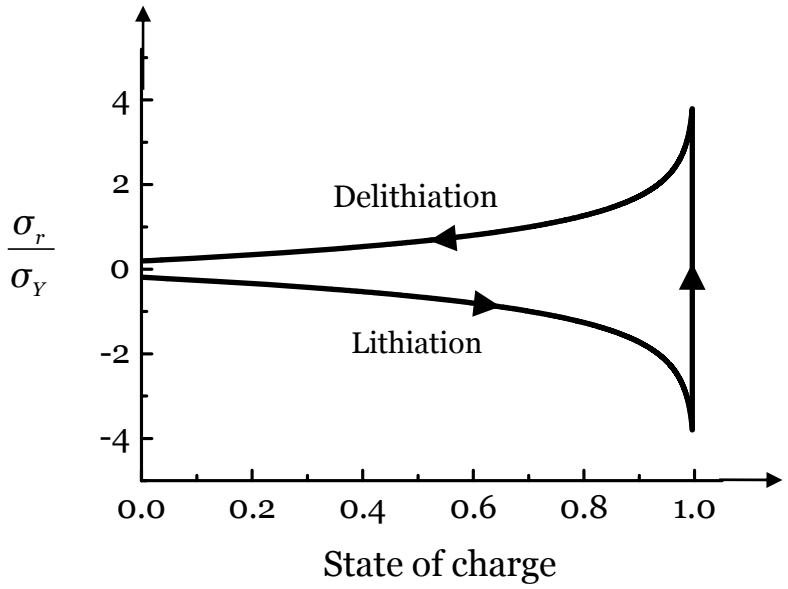

Figure 5. 4. Evolution of the radial stress at the interface between the particle and the shell during lithiation and delithiation.

Mechanical failure is mainly due to the stress at the interface between the core and shell. Figure 5. 4 plots the evolution of the radial stress at the interface of the hollow core during lithiation and delithiation. The stress is plotted as a function of the state of charge (SOC) – 0 represents the Li-free state, and 1 the fully lithiated state. Given the geometric condition in Eq. (5. 1), the state of charge is calculated by using the inner radius a at a given state,

$$SOC = \frac{A^3 - a^3}{A^3}. \tag{5.9}$$

As expected, the hollow core is under compression in the radial direction during lithiation. The compressive stress increases logarithmically with the state of lithiation, Eq.(5. 3). Because of the triaxial state of stress, the magnitudes of the components of the stress readily exceed the yield strength of lithiated silicon.[90] Such big compressive stresses in the core can cause a large tensile hoop stress in the outer shell, which may lead to fracture of the shell. During delithiation, the core-shell

interface is under tensile stress in both the radial and hoop directions. The magnitudes of the stress components are maximized at the beginning of the delithiation, and gradually decrease with the state of delithiation. The tensile stress in the radial direction may initiate interfacial debonding, resulting in a loss of electrical contact between the active core and the surface coating.

5.3 Fracture and debonding analysis

We now analyze fracture of the coating using an approach similar to that described in several recent papers.[15]-[16] We focus on fracture of the coating caused by the tensile hoop stress during lithiation. Linear elastic fracture mechanics is adopted. The reduction in the elastic energy associated with a crack advancing a unit area defines the energy release rate G_f. Dimensional analysis dictates that the energy release rate should take the form

$$G_f = Z\frac{\sigma_\theta^{\,2}}{E_s}(C-B), \tag{5.10}$$

where E_s is Young's modulus of the shell, Z a dimensionless parameter to be determined by solving the elastic boundary-value problem, σ_θ the stress in the hoop direction given by Eq. (5. 6), and $C-B$ the thickness of the surface coating. In the case of a channel crack in the thin shell, $Z=2$ is a typical value.[44] Inserting this value of Z and Eq. (5. 6) into Eq. (5. 10) gives an analytical solution of the energy release rate

$$G_f = \frac{8\sigma_Y^{\,2}}{E_s}\left(\log\frac{B}{a}\right)^2\left(\frac{B^3}{C^3-B^3}\right)^2\left(1+\frac{C^3}{2B^3}\right)^2(C-B), \tag{5.11}$$

where we have approximated $r \approx B$ since $B \gg C - B$. In this limit, Eq. (5. 11) can be further approximated as

$$G_f \approx 2\frac{\sigma_Y^{\,2}}{E_s}\left(\log\frac{B}{a}\right)^2 \frac{B^2}{C-B}. \tag{5.12}$$

The energy release rate is proportional to the square of the yield strength of lithiated silicon, the compliance of the surface coating, the ratio of the sizes of core and shell, and the size of the core. Therefore, to minimize the energy release rate, it is desired to have a small and soft hollow core and a thick and stiff surface shell. However, the shell also needs to be thin to minimize weight and to allow for fast diffusion of Li through its thickness.

We take the same approach for the analysis of interfacial debonding. We assume a pre-existing crack of a size comparable to the thickness of the shell, $C - B$. Here we consider that the energy release rate of debonding is mainly attributed to mode I fracture caused by the tensile radial stress. As such, the energy release rate may be reduced to a simple form,

$$G_d = \pi\frac{\sigma_r^{\,2}}{E_e}(C-B). \tag{5.13}$$

The value of the numerical pre-factor in (5. 13) is approximate, which changes somewhat with the elastic mismatch between the shell and the core, and with the relative length of the crack to the thickness of the shell. Accurate values of the factor can be calculated by solving the boundary-value problem using the finite-element method.[61] In this work, however, a particular value is used to illustrate the main ideas. The radial stress during delithiation is given by Eq. (5. 7), and thus

$$G_d = 4\pi \frac{\sigma_Y^{\,2}}{E_e}\left(\log\frac{B}{a}\right)^2 (C-B). \tag{5.14}$$

Here E_e is the effective modulus that accounts for the effects of inhomogeneous properties of the core and shell. A typical relation is represented by

$$\frac{1}{E_e} = \left(\frac{1}{E_c} + \frac{1}{E_s}\right)/2. \tag{5.15}$$

where E_c is the modulus of the core, and E_s the modulus of the shell.[44] Comparing Eq. (5. 12) and (5. 14), we can see some interesting differences. Namely, the energy release rate for interfacial debonding is seen to scale directly with the shell thickness while the energy release rate for fracture of the shell scales inversely with the shell thickness. Furthermore, the energy release rate for debonding scales much more slowly with the core radius, B, than does the energy release rate for fracture of the shell.

Let Γ_f be the fracture energy of the shell, and Γ_d the interfacial energy between the core and the shell. No preexisting flaws will advance if the maximum energy release rate is less than the fracture energy. Therefore, $G_f = \Gamma_f$ defines the critical condition for initiation of fracture of the shell, and $G_d = \Gamma_d$ defines the critical condition for initiation of interfacial debonding.

Recent experiments indicate that a thin layer of Al_2O_3 deposited on silicon anodes by atomic layer deposition provides excellent improvement of the cycling stability of silicon anodes.[75], [77] Here we take the example of a hollow spherical particle of silicon coated with a thin shell of Al_2O_3 to illustrate the above analysis. Representative values of lithiated silicon and Al_2O_3 are taken, $\sigma_Y = 1$ GPa [52]

and $E_c = 12$ GPa for lithiated silicon,[91], [92] $E_s = 300$ GPa, $\Gamma_f = 40$ J/m^2,[93] and $\Gamma_d = 1$ J/m^2.

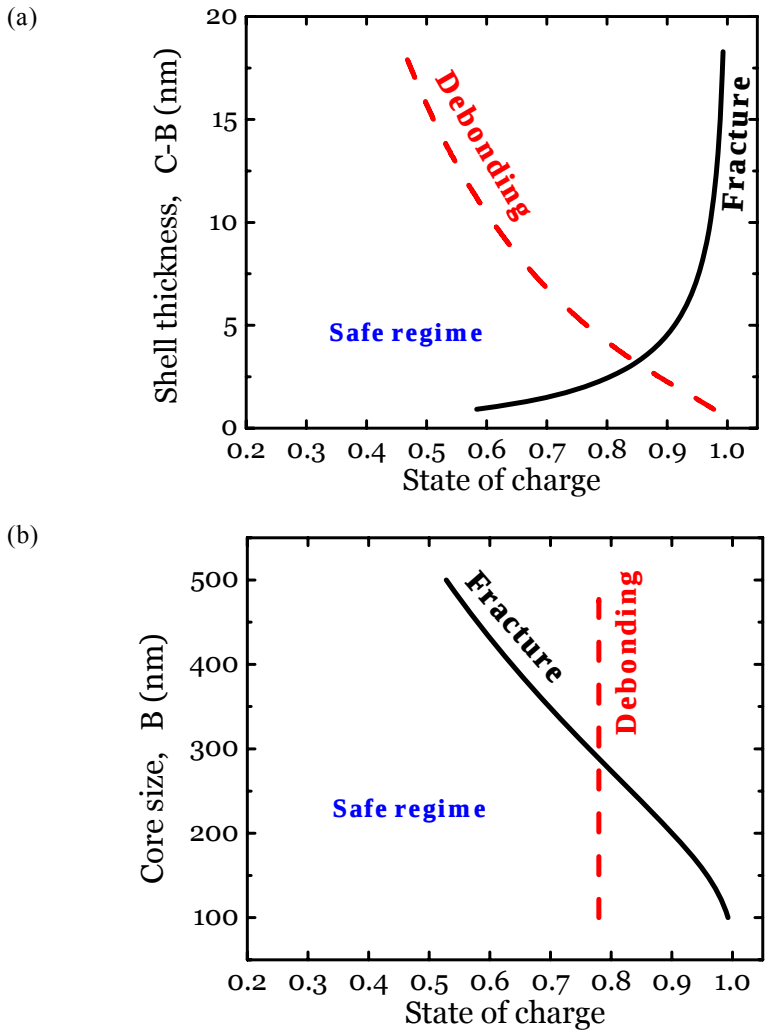

Figure 5. 5. Conditions of fracture and debonding for a spherical hollow particle plotted in the plane of (a) the thickness of the shell and the state of charge, and (b) the radius of the particle and the state of charge.

We first construct a phase diagram to show the effects of the thickness of the shell and the state of charge, Figure 5. 5 (a). We take a typical value of the silicon core size, $B = 200$ nm and $A/B = \sqrt[3]{3/4}$. The thickness of Al_2O_3, $C - B$, is varied. The state of charge is calculated from Eq. (5. 9). The solid black line represents the critical conditions for fracture of the shell, corresponding to the condition $G_f = \Gamma_f$, and the

red dashed line represents the critical conditions of interfacial debonding, corresponding to the condition $G_d = \Gamma_d$. These two lines delineate an upper boundary to the safe regime in which no fracture of the surface coating or interfacial debonding would occur. Figure 5. 5 (b) further plots a phase diagram to show the effects of core size and state of charge. In this case, the thickness of the Al_2O_3 shell is fixed, $C - B = 5$ nm, and the core size B is varied while maintaining the geometric relation $A/B = \sqrt[3]{3/4}$. Given the analytical solutions in Eq. (5. 11) and Eq. (5. 14), phase diagrams for other experimental conditions can be readily constructed.

5.4 Analysis of coated hollow Si nanowires

One dimensional nanowires and nanotubes are emerging designs that can mitigate the mechanical failure of silicon electrodes. In particular, Y. Cui and co-workers illustrate that coated hollow nanowires enable silicon anodes to sustain over six thousands cycles with high coulombic efficiencies.[85] Such excellent performance would ultimately meet the requirement of commercializing silicon into electric vehicles. In this section, we analyze fracture and debonding of a hollow nanowire. The cross-section is as shown in Figure 5. 3. For complete utilization of the available hollow volume upon full lithiation, we must satisfy the geometric relation:

$$\frac{A}{B} = \left(\frac{\beta - 1}{\beta}\right)^{1/2}, \tag{5.16}$$

where for silicon $\beta = 4$ and $A/B = (3/4)^{1/2}$.

Similar to the case of spherical particles, lithiation of silicon causes a tensile hoop stress in the shell, which may fracture the coating material. Furthermore, a

large tensile radial stress is developed at the beginning of delithiation, which may initiate interfacial debonding. We derive the stress field in the Appendix B. Since the deformation of the core along the axial direction is constrained by the shell, lithiated silicon is assumed to deform under plane-strain conditions. The analytical solution of fracture energy release rate of the shell during lithiation is given by

$$G_f = \frac{8}{3}\frac{\sigma_Y^{\,2}}{E_s}\left(\log\frac{B}{a}\right)^2\left(\frac{B^2}{C^2-B^2}\right)^2\left(1+\frac{C^2}{B^2}\right)^2(C-B). \tag{5.17}$$

In the case of $C \approx B$, Eq. (5. 17) can be further approximated as

$$G_f \approx \frac{8}{3}\frac{\sigma_Y^{\,2}}{E_s}\left(\log\frac{B}{a}\right)^2\frac{B^2}{C-B}. \tag{5.18}$$

And the interfacial fracture energy during delithiation is given by

$$G_d = \frac{4\pi}{3}\frac{\sigma_Y^{\,2}}{E_e}\left(\log\frac{B}{a}\right)^2(C-B). \tag{5.19}$$

Comparing the fracture energies in the spherical particle and the nanowire, we find that the energy release rate for fracture of the shell is a factor of 4/3 larger for the nanowire than for the sphere. In contrast, energy release rate for interfacial debonding is 3 times larger in the sphere than in the nanowire.

We now consider the practical example of a hollow silicon nanowire coated with a thin layer of Al_2O_3. A phase diagram showing the effects of the thickness of the shell and the state of charge is given in Figure 5. 6 (a).

(a)

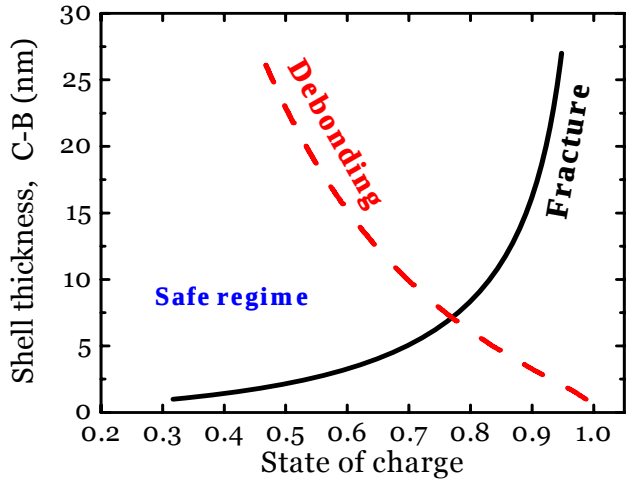

(b)

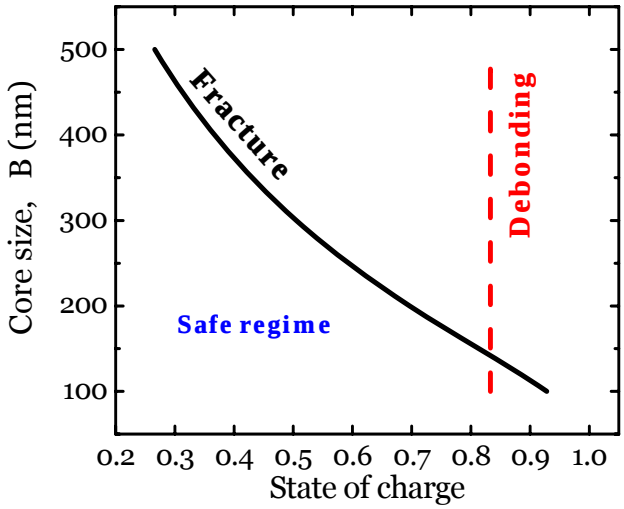

Figure 5. 6. Conditions of fracture and debonding for a hollow nanowire plotted in the plane of (a) the thickness of the shell and the state of charge, and (b) the radius of the particle and the state of charge.

In the nanowires, the state of charge is calculated by

$$SOC = \frac{A^2 - a^2}{A^2}. \tag{5.20}$$

The silicon core size is taken as $B = 200$ nm and $A/B = (3/4)^{1/2}$. The thickness of Al_2O_3, $C - B$, is varied. The solid black line corresponds to the critical conditions of fracture of the shell, given by $G_f = \Gamma_f$, and the red dashed line corresponds to the critical conditions for interfacial debonding, given by $G_d = \Gamma_d$. Figure 5. 6 (b) shows a phase diagram demonstrating the effects of the core size and state of charge. In this case,

the thickness of the Al_2O_3 shell is taken as $C - B = 5$ nm, and the core size B is varied while maintaining the geometric relation $A/B = \sqrt{3/4}$. More accurate measurements of Γ_d are needed to produce a more accurate plot. In the case where the interfacial fracture energy Γ_d is less than the value we have used here, the red dashed lines in Figure 5. 5 and Figure 5. 6 would shift to a lower state of charge limit.

5.5 Stress effect on the lithiation reaction

We now identify the driving forces for the lithiation reaction of silicon, namely, the change of free energy associated with the reaction. Let ΔG_r be the free energy of the lithiation reaction of silicon when both the stress and the applied voltage vanish. Assume the silicon anode is connected to a cathode by a conducting wire through a voltage source. Associated with converting one Li atom and Si into lithiated silicon, one electron passes through the external wire, so that the voltage source does work $e\Phi$, where Φ is the voltage, and e the elementary charge (a positive quantity). The driving force is further modified when the stress effect is included. During lithiation of the coated hollow silicon particle, Li atoms migrate into Si by overcoming an energy barrier induced by the compressive stress in the core. Thus, when one Li atom is incorporated into lithiated silicon, the stress does work $-\Omega\sigma_m$, where σ_m is the mean stress in the core, and Ω is the change in volume caused by insertion of one Li atom. Here we assume an isotropic swelling of Si caused by Li insertion such that only the contribution from the mean stress is included. We also consider small elastic deformation of lithiated silicon such that stress terms of higher orders can be

neglected.[94] Combining the above contributions, we find that, when the reaction advances, the net change in the free energy is

$$\Delta G = \Delta G_r - e\Phi - \Omega\sigma_m . \tag{5.21}$$

We have neglected the dissipation at the electrolyte/electrode interfaces, as well as inside the electrodes and electrolytes. In our sign convention, a negative ΔG drives lithiation, and a more negative value represents a larger driving force. The free energy of reaction ΔG_r takes a negative value. The sign of $e\Phi$ depends on the polarity. We consider Φ being positive in the direction that drives lithiation. As expected, a compressive mean stress at in silicon retards lithiation.

For both the spherical silicon particles and nanowires, the analytical solutions of the stress fields are given in the prior sections. Inserting the stresses into Eq. (5. 21), we can quantify the effect of stress on the lithiation reaction. We note that the compressive stress is maximized at the core-shell interface. Thus, the retarding effect of stress on the lithiation reaction is most significant at the interface. The contribution due to the stresses at the interface is plotted in Figure 5. 7. In making this plot, we have adopted the value $\Omega = 1.36\times10^{-29}\,\mathrm{m}^3$.[66] As expected, the magnitude of the stress contribution increases with the state of charge. Recall that the free energy of formation of lithiated silicon is small; for example, $\Delta G_r = -0.18\mathrm{eV}$ for amorphous $Li_{2.1}Si$.[95] Consequently, the reaction can readily generate a large enough stress to counteract the electrochemical driving force, stalling the surface reaction prior to complete lithiation. In fact, a lower lithiation capacity due to an incomplete surface reaction has been observed in recent

experiments.[96]

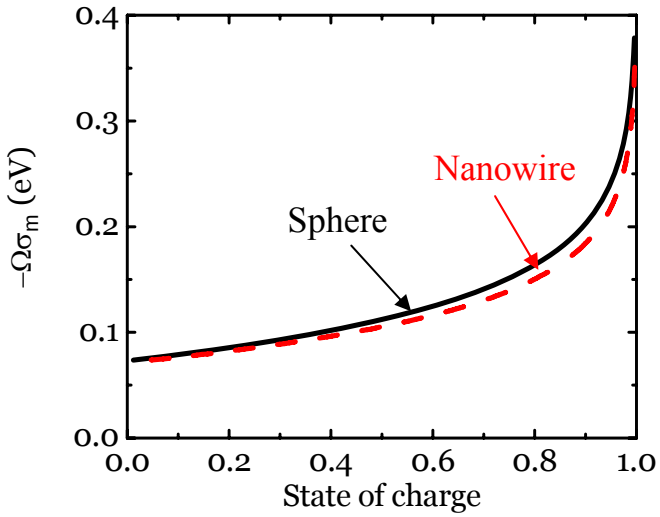

Figure 5. 7. The effect of the stress on the driving force for the lithiation reaction is plotted as a function of the state of charge.

5.6 Summary

We present an analysis of fracture and debonding failure in coated hollow spherical particles and nanowires of silicon anodes. A phase diagram describing the critical structural parameters and operating conditions is constructed, outlining how to avoid fracture of the coating and debonding between the coating and the active material. We further explore the effect of the stress field on the lithiation reaction of silicon. The large compressive stress at the core-shell interface may counteract the electrochemical driving force, leading to a low lithiation capacity. The present results and associated analysis provide insightful guidelines for a viable design of coated hollow nanostructures.

Chapter 6

Fracture in C-Si core-shell nanofibers

This chapter considers another promising anode structure of silicon-carbon nanofibers coaxial sponge. Due to the strong mechanical integrity and improved electronic conductivity, such nanostructure is under intensive development for commercial high-capacity Li-ion batteries. Our collaborator, Dr. Jianyu Huang group at Sandia National Lab, characterized the electrochemical and mechanical behaviors of amorphous silicon coated carbon nanofibers (*a*-Si/CNFs) with *in situ* transmission electron microscopy (TEM). The experimental observations will be briefly introduced in section 2. I will focus on the formulation of an analytical solution of the stress field based on the continuum theory of finite deformation in section 3.

6.1 Introduction

Nano-structuring and compositing are currently being pursued as important strategies to fabricate high performance electrodes for Li-ion batteries (LIBs).[97]-[99] It has been demonstrated that active materials with sufficiently small sizes are able to avert lithiation-induced stress accumulation and fracture,[100]-[102] and to allow fast charging and discharging. Furthermore, the overall performance of an electrode, in terms of higher energy density, power density, and cyclability, could be enhanced by rationally tailoring the mixture of the active materials and additives such as a conducting matrix or structural buffer.[103]-[108]

Amorphous silicon coated carbon nanofibers (*a*-Si/CNFs) composite has several advantages as a promising anode material for LIBs. A combination between the high gravimetric capacity of Si and excellent stability of CNF may boost the overall performance.[109]-[113] Si has the highest theoretical capacity (4200 mAh/g for $Li_{22}Si_5$ at high temperatures[60] or 3579 mAh/g for $Li_{15}Si_4$ at room temperature[114]-[116]), which is nearly ten times higher than that of graphite (372 mAh/g). However, Si undergoes ~ 300% volume expansion during lithiation, often leading to fracture, pulverization, and rapid capacity-fading of the Si-based electrodes.[24] In contrast, carbonaceous anodes exhibit great cyclability with < 10% volume changes upon lithium insertion/extraction. Combining Si and CNF provides tunable capacity, electrical and mechanical properties. In addition, the mass loading can be feasibly increased by repeated stacking, while the thinness of the *a*-Si and the mechanically robustness of the CNF scaffold are maintained for high rate performance and cyclability. Since a single material is unlikely to meet all the requirements at the same time, nanostructured composite materials will be the choice of technique to reach high performance.

6.2 In-situ TEM experiments

The *a*-Si/CNF samples were prepared by coating *a*-Si onto CNFs with chemical vapor deposition (CVD) method (Applied Sciences Inc.). Figure 6. 1 shows a schematic illustration of the *in situ* experimental setup with a half-cell configuration. The *a*-Si/CNF composite nanowires were glued to an aluminum (Al) rod with conductive silver epoxy and were the working electrode. A uniform coating layer of

a-Si was deposited onto the CNF surface. The thickness of the surface *a*-Si coating layer can be controllably varied. Fresh Li metal was loaded onto a tungsten (W) rod in a glove box filled with helium (H_2O and O_2 concentration below 1 ppm) and served as the counter electrode and Li source. The two electrodes were mounted onto a Nanofactory® TEM-scanning tunneling microscopy (STM) holder. A native Li_2O layer was formed on the Li metal during the holder being transferred from the glove box to the TEM column and served as the solid-state electrolyte. Inside the TEM, the Li_2O/Li terminal can be driven by a piezo-positioner to approach the *a*-Si/CNF-Al terminal. Once the contact was established, a negative bias (such as -2 V) was applied to the *a*-Si/CNF electrode to initiate the lithiation process.

Figure 6. 1 (b)-(c) shows the morphology of an *a*-Si/CNF wire before and after lithiation. The thickness of the surface *a*-Si layer increased from ~ 13 nm to 55 nm after lithiation. Lithiation-induced deformation is only accommodated by swelling of the *a*-Si layer, while the deformation of the carbon core is negligible.

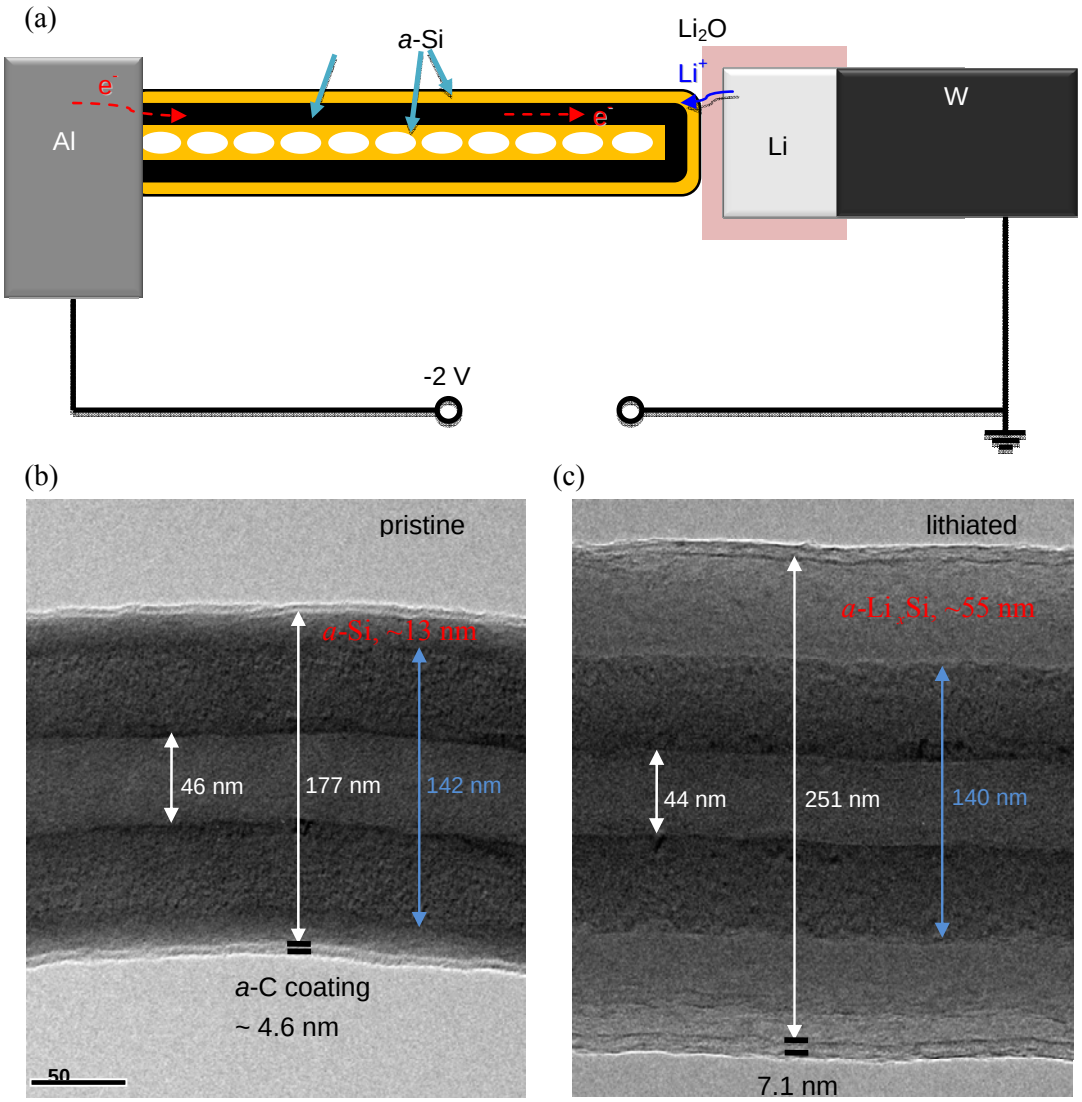

Figure 6. 1. *In situ* experimental setup and typical microstructural changes during lithiation of the amorphous Si on carbon nanofiber (*a*-Si/CNF) anode. (a) Schematic illustration of the half-cell configuration for the *in situ* electrochemical lithiation-delithiation tests inside a TEM. The working electrode is an individual CNF (black) coated with a uniform a-Si layer (yellow). A Li metal on a W probe is the counter electrode, and the native Li_2O layer on Li metal serves as a solid-state electrolyte for Li transport. (b-c) Morphology change of a CNF with uniform Si coating. The Si coating layers was thickened from ~ 13 nm to 55 nm after lithiation, and the CNF core was almost unchanged during lithiation.

Figure 6. 2 shows the typical structural evolution during the lithiation-delithiation cycles. In the first a few cycles, the coated *a*-Si layer underwent nearly reversible volumetric expansion and shrinkage. However, the uniform *a*-Si coating became roughened and showed longitudinal cracks running parallel to the

CNF axis (marked by the red arrows in Figure 6. 2 (e)-(f)). The cracks typically nucleated during the delithiation process (Figure 6. 2 (e)), and became obvious during the following lithiation process (Figure 6. 2 (f)). The surface roughening and crack nucleation during delithiation are due to the plastic flow of lithiated silicon.[90] The electron diffraction patterns indicated that the pristine *a*-Si (Figure 6. 2 (g)) firstly underwent the phase transformation to form *a*-Li_xSi, which might partially or completely crystallize to the *c*-$Li_{15}Si_4$ phase (Figure 6. 2 (h)). The lithiated *a*-Li_xSi or *c*-$Li_{15}Si_4$ phases transformed back to *a*-Si after delithiation (Figure 6. 2 (i)). It should be noted that we did not observe noticeable changes in the diffraction patterns from the CNF, such as the spacing expansion of the basal planes in the graphitic sheets as observed in carbon nanotubes or few-layered graphene, indicating low degree of lithiation in the CNF, which is consistent with the small morphology change.

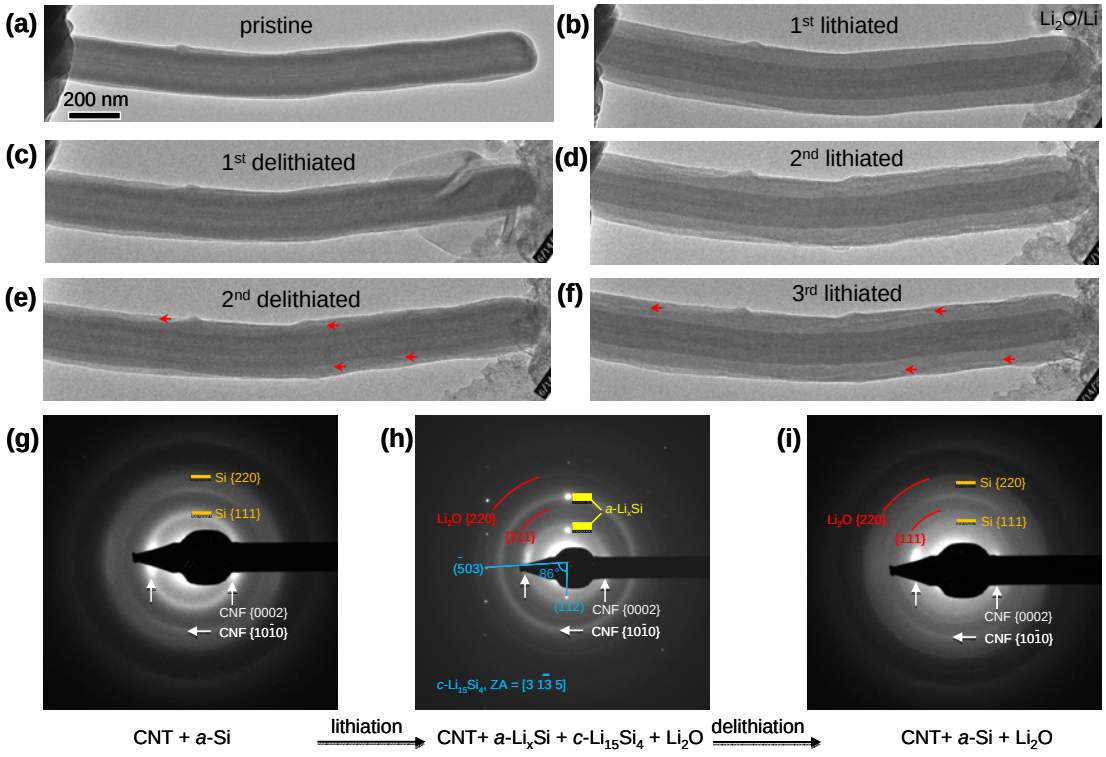

Figure 6. 2. Microstructural changes during the lithiation-delithiation cycles. (a-f)

Figure 6. 2 (Continued) Morphology evolution of an *a*-Si/CNF structure in the first three cycles. The dramatic changes occurred in the surface *a*-Si layer, which swelled and showed a brighter contrast during lithiation. Nano-cracks nucleated during the second delithiation process (e) and became more obvious during the third lithiation process. (g-i) Electron diffraction patterns (EDPs) of the pristine (g), lithiated (h), and delithiated structures (i). Amorphous Li_xSi or crystalline $Li_{15}Si_4$ phases were formed after lithiation, which were converted to *a*-Si after Li extraction.

Figure 6. 3 shows the longitudinal nano-crack formation in the *a*-Si coating layer after cycling. Reversible volumetric changes took place in the lithiation-delithiation cycles (Figure 6. 3 (a)-(k)), and the lithiated phase could be either amorphous (Figure 6. 3 (b), (d), (h)) or crystalline (Figure 6. 3 (f), (j)). Close examination of the structure after cycling reveals nano-cracks (marked by the red arrowheads in Figure 6. 3 (l)) and a sponge-like structure, consistent with the previous results obtained in the liquid-electrolyte-based *in situ* nanobattery or *ex situ* cells.[117]

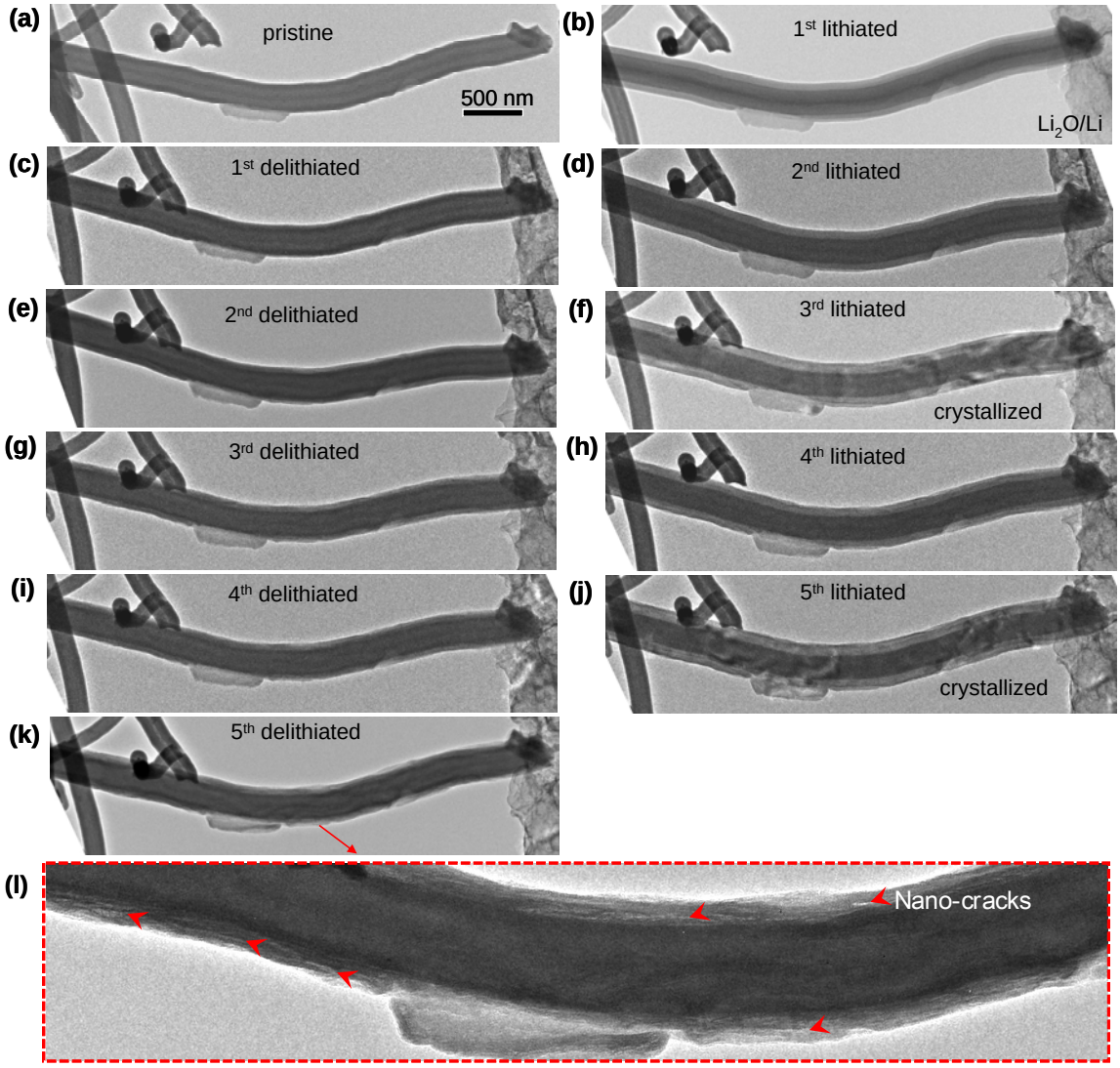

Fig 6. 3. Crack formation after cycling. (a-k) Morphology evolution in the first five lithiation-delithiation cycles. (l) Zoomed-in image of the structure after the fifth delithiation process. The surface coating layer became rough with many nano-cracks and sponge-like morphology.

Interestingly, the nano-cracks were mostly orientated along the longitudinal directions (*i.e.*, parallel to the CNF's axis). Such longitudinal cracks are due to the tensile stress in the hoop direction, which drives the initial flaws (i.e., preexisting cracks) in the axial orientation to propagate. We note that, to accommodate the large volumetric expansion during lithiation cycles, the lithiated silicon must deform plastically. To illustrate the salient feature of the stress field, we consider that the silicon coating is uniformly lithiated. This is not an unreasonable assumption when

the feature size of the silicon shell is small such that the diffusion of Li is fast process through silicon. As the lithiation progresses, the lithiated silicon enlarges. Such expansion is constrained by the carbon core. An element in the curved lithiated silicon undergoes tensile stress in the radial direction, and compressive stresses in the hoop and axial directions. Upon subsequent delithiation, the element unloads elastically, and then deforms plastically in compression in the radial direction, while in tension in the hoop and axial directions. This process can cause the initial flaws in the silicon shell to grow, leading to the fracture of the lithiated silicon. It is worth noting that the fracture event does not necessarily lead to immediate failure of the battery, as long as a good bonding is maintained between the lithiated silicon shell and the conductive carbon backbone. Nevertheless, the fatigue fracture associated with the cyclic plastic deformation of silicon could become a major degradation mechanism of such architecture in the cycle life.

6.3 Stress field in C-Si core-shell nanofibers

We derive the stress field in a silicon-carbon nanofibers coaxial structure using the continuum theory of finite deformation. The geometry is represented in Figure 6. 4 (a). We represent a material element in the reference configuration by its distance R from the center. At time t, the material element moves to a place at a distance r from the center. The function $r(R, t)$ specifies the deformation kinematics. It is noted that the elastic stiffness of CNF is around 10 times that of the lithiated silicon,[91], [118] the deformation of rigid CNFs is neglected. Due to the mechanical constraint

imposed by the CNFs in the axial direction, the lithiated silicon is assumed to deform under the plane-strain conditions. To focus on the main ideas, we neglect the elasticity of the lithiated silicon; we model the lithiated silicon as a rigid-plastic material. Consequently, the expansion of lithiated silicon is entirely due to the lithiation. Consider the shell of the lithiated silicon between the radii *A* and *r*. This shell is lithiated from the shell of pristine silicon between the radii *A* and *R*. We assume that lithium is injected slowly and has sufficient time to diffuse through silicon. The ratio of the volume of the lithiated shell over the volume of pristine silicon, $\tilde{\beta}$, is taken to be homogeneous and evolves in time. Thus,

$$r^2 - A^2 = \tilde{\beta}\left(R^2 - A^2\right). \tag{6.1}$$

This equation gives the function *r(R, t)* once the function $\tilde{\beta}(t)$ is given. That is, $\tilde{\beta}(t)$ fully specifies the kinematics of the silicon shell, $r = \sqrt{A^2 + \tilde{\beta}\left(R^2 - A^2\right)}$. The stretches can be calculated as

$$\lambda_r = \frac{\partial r}{\partial R} = \frac{R\tilde{\beta}}{r}, \quad \lambda_\theta = \frac{r}{R}, \quad \lambda_z = 1. \tag{6.2}$$

We decompose the stretches by writing $\lambda_r = \lambda_r^p \tilde{\beta}^{1/3}$, $\lambda_\theta = \lambda_\theta^p \tilde{\beta}^{1/3}$, $\lambda_z = \lambda_z^p \tilde{\beta}^{1/3}$, where $\tilde{\beta}$ represents the volume change due to the insertion of Li, and the plastic stretch λ^p represents the shape change during lithiation. The volume change $\tilde{\beta}$ has been assumed to be isotropic for amorphous silicon. We can calculate the strain components from the stretches,

$$\varepsilon_r = \log \lambda_r, \quad \varepsilon_\theta = \log \lambda_\theta, \quad \varepsilon_z = \log \lambda_z. \tag{6.3}$$

To calculate the stress field, one has to consider the incremental plastic deformation with respect to time. Given Eq. (6. 2) and (6. 3), we obtain that

$$\delta\varepsilon_r^p = \delta\log\lambda_r - \frac{1}{3}\delta\log\tilde{\beta} = \left(\frac{1}{6} + \frac{1}{2}\frac{A^2}{r^2}\right)\frac{\delta\tilde{\beta}}{\tilde{\beta}},$$
$$\delta\varepsilon_\theta^p = \delta\log\lambda_\theta - \frac{1}{3}\delta\log\tilde{\beta} = \left(\frac{1}{6} - \frac{1}{2}\frac{A^2}{r^2}\right)\frac{\delta\tilde{\beta}}{\tilde{\beta}}, \tag{6.4}$$
$$\delta\varepsilon_z^p = \delta\log\lambda_z - \frac{1}{3}\delta\log\tilde{\beta} = -\frac{1}{3}\frac{\delta\tilde{\beta}}{\tilde{\beta}}$$

The equivalent plastic strain increment is

$$\delta\varepsilon_{eq}^p = \sqrt{\frac{2}{3}\delta\varepsilon_{ij}^p\delta\varepsilon_{ij}^p} = \frac{\delta\tilde{\beta}}{\tilde{\beta}}\sqrt{\frac{1}{9} + \frac{1}{3}\frac{A^4}{r^4}}\,. \tag{6.5}$$

We adopt the flow rule

$$s_{ij} = \frac{2}{3}\frac{\sigma_Y}{\delta\varepsilon_{eq}^p}\delta\varepsilon_{ij}^p\,, \tag{6.6}$$

where s_{ij} is the deviatoric stress, defined as $s_{ij} = \sigma_{ij} - \frac{1}{3}\sigma_{ii}$, and σ_Y the yield strength of lithiated silicon. Therefore,

$$s_r = \frac{\sigma_Y}{\sqrt{\frac{1}{9} + \frac{1}{3}\frac{A^4}{r^4}}}\left(\frac{1}{9} + \frac{1}{3}\frac{A^2}{r^2}\right),$$
$$s_\theta = \frac{\sigma_Y}{\sqrt{\frac{1}{9} + \frac{1}{3}\frac{A^4}{r^4}}}\left(\frac{1}{9} - \frac{1}{3}\frac{A^2}{r^2}\right), \tag{6.7}$$
$$s_z = -\frac{2}{9}\frac{\sigma_Y}{\sqrt{\frac{1}{9} + \frac{1}{3}\frac{A^4}{r^4}}}$$

and

$$\sigma_r - \sigma_\theta = s_r - s_\theta = \frac{2\sigma_Y}{\sqrt{r^4/A^4 + 3}}\quad. \tag{6.8}$$

Consider the force balance of a material element in lithiated silicon

$$\frac{\partial\sigma_r}{\partial r} + \frac{\sigma_r - \sigma_\theta}{r} = 0\,, \tag{6.9}$$

the radial stress can be obtained by integrating Eq. (6. 9), it gives,

$$\sigma_r = -\frac{\sqrt{3}}{3}\sigma_Y\log\frac{\sqrt{r^4 + 3A^4} - \sqrt{3}A^2}{r^2} + D, \qquad A \le r \le b\,. \tag{6.10}$$

The integration constant D is determined by the traction-free boundary condition, $\sigma_r(b,\ t)=0$, such that

$$\sigma_r=-\frac{\sqrt{3}}{3}\sigma_Y\left(2\log\frac{b}{r}+\log\frac{\sqrt{r^4+3A^4}-\sqrt{3}A^2}{\sqrt{b^4+3A^4}-\sqrt{3}A^2}\right),\qquad A\le r\le b. \tag{6.11}$$

The stresses along hoop and axial directions are obtained by Eq. (6. 8) and (6. 7),

$$\begin{aligned}\sigma_\theta&=-\frac{\sqrt{3}}{3}\sigma_Y\left(2\log\frac{b}{r}+\log\frac{\sqrt{r^4+3A^4}-\sqrt{3}A^2}{\sqrt{b^4+3A^4}-\sqrt{3}A^2}\right)-\frac{2\sigma_Y}{\sqrt{r^4/A^4+3}}\\ \sigma_z&=-\frac{\sqrt{3}}{3}\sigma_Y\left(2\log\frac{b}{r}+\log\frac{\sqrt{r^4+3A^4}-\sqrt{3}A^2}{\sqrt{b^4+3A^4}-\sqrt{3}A^2}\right)-\sigma_Y\left(\frac{1}{\sqrt{r^4/A^4+3}}+\frac{1}{\sqrt{3A^4/r^4+1}}\right)\end{aligned} \tag{6.12}$$

Note that the stresses along the hoop and axial directions are compressive during lithiation. During delithiation, however, theses stresses become tensile, and can be calculated by taking the same approach,

$$\begin{aligned}\sigma_r&=\frac{\sqrt{3}}{3}\sigma_Y\left(2\log\frac{b}{r}+\log\frac{\sqrt{r^4+3A^4}-\sqrt{3}A^2}{\sqrt{b^4+3A^4}-\sqrt{3}A^2}\right)\\ \sigma_\theta&=\frac{\sqrt{3}}{3}\sigma_Y\left(2\log\frac{b}{r}+\log\frac{\sqrt{r^4+3A^4}-\sqrt{3}A^2}{\sqrt{b^4+3A^4}-\sqrt{3}A^2}\right)+\frac{2\sigma_Y}{\sqrt{r^4/A^4+3}}\\ \sigma_z&=\frac{\sqrt{3}}{3}\sigma_Y\left(2\log\frac{b}{r}+\log\frac{\sqrt{r^4+3A^4}-\sqrt{3}A^2}{\sqrt{b^4+3A^4}-\sqrt{3}A^2}\right)+\sigma_Y\left(\frac{1}{\sqrt{r^4/A^4+3}}+\frac{1}{\sqrt{1+3A^4/r^4}}\right)\end{aligned} \tag{6.13}$$

We plot the stress field after delithiation of the silicon shell, Figure 6. 4. (b). Experimental values are taken in the calculations, $A=70$ nm , $b=84$ nm . As aforementioned, the tensile stress in the hoop direction acts as the driving force for the cracks in the longitude directions. A representative value of the yield strength is $\sigma_Y=1.5$ GPa .[52] A representative flaw size is taken to be a fraction of the thickness of the lithiated silicon shell, c = 55 nm. The estimated stress intensity factor is $K=\sigma\sqrt{\pi c}=0.62\ \text{MPa}\sqrt{\text{m}}$. This value may be compared with the fracture

toughness $K_c = \sqrt{\gamma E} = 1.09$ MPa$\sqrt{\text{m}}$, where γ represents the surface energy, with a typical value ~1 J/m^2, and E Young's modulus of the lithiated silicon ~12 GPa as measured in *ex*-situ indentation experiments.[91] Note that the magnitude of the axial stress is slightly larger than that of the hoop stress, but the observed crack is along the axial direction. This difference between the experimental observation and theoretical prediction is unresolved at this writing.

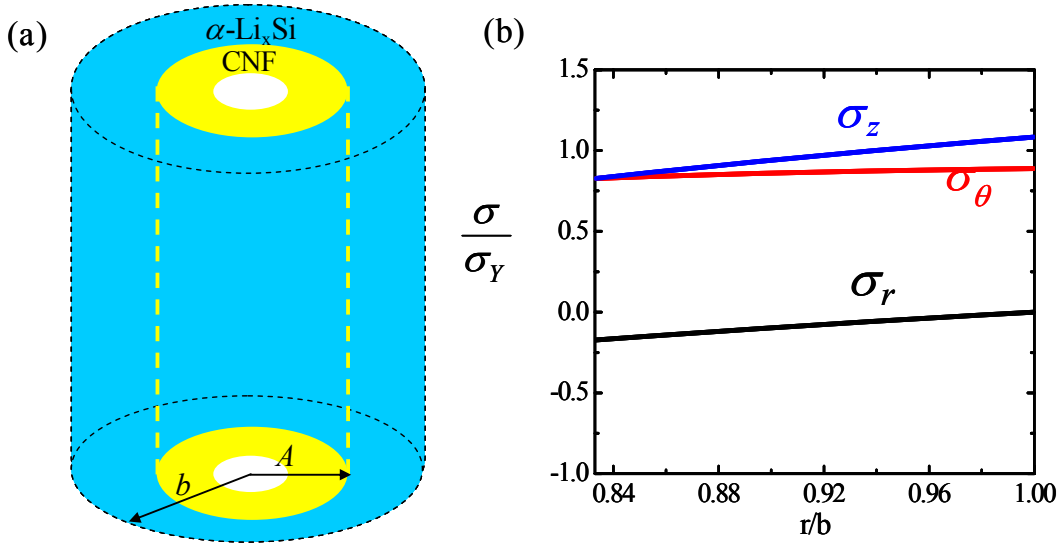

Fig 6. 4. (a) Schematic illustration of an *a*-Si/CNF anode. The radius of carbon core is *A*. Lithiation of the CNF is neglected. During lithiation (delithiation) of the *a*-Si shell, the radius of Si expands to be *b*. (b) Distribution of radial, hoop and axial stresses after delithiation. The stresses are scaled with the yield strength of lithiated silicon σ_Y. Experimental values are taken in the calculations, $A = 70$ nm, $b = 84$ nm.

6.4 Summary

The electrochemical lithiation and corresponding microstructural evolution of the *a*-Si/CNF composite nanowires were studied with *in situ* TEM in a half-cell configuration. Nano-cracks and sponge-like structures were formed after lithiation cycles. Fracture of the shell is attributed to the cyclic plastic deformation of the

lithiated silicon. An analytical solution of the stress field is obtained based on the continuum theory of finite deformation. The observations provide insight into the electrochemical reactions and failure mechanism of the Si/C composite materials for Li-ion batteries.

Chapter 7

Concurrent reaction and plasticity during lithiation of crystalline silicon electrodes

7.1 Introduction

Nanostructured electrodes of silicon are often fabricated with crystalline silicon. In an electrochemical cell, crystalline Si and Li react at room temperature, forming an amorphous phase of lithiated silicon [Figure 7. 1].[114], [115] The reaction front is atomically sharp—the phase boundary between the crystalline silicon and the lithiated silicon has a thickness of ~1 nm.[119] Evidence has accumulated recently that, in the nanostructured electrodes, the velocity of the reaction front is not limited by the diffusion of Li through the amorphous phase, but by the reaction of Li and Si at the front. For example, it has been observed that under a constant voltage the displacement of the reaction front is linear in time.[120] This observation indicates that the rate of lithiation is limited by short-range processes at the reaction front, such as breaking and forming atomic bonds.

That the reaction is the rate-limiting step is perhaps most dramatically demonstrated by lithiated silicon of anisotropic morphologies. Recent experiments have shown that lithiated silicon grows preferentially in a direction perpendicular to the (110) planes of crystalline silicon.[120]-[122] It has been suggested that the anisotropic morphologies are due to the difference in diffusivities along various crystalline orientations of silicon. However, it is well established that the tensor of

diffusivity of a species in a cubic crystal is isotropic.[123] We propose that the observed anisotropic morphologies are due to the variation in the short-range atomic processes at the reaction fronts in different crystallographic orientations.

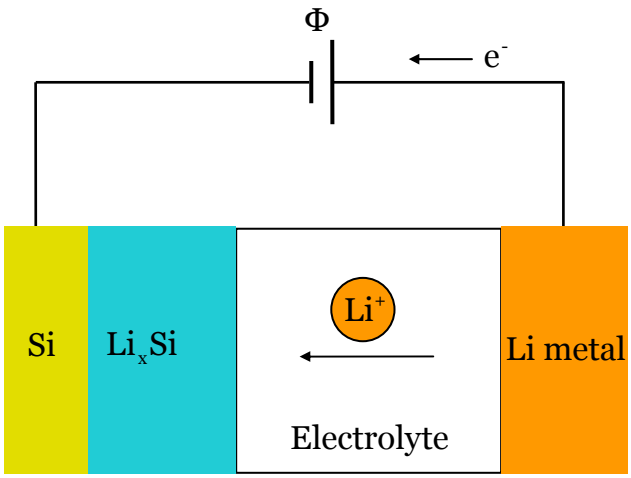

Figure 7. 1. Schematic of an electrochemical test cell composed of a Li metal anode and a crystalline Si cathode. Crystalline Si and Li react at room temperature, forming an amorphous phase of lithiated silicon. The reaction front—the boundary between the crystalline silicon and the lithiated silicon—is atomically sharp.

We further note that, to accommodate the large volumetric expansion associated with the phase transition, the lithiated silicon must deform plastically. It is instructive to compare a flat reaction front with a curved one. When the reaction front is flat [Figure 7. 2 (a)], the large volumetric expansion associated with the reaction is accommodated by elongating the lithiated silicon in the direction normal to the reaction front, while maintaining the geometric compatibility between the two phases in the directions tangential to the reaction front. As the reaction front advances, freshly lithiated silicon is added at the front, and previously lithiated silicon recedes by rigid-body translation, with no deformation. The biaxial stresses in the lithiated silicon remain at the compressive yield strength. When the reaction

front is flat, reaction and plasticity are concurrent and co-locate—right at the reaction front. Indeed, the two processes may not be differentiated without ambiguity.

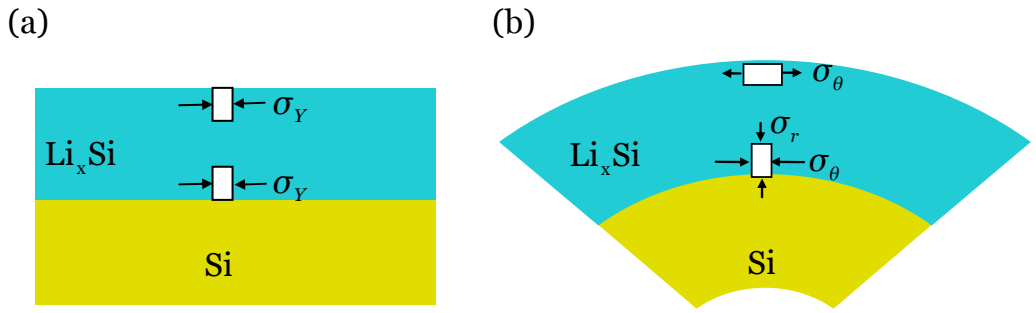

Figure 7. 2. The lithiation of Si causes a large volumetric expansion, which is accommodated by plastic deformation. (a) In a thin film with no curvature, as the reaction front advances, freshly lithiated silicon is added at the front, and previously lithiated silicon recedes by rigid-body translation, with no deformation. The biaxial stresses in the lithiated silicon remain at the compressive yield strength. (b) At a curved reaction front, an element of newly lithiated silicon undergoes compressive plastic deformation in the directions tangent to the reaction front. As the reaction front advances, the element is pushed away from the front, unloads elastically, and then undergoes tensile plastic deformation in the directions tangential to the reaction front. The external surface of the lithiated silicon is subject to tensile hoop stress, possibly leading to fracture.

When the reaction front is curved, the crystalline silicon and the lithiated silicon form a core-shell structure [Figure 7. 2 (b)]. As the reaction front advances, freshly lithiated silicon is added at the front, previously lithiated silicon recedes, and the shell enlarges. An element of lithiated silicon at the curved front initially undergoes compressive plastic deformation in the hoop directions. Upon subsequent lithiation of the core, the element is pushed away from the front, unloads elastically, and then deforms plastically in *tension* in the hoop directions. This process results in tensile hoop stress at the surface of the particle, possibly causing fracture. When the reaction front is curved, reaction and plasticity are concurrent, but can occur at different places. There is no ambiguity in differentiating processes at the reaction front and plastic deformation inside the lithiated silicon.

We present a model of concurrent reaction and plasticity. Existing analyses of lithiation-induced deformation and fracture have assumed diffusion-limited lithiation.[12]-[16], [124]-[127] In this paper, motivated by experimental observations, we assume that the velocity of the reaction front is limited by the rate of the reaction of Li and Si at the front, rather than by the diffusion of Li through the amorphous phase. We identify the driving force for the movement of the phase boundary, and accommodate the reaction-induced volumetric expansion by plastic deformation of lithiated silicon. The model is illustrated by an analytical solution of the co-evolving reaction and plasticity in a spherical particle. We show that lithiation may induce high enough stress to stall the reaction, and that fracture is averted if the particle is small and the yield strength of lithiated silicon is low. Furthermore, we show that the model accounts for recently observed lithiated silicon of anisotropic morphologies.

7.2 A model of concurrent reaction and plasticity

Figure 7. 1 illustrates an electrochemical cell, in which crystalline Si and Li react and form an amorphous phase of lithiated silicon:

$$\mathrm{Li} + \frac{1}{x}\mathrm{Si} = \frac{1}{x}\mathrm{Li}_x\mathrm{Si} \tag{7.1}$$

The two electrodes are connected through a conducting wire and an electrolyte. The conducting wire may be connected to an external voltage source. At the interface between the Li electrode and the electrolyte, Li atoms dissociate into Li ions and electrons. Li ions pass through the electrolyte, and electrons pass through the

conducting wire. Since lithiated silicon is an electron conductor,[128] Li ions and electrons recombine into Li atoms upon reaching the silicon electrode. Li atoms then diffuse through the lithiated silicon, and react with the crystalline silicon—at the reaction front—to form fresh lithiated silicon. The reaction causes the lithiated silicon to grow at the expense of the crystalline Si and metallic Li.

Migration of Li ions in the electrolyte is relatively fast, so that the diffusion of Li through the lithiated silicon and the reaction between Li and Si at the front may limit the velocity of the reaction front. Let D be the diffusivity of Li in the lithiated silicon, V the velocity of the reaction front, and L the thickness of the lithiated silicon. These quantities form a dimensionless group:

$$\chi = \frac{D}{VL}. \tag{7.2}$$

The parameter χ characterizes the relative rate of diffusion and reaction. If χ is large, the diffusion of Li is fast, and lithiation is limited by the reaction. A representative value of diffusivity of Li at room temperature in lithiated silicon is $D = 10^{-16}\,\mathrm{m^2/s}$.[59] A reported velocity of the reaction front of the lithiation of a (100)-Si wafer is $V = 1.2\times10^{-11}\,\mathrm{m/s}$.[119] We note that the reaction velocity may be dependent on the crystallographic directions.[120], [122] So far, a systematic experimental study of such dependence is incomplete. For rates of diffusion and reaction to be comparable, $\chi = 1$, and the thickness of the lithiated silicon is calculated to be $L = 8\,\mu m$. In typical nanostructured electrodes of silicon, the feature size is less than a few hundreds of nanometers.[120]-[122] Thus, for electrodes at such size scales, the velocity of the reaction front is limited by the reaction of Si and Li at the front, rather than by

the diffusion of Li through the amorphous phase.

We next identify the driving force for the reaction, namely, the change in the free energy associated with the reaction that converts one Li atom and $1/x$ number of Si atoms into lithiated silicon. Let ΔG_r be the free energy of reaction (7. 1) when both the stress and the applied voltage vanish. When the conducting wire is connected through a voltage source, associated with converting one Li atom into lithiated silicon, one electron passes through the conducting wire, so that the external voltage source does work $e\Phi$, where Φ is the voltage, and e is the elementary charge (a positive quantity). The driving force is further modified when the two phases, the crystalline silicon and the lithiated silicon, are stressed. (The metallic Li electrode is taken to be stress-free.) Associated with converting one Li atom into lithiated silicon, the crystalline Si phase loses $1/x$ number of Si atoms, and the stress in silicon does work $-\sigma_m^{\mathrm{Si}}\Omega^{\mathrm{Si}}/x$, where σ_m^{Si} is the mean stress in Si at the reaction front, and Ω^{Si} is the volume per Si atom. The amorphous phase gains $1/x$ number of Si atoms and one Li atom, so that the stress in the amorphous phase does work $\sigma_m^{\mathrm{Li_xSi}}\Omega^{\mathrm{Li_xSi}}/x$, where $\sigma_m^{\mathrm{Li_xSi}}$ is the mean stress in the amorphous phase at the reaction front, and $\Omega^{\mathrm{Li_xSi}}$ is the volume per unit of $\mathrm{Li_xSi}$.

Combining the above contributions, we find that, when the reaction advances by converting one Li atom and $1/x$ number of Si atoms into lithiated silicon, the net change in the free energy is

$$\Delta G = \Delta G_r - e\Phi + \frac{1}{x}\left(\sigma_m^{\mathrm{Si}}\Omega^{\mathrm{Si}} - \sigma_m^{\mathrm{Li_xSi}}\Omega^{\mathrm{Li_xSi}}\right). \tag{7.3}$$

We have neglected the dissipation at electrolyte/electrode interfaces, as well as inside

the electrodes and electrolytes. In our sign convention, a negative ΔG drives lithiation, and a more negative value represents a larger driving force. The free energy of reaction ΔG_r takes a negative value. In Figure 7. 1, we have drawn the polarity of the voltage source in the direction that drives lithiation. As expected, a compressive mean stress in the crystalline Si promotes lithiation, but a compressive mean stress in the lithiated silicon retards lithiation.

This net change in the free energy is the driving force for the movement of the reaction front. The velocity of the reaction front will increase as the magnitude of the driving force increases. The reaction is taken to be thermally-activated, described by the familiar kinetic model:[129]

$$V = V_0 \exp\left(-\frac{Q}{kT}\right)\left[\exp\left(-\frac{\Delta G}{kT}\right)-1\right], \tag{7.4}$$

where kT is the temperature in the unit of energy, Q the activation energy, and V_0 a parameter analogous to the exchange current density in a redox process . The velocity of the reaction is taken to be positive when the crystalline Si is consumed and the lithiated silicon grows. When $\Delta G = 0$, the electrochemical cell is in equilibrium, and the reaction halts, $V = 0$. When $\Delta G < 0$, the reaction front advances in the direction that consumes crystalline silicon, $V > 0$. When $\Delta G > 0$, it may seem that the reverse reaction would take place—the lithiated phase would be consumed, Si redeposited at the reaction front, and Li redeposited as Li metal. The reaction front would move in the direction opposite as that during lithiation. However, experiments have suggested that during delithiation ($\Delta G > 0$), the phase boundary remains stationary as Li is removed from the amorphous layer.[119] Thus, the

forward and backward reactions seem to involve distinct kinetic processes. Such complication should be considered in describing an accurate kinetic model. Nevertheless, in the case of $|\Delta G| >> kT$, as is common in these systems at room temperature, the forward reaction is more prominent than the backward one. Thus, the kinetics model of Eq. (7. 4), based on transition state theory, is still approximately valid.

At this writing, the available experimental data are lacking in completeness to substantiate kinetic model of any specific form. As such, in the following sections, we calculate the stress field and simulate the morphology of lithiated silicon with a prescribed velocity field. The considerations in Eq. (7. 3)-(7. 4) may aid the planning of future experiments.

Associated with the reaction (7. 1), the volume of the silicon electrode expands by the ratio

$$\beta = \frac{\Omega^{\mathrm{Li_xSi}}}{\Omega^{\mathrm{Si}}}. \tag{7.5}$$

The lithiation-induced expansion is too large to be accommodated by elastic deformation; rather, the large lithiated-induced expansion is accommodated by plastic deformation of the lithiated silicon.[61], [90] The concurrent reaction and plasticity evolve a field of stress in both crystalline and lithiated silicon. The reaction front is atomically sharp, the amorphous phase attains the fully lithiated state, and the crystalline silicon core remains free of Li. The crystalline silicon is modeled as an elastic material, and the lithiated silicon is modeled as an elastic-plastic material. The elastic-plastic model can be found in the classic text of

Hill.[58]

The models of reaction kinetics and elastic-plastic deformation, in combination, co-evolve the reaction front and elastic-plastic field. At a given time, the location of the reaction front and the elastic-plastic field are known. For a small increment in time, advance the reaction front by an amount following the kinetic model, and then accommodate the reaction-induced volumetric expansion by updating the elastic-plastic field. Repeat the procedure to trace the co-evolution incrementally in time.

7.3 Lithiation of a spherical particle of crystalline Si

To illustrate the salient features of the model, we derive an analytical solution of a spherical particle. A particle of pristine crystalline Si, radius *B*, is taken to be the reference configuration [Figure 7. 3 (a)]. The velocity of the reaction front is taken to be the same everywhere on the front, so that the front remains to be a spherical surface as it advances, and the spherical symmetry is retained. The magnitude of the velocity, however, may change as the reaction progresses. At time *t*, Figure 7. 3 (b), the particle becomes a core-shell structure, with the radius of the crystalline core being A, and the outer radius of the amorphous shell being $b(t)$. The function $A(t)$ specifies the extent of reaction, and the velocity of the reaction front is $V = -dA(t)/dt$. In the reference configuration, an element of crystalline Si is identified by the radius *R*. At time *t*, this element is lithiated and moves to a place of radius *r*. The function $r(R,t)$ specifies the field of deformation. In representing

a field, we may choose either R or r as an independent variable. One variable can be changed to the other by using the function $r(R,t)$. We will indicate our choice in each field explicitly when the distinction is important.

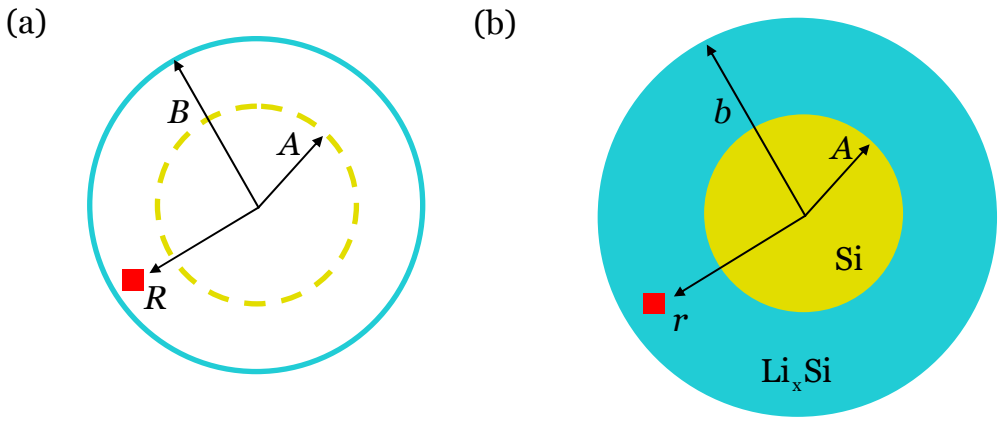

Figure 7. 3. Lithiation of a spherical particle of crystalline Si. (a). The pristine crystalline Si, radius B, is taken as the reference configuration, in which a spherical surface is marked by the radius A, and an element of silicon by the radius R. (b). At time t, silicon in the shell outside the radius A is lithiated, and the element R moves to a new position of radius r.

Elastic strain is much smaller than the volumetric strain associated with the phase transition. To focus on the main ideas, we neglect elastic strains of both phases, and model the crystalline Si as a rigid material, and the lithiated silicon as a rigid-plastic material. Consequently, the expansion of the particle is entirely due to lithiation. Consider the shell of the lithiated silicon between the radii A and r. This shell is lithiated from the shell of the pristine crystalline Si between the radii A and R. The ratio of the volume of the lithiated shell over the volume of the crystalline shell is β, so that

$$r^3 - A^3 = \beta\left(R^3 - A^3\right). \tag{7.6}$$

This equation gives the function $r(R,t)$ once the function $A(t)$ is given. That is, $A(t)$ fully specifies the kinematics of the spherical particle. In particular, the outer radius of the lithiated silicon is obtained by setting $R = B$ in (7. 6):

$$b=\left[A^3+\beta\left(B^3-A^3\right)\right]^{1/3}. \tag{7.7}$$

The radial and hoop stretches can be calculated from

$$\lambda_r=\frac{\partial r\left(R,t\right)}{\partial R},\quad \lambda_\theta=\frac{r\left(R,t\right)}{R}. \tag{7.8}$$

The crystalline core is in a state of homogeneous hydrostatic compression. The stress field in the amorphous shell, however, is inhomogeneous. Each material element in the shell is subject to a state of triaxial stresses. Let σ_r be the radial stress, and σ_θ the hoop stress [Figure 7. 4(a)]. We adopt a commonly used idealization that plastic deformation is unaffected when a hydrostatic stress is superposed. Superposing a hydrostatic stress of magnitude σ_r, we observe that the state of plastic deformation of the element subject to the triaxial stresses is the same as the state of the plastic deformation of the element subject to equal biaxial stresses, $\sigma_\theta-\sigma_r$.

Figure 7. 4 (b) sketches the stress-stretch relation in terms of the stress $\sigma_\theta-\sigma_r$ and the strain $\log\lambda_\theta$. For simplicity, the yield strength of the lithiated phase, σ_Y, is taken to be constant, independent of the amount of deformation and the concentration of Li. An element of newly lithiated Si is compressed in the hoop directions, and is in the state $\sigma_\theta-\sigma_r=-\sigma_Y$. Subsequently, this material element is pushed outward by even newer lithiated silicon, and undergoes elastic unloading. Because the elastic strain is negligible compared to lithiation-induced strain, the elastic unloading is represented by the vertical line in Figure 7. 4 (b). After elastic unloading, and element plastically deforms under $\sigma_\theta-\sigma_r=+\sigma_Y$.

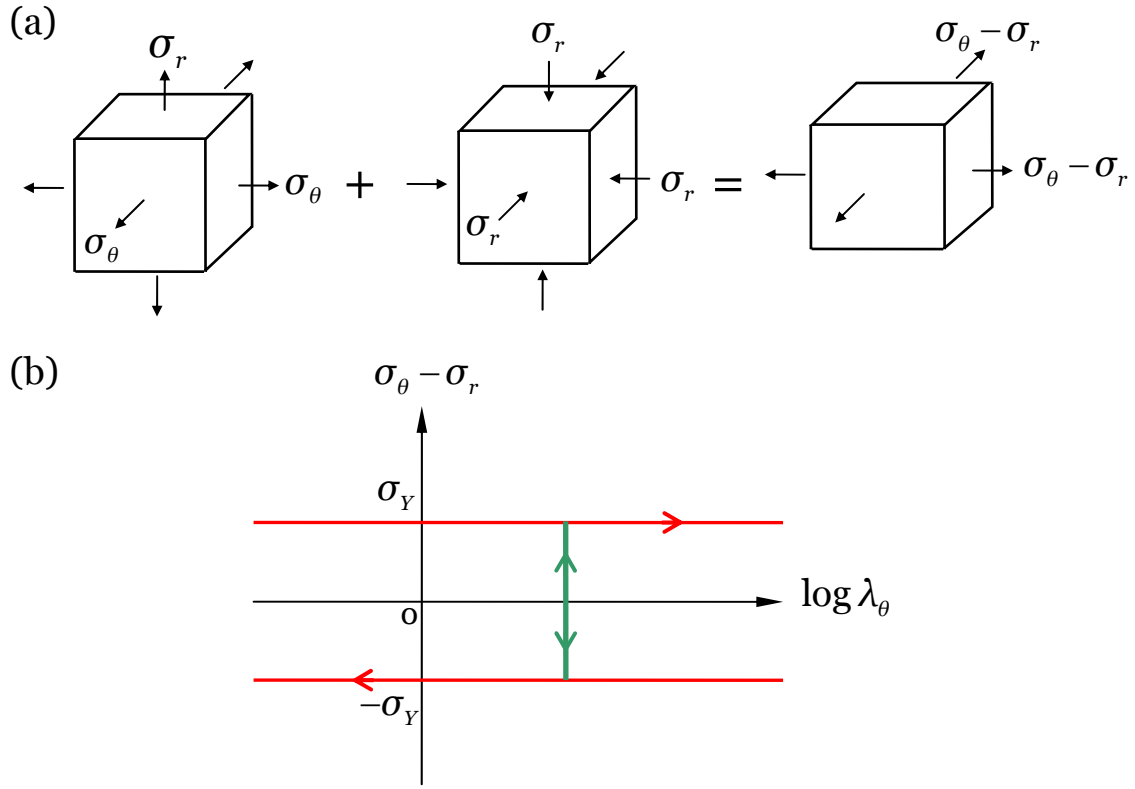

Figure 7. 4. (a) The state of plastic deformation of an element subject to the triaxial stresses $(\sigma_r, \sigma_\theta, \sigma_\theta)$ is the same as that of an element subject to equal-biaxial stresses $\sigma_\theta - \sigma_r$. (b) The stress-strain relation in terms of the stress $\sigma_\theta - \sigma_r$ and the strain $\log \lambda_\theta$. When $\sigma_\theta - \sigma_r = +\sigma_Y$, the plastic deformation is tensile in the hoop direction. When $\sigma_\theta - \sigma_r = -\sigma_Y$, the plastic deformation is compressive in the hoop direction. The elastic strain is negligible compared to lithiated strain, so that elastic part of the stress-strain relation is represented by a vertical line.

The balance of forces acting on a material element requires that

$$\frac{\partial \sigma_r(r,t)}{\partial r} + 2\frac{\sigma_r(r,t) - \sigma_\theta(r,t)}{r} = 0. \tag{7.9}$$

Setting $\sigma_\theta - \sigma_r = \sigma_Y$ in (7. 9) and integrating over r with the traction-free boundary condition, $\sigma_r(b,t) = 0$, we obtain the radial stress in the shell:

$$\sigma_r = -2\sigma_Y \log(b/r), \quad A \le r \le b. \tag{7.10}$$

The hoop stress inside the shell, away from the reaction front, is determined from $\sigma_\theta - \sigma_r = \sigma_Y$, giving

$$\sigma_\theta = \sigma_Y - 2\sigma_Y \log(b/r), \quad A < r \le b . \tag{7.11}$$

As discussed above in connection with Figure 7. 2, in the shell at the reaction front, the element of the freshly lithiated silicon undergoes plastic deformation, which elongates the element in the radial direction. The hoop stress in the element of freshly lithiated silicon is determined from $\sigma_\theta - \sigma_r = -\sigma_Y$, giving

$$\sigma_\theta = -\sigma_Y - 2\sigma_Y \log(b/A), \quad r = A . \tag{7.12}$$

A comparison of (7. 11) and (7. 12) indicates a jump in the hoop stress by magnitude $2\sigma_Y$. This jump is caused by our neglecting the elastic strain. Should we include elastic strain, the hoop stress would make a transition from (7. 12) to (7. 11) within a very thin shell.

As mentioned above, the core is in a state of homogeneous and hydrostatic compression. In order to balance forces, the radial stress is continuous across the reaction front. Setting $r = A$ in (7. 10), we obtain the stress field in the crystalline core:

$$\sigma_r = \sigma_\theta = -2\sigma_Y \log(b/A), \quad r \le A . \tag{7.13}$$

Figure 7. 5 plots the stress field when the reaction front is at $A/b = 0.4$. As expected, the core is in a homogeneous state of hydrostatic compression, but the stress field in the shell is triaxial and inhomogeneous. The radial stress in the shell is compressive, with $\sigma_r(b,t) = 0$ prescribed as the boundary condition. Because of the triaxial state of stress, the magnitude of the stress component readily exceeds the yield strength. The hoop stress is tensile at the external surface of the particle, $\sigma_\theta(b,t) = \sigma_Y$, and gradually becomes compressive inside the shell. Near the reaction

front, the hoop stress jumps by amplitude $2\sigma_Y$, as discussed before.

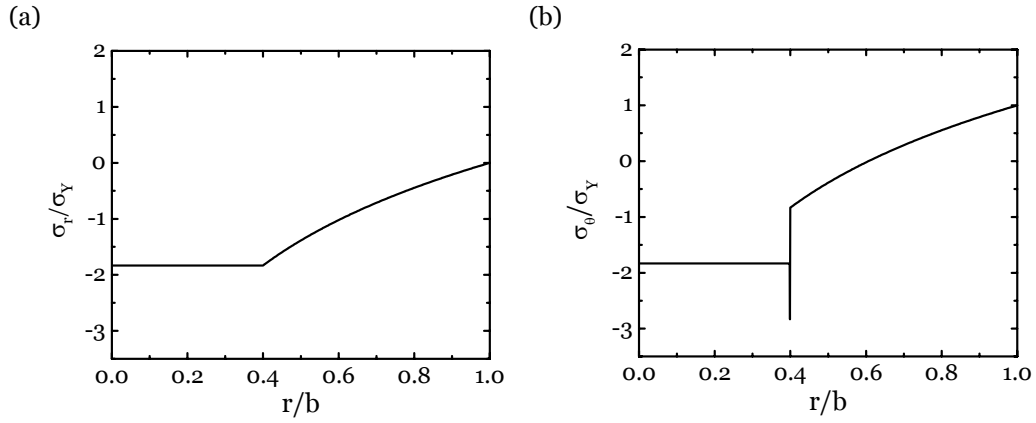

Figure 7. 5. Stress field in a spherical particle when the reaction front is at $A/b=0.4$. (a) radial stress, (b) hoop stress.

For the spherical particle, the field of stress and the field of deformation are fully determined once the radius of the core *A* is specified. We now examine how the stress affects the movement of the reaction front. The mean stress in the crystalline silicon is $\sigma_m^{\mathrm{Si}}=-2\sigma_Y\log(b/A)$. At the reaction front, the mean stress in the lithiated silicon is $\sigma_m^{\mathrm{Li_xSi}}=-2\sigma_Y\log(b/A)-2\sigma_Y/3$. Inserting these expressions into (7. 3), we obtain the driving force for the movement of the reaction front:

$$\Delta G=\Delta G_r-e\Phi+\frac{2\sigma_Y\Omega^{\mathrm{Si}}}{x}\left[(\beta-1)\log\left(\frac{b}{A}\right)+\frac{\beta}{3}\right]. \tag{7.14}$$

The contribution due to the stresses is plotted in Figure 7. 6, where the horizontal axis is the normalized radius of the crystalline core A/b. In making this plot, we have adopted the following values: $\beta=4$,[17] $x=3.75$,[119] $\sigma_Y=1\mathrm{GPa}$,[92] and $\Omega^{\mathrm{Si}}=2.0\times10^{-29}\mathrm{m}^3$.[66] As expected, the contribution due to the stresses is positive and retards lithiation. The magnitude of the contribution increases as the crystalline core shrinks. Recall that the free energy of formation of lithiated silicon

is small; for example, $\Delta G_r = -0.18\text{eV}$ for amorphous $Li_{2.1}Si$.[95] Consequently, the reaction can readily generate large enough stress to counteract the electrochemical driving force, stalling the reaction. Note that the free energy of reaction ΔG_r differs for amorphous Li-Si phases with various Li compositions; the experimental data on such functional dependence is unavailable to date.

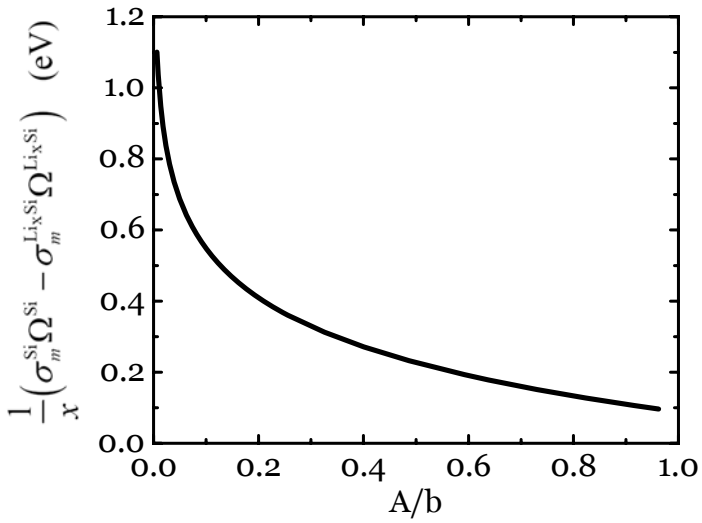

Figure 7. 6. The contribution of the stress to the driving force of lithiation is plotted as a function of the normalized radius of the core.

The curvature of the electrode plays a key role in this contribution of the stress to the free energy. To illustrate this point, consider a flat crystalline Si electrode. In the initial stages of lithiation, the amorphous phase exists as a thin film on a crystalline silicon substrate. As previously mentioned, the biaxial stress in the freshly lithiated silicon is at the compressive yield strength. The stress in the crystalline silicon is zero. Using the same representative values as for the spherical particle, the contribution from the stress to the free energy in (7. 3) is 0.089eV. As with the spherical particle, in a thin film, the stresses retard lithiation. However, the value of this contribution is small compared to the values found for the spherical

particle [Figure 7. 6]. Hence, the curvature can greatly influence the rate of lithiation of crystalline Si.

7.4 Reaction-induced fracture

We now analyze reaction-induced fracture using an approach similar to that described in several recent papers.[15], [16], [61] We focus on fracture caused by the tensile hoop stress during the lithiation of a spherical particle of silicon. A circumferential crack, depth *d*, is assumed to preexist in the particle, as illustrated in Figure 7. 7. We ask if the lithiation-induced stress will cause the crack to grow. The propagation of the crack, should it occur, is assumed to be a much faster process than the plastic flow. Consequently, in analyzing fracture, we assume that no further plastic deformation occurs during the propagation of the crack, and we adopt linear elastic fracture mechanics. The reduction in the elastic energy associated with the crack advancing a unit area defines the energy release rate *G*. Dimensional analysis dictates that the energy release rate should take the form

$$G = Z\frac{\sigma_Y^2}{E}b, \tag{7.15}$$

where *E* is Young's modulus, and *Z* is a dimensionless number to be determined by solving the elastic boundary-value problem. At a given time, once the location and the depth of the crack are given, *Z* is uniquely determined. For the lithiation of a spherical particle, the energy release reaches the maximum value when the particle is fully lithiated, and the length of the crack equals the size of the regime where hoop stress is tensile, $d/b = 0.395$. Therefore, the calculation gives a conservative critical

particle size to avoid fracture. We use the commercial finite-element software ABAQUS to calculate the energy release rate. In the simulation, we input the stress distribution at the fully lithiated state, and the *J*-integral is used to calculate the energy release rate. Our calculation gives $Z = 0.91$.

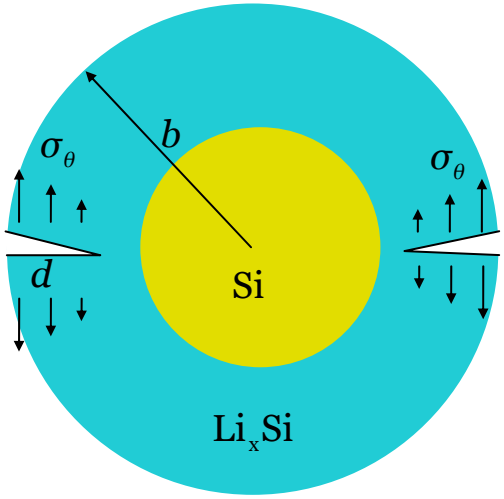

Figure 7. 7. A preexisting circumferential crack in a spherical particle of electrode.

Let Γ be the fracture energy of the particle. No preexisting flaws will advance if the maximum energy release rate is below the fracture energy. Thus, (7. 15) defines a critical particle size:

$$b_{cr} = \frac{\Gamma E}{Z\sigma_Y^2}. \tag{7.16}$$

When the size of the particle is below this critical value, fracture is averted. That is, fracture is averted if the particle is small and the yield strength is low. Taking representative values, $\Gamma = 10\ \text{J/m}^2$,[61] $E = 35\ \text{GPa}$, and $\sigma_Y = 1\ \text{GPa}$,[52] we find that the critical radius of fully lithiation silicon is $b_{cr} = 380\,\text{nm}$. The critical radius of the pristine crystalline silicon is thus $B_{cr} = 239\,\text{nm}$.

7.5 Lithiated silicon of anisotropic morphologies

Recent experiments have shown that electrochemical reaction of crystalline Si and Li produces lithiated silicon of fascinating morphologies.[120]-[122] Lee et al. have fabricated nanopillars of crystalline silicon, of axial orientations <100>, <110> and <111>, all with circular cross sections. On lithiation, the cross sections of these nanopilars evolve into crosses, ellipses and hexagons, respectively.[121] Liu et al. have reported that a nanowire of crystalline silicon, of <112> axial orientation, upon lithiation, evolves into a wire of a dumbbell-shaped cross section.[120] Goldman et al. have fabricated arrays of micron-sized structures of crystalline silicon—bars, posts and platelets—and shown that lithiated silicon grows predominantly along the <110> orientations of silicon, and negligibly along the <111> orientations.[122]

It has been suggested that the anisotropic morphologies are due to the difference in diffusivities along various crystalline orientations of silicon. This suggestion contradicts a mathematical theorem: the tensor of diffusivity of a species in a cubic crystal is isotropic.[123] Instead, we propose that the observed anisotropic morphologies are due to different rates of reaction on various surfaces of crystalline silicon. Lithiation of crystalline silicon is a heterogeneous reaction: Li and Si react on the surfaces of crystalline Si. For this heterogeneous reaction to advance, corporative rearrangement of atoms must occur. Surfaces of silicon in various crystallographic orientations have drastically different atomic structures. It seems plausible that such pronounced dissimilarity in the atomic structures on various surfaces of crystalline surface can readily result in different rates of reaction on these

surfaces.

For heterogeneous reactions involving single crystals, anisotropy in the rates of reaction is a norm, rather than an exception. Lithiation of crystalline Si, however, is of particular interest because this reaction generates an exceptionally large volumetric expansion, and because intriguing experimental observations are being reported. In the absence of a detailed atomistic model of the anisotropy of the lithiation reaction, we proceed as follows, within the model of concurrent reaction and plasticity. We take the experimentally observed anisotropic morphologies as a basis to ascribe different velocities to reaction fronts in different crystallographic orientations. The freshly lithiated silicon at these reaction fronts push previously lithiated silicon, which then undergoes plastic deformation to accommodate the volumetric expansion associated with the freshly lithiated silicon. The concurrent reaction and plasticity evolve the anisotropic morphologies.

To illustrate this model, we simulate the morphological evolution observed during the lithiation of a crystalline silicon nanopillar.[121] Figure 7. 8 (a) shows the cross section of a silicon nanopillar with different crystallographic facets. The diameter of the nanopillar is around 100 nm. The concurrent reaction and plasticity are simulated by using ABAQUS. The lithiation-induced volumetric expansion is simulated as if it were thermal expansion, while deformation in the lithiated silicon is modeled by the elastic-plastic theory. To simulate the movements of the reaction fronts, we prescribe a moving temperature field. The velocity of the front depends on the crystallographic orientation. Following the experimental observation, we

assume that reaction primarily occurs on the (110) crystalline facets. The simulation advances incrementally in time. At a given time, all reaction fronts are at the known positions. The volumetric expansion associated with the freshly lithiated silicon is simulated within ABAQUS by prescribing a change in temperature.

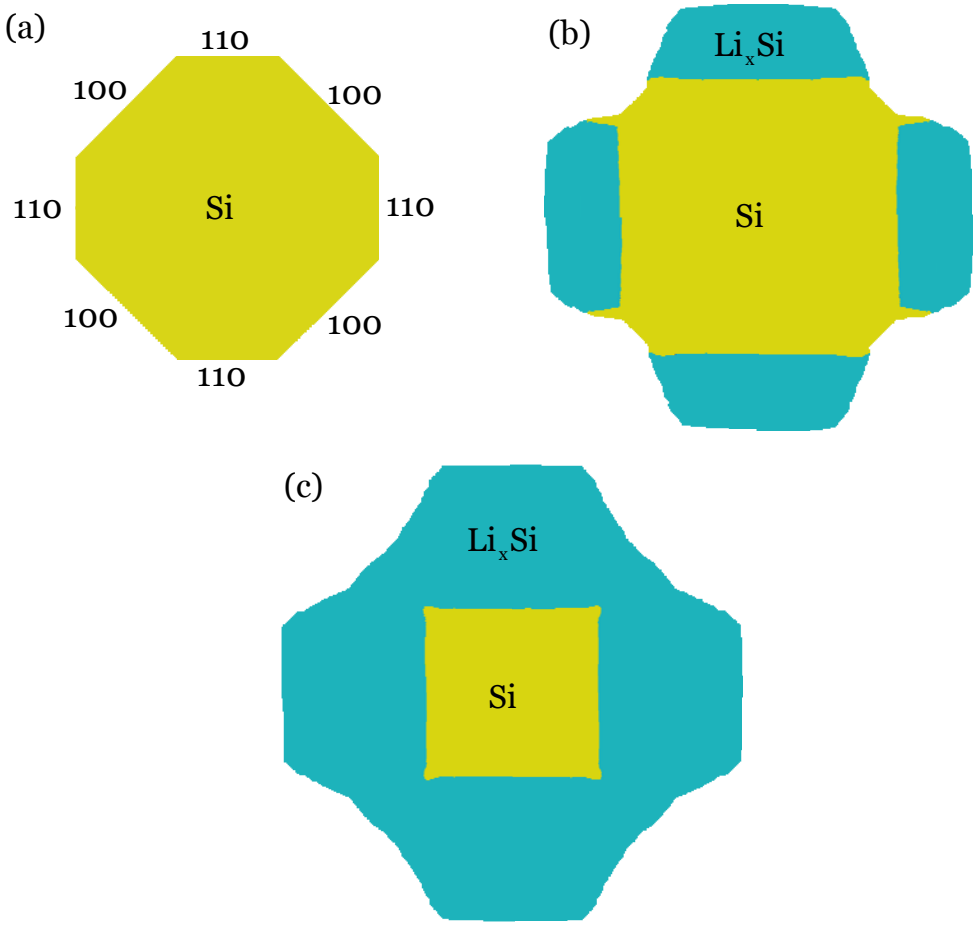

Figure 7. 8. Concurrent migration of the reaction front and plastic deformation in the amorphous phase evolve the anisotropic shape. (a) Schematics of silicon electrode with different crystallographic facets. Lithiation reaction primarily occurs on the <110> planes. The anisotropic shape evolution at the time (b) $t/\tau = 0.25$, and (c) $t/\tau = 0.5$. τ is the time to fully lithiate the crystalline silicon particle.

To accommodate this volumetric expansion, the plastic deformation is updated by solving the boundary-value problem. To avoid computational singularity, the temperature front, which simulates the reaction front, is located within a thin

shell, whose size is much smaller than the feature size of the nanopillar, but sufficiently larger than the mesh size. Such regularization is used to afford a compromise between computational cost and accuracy. Figure 7. 8 (b) and (c) show the morphologies of the particle at two stages of reaction, $t/\tau = 0.25$ and $t/\tau = 0.5$, using the procedure described above. τ is the time to fully lithiate the crystalline silicon particle. The anisotropic pattern agrees well with the experimental observation.[121]

7.6 Summary

Crystalline Si and Li react to form lithiated silicon. The reaction front is at the atomically sharp phase boundary between the crystalline Si and lithiated Si. The reaction generates a large volumetric expansion, which is accommodated by plastic deformation in the lithiated Si. This paper describes a model that co-evolves the reaction front and plastic deformation. The velocity of the reaction front relates to the change in the free energy through a kinetic model, while the stress field evolves according to the elastic-plastic theory. The model is illustrated with the lithiation of a spherical particle of crystalline Si. We show that fracture is averted when the particle is small and the yield strength of lithiated Si is low. The model also accounts for anisotropic morphologies of lithiated Si. It is hoped that model will aid in the planning of future experiments and atomistic simulations.

Chapter 8

Li-assisted plastic deformation: A first-principles study

8.1 Introduction

Mechanical stability is one of the key criteria for the selection of materials for commercial batteries.[5] The electrode material has to maintain its mechanical integrity and chemical properties over a long lifetime. Lithiation-induced fracture not only limits the lifetime of existing commercial batteries, but also acts as a bottleneck for developing high-capacity Li-ion batteries.[6] One way to circumvent the mechanical damage is the use of nanostructures, possibly encapsulated by confining oxide layers, which can mitigate the effects of stress by managing the electrode deformation pattern through its shape and geometric restrictions.[130]-[132]

Recent experiments indicate that the lithiation-induced large deformation of silicon electrodes can be accommodated by plastic flow: during lithiation Si films deform plastically when the stress exceeds yield strength.[52] This feature makes it possible to maintain good capacity over many cycles for silicon anodes of small sizes. For instance, Takamura *et al.* have demonstrated fracture-free lithiation of a 50nm-thick Si film for more than 1,000 cycles.[20] During this cycling, the film develops surface undulations, a type of roughening also observed during cyclic lithiation of Si nanowires.[21] Furthermore, Sethuraman *et al.* measured lithiation-induced stress as a function of the state of charge in an amorphous Si thin

film and found a pronounced hysteresis, indicating plastic deformation of lithiated silicon.[52] These observations motivated studies of Li diffusion coupled to the elastic-plastic deformation of the electrode, using continuum plasticity theory.[61], [90], [133]While the experimental observations and the modeling of silicon lithiation based on continuum theories provide an understanding of the long-range mechanical properties, the atomic-scale mechanisms that give rise to the plastic behavior remain poorly understood.

In this chapter, we employ first-principles computational methods to explore the atomic-scale mechanisms of lithiation and the relation to mechanical behavior. Previous atomistic studies primarily concentrated on elastic properties of the bulk,[50], [134] and on reproducing the volumetric and electric potential responses during lithiation and delithiation.[135], [136]More recently, groups studied the energetics of lithium atoms in bulk crystalline silicon[128], [137]-[139] and in silicon nanowires[140]-[143]. Here we present first-principles studies of the atomistic mechanism of large plastic deformation in lithiated crystalline (c-Si) and amorphous silicon (a-Si). We find that the local atomic structure in a silicon network is altered by Li insertion, with Si atoms breaking a bond and reforming a new bond with different neighbors. In this process, the lithiation-induced weakening of bonds between Si atoms and the high mobility of Li in the network play key roles. The continuous breaking and reforming of Si-Si bonds accommodates the large plastic deformation of lithiated silicon.

8.2 Li in crystalline Si

The first-principles calculations based on Density Functional Theory (DFT) were performed using the SIESTA code.[144] The crystalline structure is modeled as a 2x2x2 supercell of the conventional cubic cell that contains 8 atoms, with periodic boundary conditions. For consistent comparisons, a supercell containing the same number of Si atoms (64) is employed for the amorphous silicon study. This choice of supercell is consciously relatively small, because we are interested in exploring both a large number of possible configurations (especially for the amorphous case) of Si structures with various Li concentrations, and a wide range of perturbations of the equilibrium structures through application of large stresses. Our choice of supercell affords these explorations at a reasonable balance of computational cost and accuracy. The calculated silicon lattice constant is 5.52 Å, slightly larger than the experimental value of 5.43 Å; this difference can be attributed mostly to the generalized gradient approximation for the exchange-correlation functional used in the calculations.[145] The atomic structures, system energy and mechanical stresses are calculated using a local-basis set of double-ζ polarized atomic orbitals with an energy cutoff of 70 Ry (~952 eV). In energy optimization calculations, both the atomic coordinates and the supercell shape were relaxed. The energy optimization was considered complete when the magnitude of the force on each atom was smaller than 0.04 eV $Å^{-1}$.

As our first topic, we investigate the mechanisms through which the presence of Li atoms in the crystalline silicon lattice can lead to the breaking of Si-Si bonds. We begin this investigation by determining the stable positions of a single Li atom in c-Si. A single Li atom was placed into the supercell at different nonequivalent sites, shown

in Figure 1(a), including the tetrahedral site (*Td*), the hexagonal site (*Hx*), the center of a Si-Si bond (*Bc*), the center of the distance between next nearest Si neighbors (*Cn*), and a substitutional site.

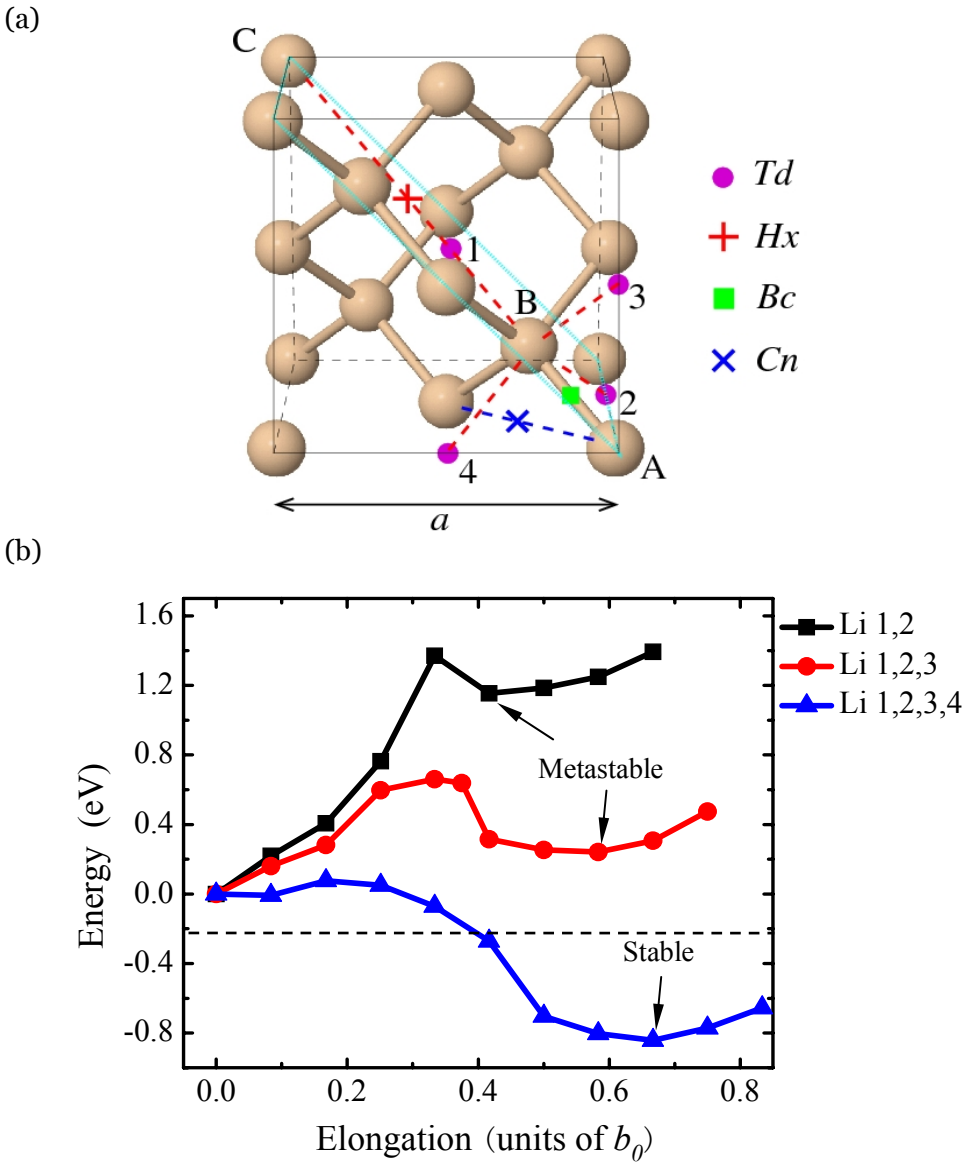

Figure 8. 1. (a) Nonequivalent sites for Li atoms in a c-Si unit cell. The conventional cubic cell of c-Si is outlined by the thin black lines (solid and dashed). The *Td* site is shown as purple circle, the *Hx* site as red cross, the *Bc* site as green square and the *Cn* site as blue X (see text for details). Four equivalent *Td* sites (labeled 1, 2, 3, 4), are shown in relation to the pair of Si atoms labeled A and B. The (110) plane outlined in light-blue lines is used for the display of valence charge densities in Figure 8. 2. (b) The total energy as a function of the AB Si-Si bond elongation for different numbers of Li atoms at the *Td* sites around this bond, in units of b_o = 2.39 Å, the calculated Si-Si equilibrium bond length.

In the calculation of the binding energy, we take the energy of an atom in c-Si (E_{Si})

and the energy of an isolated Li atom (E_{Li}) as the reference energies, with $E_{n\mathrm{Li\text{-}Si}}$ being the total energy of the system containing n Li atoms in the cell which contains 64-m Si atoms (m = 0, except in the case of the substitutional site for the Li impurity, for which m = 1). The binding energy per Li atom $E_b(n)$ is:

$$E_b(n) = [E_{nLi\text{-}Si} - (64 - m)\,E_{Si} - nE_{Li}]/n \qquad (8.1)$$

Table 8. 1 lists the calculated binding energies for Li in the various positions discussed above; these energies include the basis set superposition error (BSSE) correction. The binding energies at different positions indicate that Li insertion into the tetrahedral (*Td*) or hexagonal (*Hx*) positions results in an energetically favorable structure. We note that substitution of Si by Li is energetically costly, and that the bond center is an unstable position for a Li atom, in contrast to the case of hydrogen atoms in a silicon lattice, for which the most stable configuration is the bond-center site.[146] The binding energy of a single Li at a *Td* position is lower in magnitude than the energy of a Si-Si covalent bond of 2.72 eV,[147] which indicates a relatively weak interaction between the Li and Si atoms. The energy difference of 0.55 eV for a Li atom at the *Td* and *Hx* sites is close to the diffusion energy barrier reported by Wan *et al.*[128], as expected, given the known *Td–Hx–Td* diffusion pathway for Li in the c-Si lattice. In Table 8. 2, we show the binding energy as a function of the number of Li atoms in c-Si. With increasing occupancy of *Td* sites by Li atoms, the binding energy per Li atom decreases slightly due to the repulsive local interactions between Li atoms. The change in volume upon insertion of Li atoms in the c-Si lattice is always positive for all the sites considered, and is in the range of a fraction of a percent, with

the largest change occurring for the *Bc* site.

TABLE 8. 1. The calculated binding energies E_b (in eV) and relative volume changes V/V_o for one Li atom at the various sites in c-Si lattice shown in Figure 8. 1 (a). The Li position is given in Cartesian coordinates and in units of the lattice parameter a of bulk c-Si (the calculated value is a = 5.52 Å).

Li site	Position	E_b (eV)	$\Delta V/V_0$ (%)
Substitutional	$(0,0,0)$	1.37	0.3
Center of next nearest neighbors (*Cn*)	$\left(\frac{1}{4},\frac{1}{4},0\right)$	1.39	0.2
Bond center (*Bc*)	$\left(\frac{1}{8},\frac{1}{8},\frac{1}{8}\right)$	1.27	0.8
Hexagonal site (*Hx*)	$\left(\frac{5}{8},\frac{5}{8},\frac{5}{8}\right)$	-0.60	0.4
Tetrahedral site (*Td*)	$\left(\frac{1}{2},\frac{1}{2},\frac{1}{2}\right)$	-1.15	0.2

TABLE 8. 2. The calculated binding energy $E_b(n)$ and relative volume changes V/V_0 as a function of n, the number of Li atoms in the crystalline and amorphous Si structures at *Td* (in c-Si) and *Td*-like (in a-Si) positions; each cell contains 64 Si atoms. f is the concentration of Li atoms in the cell. In the amorphous case, for n =1, the values represent the average of the 32 lowest-energy *Td*-like positions, while the values in square brackets below the averages show the range from the smallest to the largest value in each case.

	Number of Li (n)	$E_b(n)$ (eV)	$\Delta V/V_0$ (%)
Crystalline silicon	1 (f = 0.0156)	-1.15	0.2
	2 (f = 0.0313)	-1.13	0.5
	3 (f = 0.0469)	-1.08	0.9
	4 (f = 0.0625)	-1.03	1.3
Amorphous silicon	1 (f = 0.0156)	-1.57	0.4
		[-1.94, -0.55]	[0.2, 0.7]
	8 (f = 0.125)	-1.84	3.3
	16 (f = 0.25)	-1.79	6.4
	32 (f = 0.5)	-1.92	24

To demonstrate the atomistic mechanism of Li-assisted Si-Si bond breaking, we focus on a particular bond. In the simulations, we displace a Si atom B with respect to a fixed Si atom A, imposing a gradual elongation of the AB bond. For each set of fixed positions of A and B, the other atomic positions and supercell shape are relaxed to provide the system energy at the given AB bond length. The displacement of atom B is along a main diagonal of the conventional cubic cell, shown as the red dashed line in Figure 8. 1 (a), toward the position of the Si atom labeled C. When the bond between atoms A and B is broken, the dangling bonds may be saturated by the neighboring Li atoms. We verify this scenario by examining the energetics of different

configurations with two, three and four Li atoms in the immediate neighborhood of the AB bond. Figure 8. 1 (b) shows the energy profiles as a function of the applied elongation of the AB bond for various Li concentrations (with 2, 3 and 4 Li atoms), relative to the system energy when the Li atoms are placed at *Td* positions and no stretch is applied to bond AB. When 2 or 3 Li atoms occupy *Td* positions, the initial configurations are the most stable structures, and the energy barriers for transforming to a metastable stretched configuration are 1.37 eV and 0.66 eV, respectively. However, when 4 Li atoms are placed at *Td* sites around the AB bond, the stretched structure is stable and the corresponding energy barrier is only 0.08 eV. Thus, when a single Si-Si bond is surrounded by 4 Li atoms the bond readily breaks with a very small energy barrier, and the system reverts to a more stable configuration where one of the Si atoms (B) is displaced to a position close to that occupied originally by the Li atom labeled 1 in Figure 8. 1 (a).

In order to elucidate the bond breaking mechanism induced by lithiation, we plot in Figure 8. 2 (a) the total valence electron charge density distribution on a (110) plane for the stable configuration with 4 Li atoms (this plane is highlighted in Figure 8. 1(a)). Close inspection of this charge density plot shows that the bond between Si atoms A and B is indeed broken, and a weaker bond of mixed covalent-ionic character is formed between the Si atom at position B and the Li atom at position 1. This is consistent with the expectation mentioned above that the Li atoms can saturate the dangling bonds of the Si atoms upon bond breaking; the Si-Li bond is expected to be asymmetric and polar, due to the large difference in electronegativity

between the two elements (0.98 for Li *vs.* 1.90 for Si).

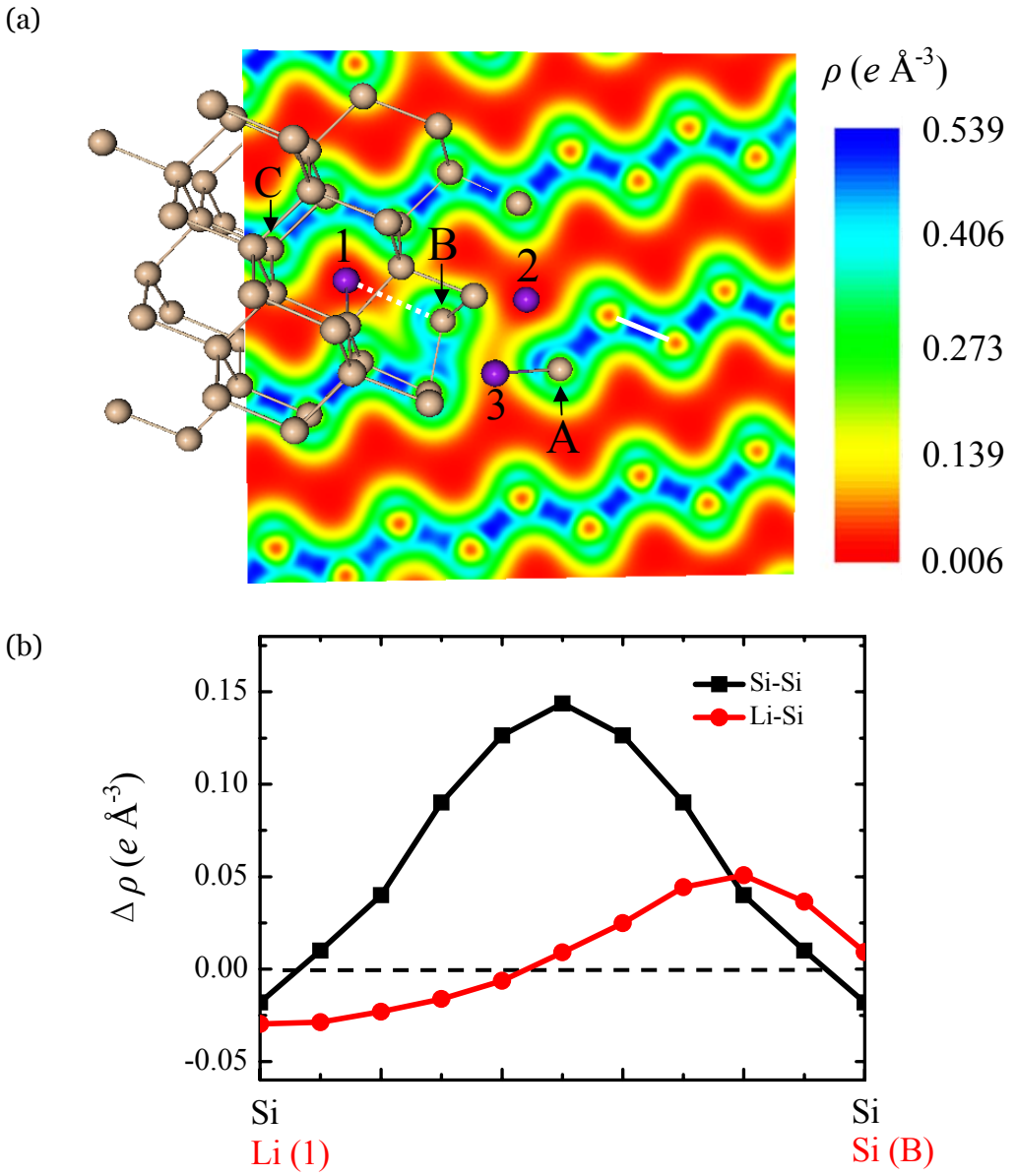

Figure 8. 2. (a)Valence electron charge density distribution on a (110) plane in the lowest-energy configuration of c-Si with 4 Li atoms. The (110) plane is indicated by light-blue lines in Figure 8. 1 (a). (b) The charge density difference distribution along a Si-Si bond in pure c-Si represented by a solid white line in (a), and the Li-Si bond 1-B represented by a dashed white line in (a).

To better illustrate this point, we show in Figure 8. 2 (b) the charge density difference distributions along a Si-Si bond in the pure silicon lattice and along the Li-Si bond 1-B. The charge density difference $\Delta\rho$ is defined as

$$\Delta\rho=\rho_{\mathrm{nLi\text{-}Si}}-\rho_{\mathrm{Si}}-\rho_{\mathrm{Li}} \tag{8.2}$$

where $\rho_{\mathrm{nLi\text{-}Si}}$, ρ_{Si}, ρ_{Li}, represent the electron densities of the Li-Si system containing n Li atoms in the c-Si supercell, the pure silicon structure consisting of only Si atoms in the same positions as in the Li-Si system, and the contribution from the individual Li atoms at the positions they occupy in the Li-Si system, respectively. The electron density around the Li atom is clearly lower than what it would be near a Si atom in the pure Si crystal, whereas the electron density near the Si atom at position B is higher, indicating a partial electron transfer from the Li atom to the neighboring Si atom. In contrast to the purely covalent bonds in c-Si, which involves a very significant and symmetric electron charge accumulation between a pair of Si nearest neighbors (black symbols and line in Figure 8. 2 (b)), the Si and neighboring Li atoms form a weak bond of mixed ionic-covalent character, with significant charge depletion of the Li atom and charge accumulation closer to the Si atom (red symbols and line in Figure 8. 2 (b)), since the latter is more electronegative.

8.3 Li in amorphous Si

During operation of a Li-ion battery, the crystalline silicon electrode is amorphized after the first cycle of charge and discharge.[21] To avoid the stress field induced by this phase transition, amorphous silicon is often used as the electrode in experiments. Intense efforts have been directed toward the characterization of the plastic deformation behavior of silicon during lithiation and delithiation, both experimentally and theoretically,[52], [90], [133] but the deformation mechanism

responsible for plastic flow has not been elucidated so far. In an attempt to capture the essential atomistic aspects of the plastic deformation mechanisms we performed a set of simulations that model a uniaxial tension experiment on lithiated silicon at various Li concentrations. The main insight from these simulations is that the plastic deformation is induced by a continuous, Li-assisted breaking and reforming of silicon bonds.

The a-Si network is generated by quenching the liquid phase with explicit molecular dynamics using the environment dependent interatomic potential (EDIP) for Si.[148] The resulting amorphous 64-atom supercell is completely free of coordination defects. The details describing this amorphous supercell have been reported elsewhere.[149] We take this cell as representative of the ideal, coordination-defect-free continuous random network that is relevant to the a-Si structure, although the actual amorphous solid is expected to contain defects such as under-coordinated (3-fold) or over-coordinated (5-fold) atoms. The bond-length distribution in this model has a peak at 2.37 Å, close to the calculated bond length in c-Si (2.39 Å), and is quite broad, with values ranging from ~2.18 Å to ~2.65 Å.

We focus here on the equilibrium, static features of lithiated silicon and do not consider kinetic effects, such as long-range diffusion processes of Li in the Si structure. We first investigated the stable positions for a single Li atom in the amorphous structure. By analogy to the crystalline case, we considered "*Td*-like" positions for the Li atoms as candidates for the lowest-energy structure. These are positions along the direction of each Si-Si bond, at a distance equal to the Si-Si bond

length from each Si atom and away from its nearest Si neighbor. The 64-atom supercell contains 128 Si-Si bonds and therefore there are 256 such *Td*-like positions in the model. To determine the actual lowest-energy positions, we placed a Li atom in each of these *Td*-like positions and then relaxed the whole structure by allowing rearrangement of atomic coordinates as well as relaxation of the supercell shape. Since some of the *Td*-like positions share the same cage of neighboring Si atoms, the relaxation produced 32 unique configurations that are not necessarily a subset of the initial 256 *Td*-like candidates; the Si coordination of the original amorphous structure is maintained in each relaxed structure. We then vary the Li occupancy of these 32 positions to control the concentration f (ratio of the number of Li atoms over the number of Si atoms) in our uniaxial stress simulations. In structures with less than full Li occupancy, such as $f = 0.125$ and $f = 0.25$, the Li atoms are located at the most energetically favorable sites out of the 32 lowest-energy positions. We note that for all these values of Li concentration the binding energy per Li atom is negative (see Table 8. 2); in other words, it is energetically favorable to insert Li atoms in the amorphous structure, taking as a reference bulk amorphous Si and free Li atoms. Moreover, the values of the binding energy per Li atom in the amorphous case are substantially larger in magnitude than the binding energy per Li atom in the crystalline lattice, suggesting that thermodynamically it is better to insert Li in electrodes consisting of amorphous rather than crystalline Si. Full occupancy of all the *Td*-like sites corresponds to an amorphous structure with $f = 0.50$, well below the theoretical capacity of 4.4 Li atoms per silicon atom. Nevertheless, even at these

relatively low concentrations, we observe pronounced Li-mediated effects on the mechanical behavior of lithiated silicon. This effect has also been observed in experiments.[92]

In the simulation of uniaxial tension, we prescribe a given stress level along the *x*-direction of the structure, and measure the nominal strain after full relaxation. The stress-strain response curves are shown in Figure 8. 3 (a). For each curve, the highest stress level represents the strength of the lithiated structure before it is fractured. The solid symbol curves represent the loading paths, while the open symbol curves represent the unloading paths. It is evident that a brittle-to-ductile transition occurs as the Li concentration increases, with very different behavior for f = 0 and f = 0.125 *vs.* f = 0.25 and f = 0.50. The corresponding strength decreases as well with increasing Li concentration. In the pure silicon structure, loading leads to nonlinear elastic behavior and the unloading path follows the loading path exactly; there is no permanent deformation after unloading. In the case of Li concentration f = 0.125, a small permanent strain of $\varepsilon = 1.21\%$ is observed after unloading. As the Li concentration increases to f = 0.25 and f = 0.50, the stress-strain curves show substantial plastic deformation. The network can be stretched by 33.5% and 40.5%, respectively, without fracture. After unloading, large permanent deformation remains in both cases. Figure 8. 3 (b) shows the average value of Si coordination, $\langle C_{Si} \rangle$, as a function of applied strain. To determine a physically meaningful Si coordination, we define two Si atoms to be bonded if their distance is within 20% of the covalent bond length in bulk c-Si, which corresponds to a largest distance of 2.87 Å. The average

coordination is closely related to the deformation behavior of lithiated silicon. At Li concentrations f = 0 and f = 0.125, the coordination of silicon changes little during deformation, corresponding to brittle behavior at low Li concentration. In contrast, at larger Li concentration f = 0.25 and f = 0.50, the Si coordination decreases dramatically with strain, which is related to the ductile behavior.

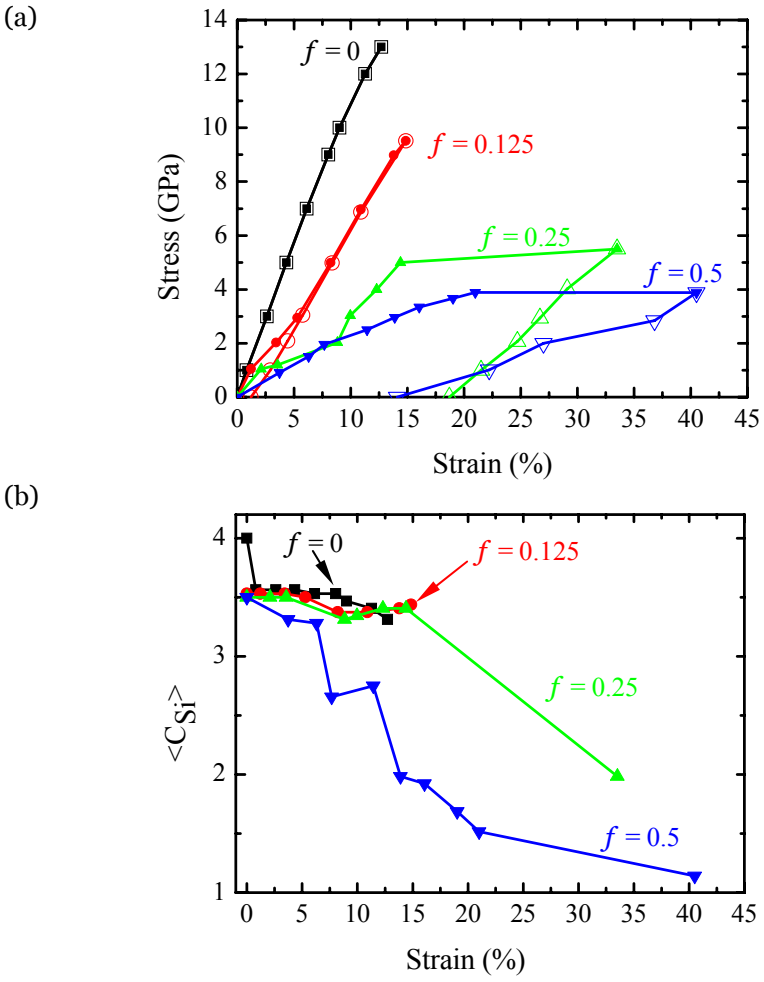

Figure 8. 3. (a) The stress-strain response of lithiated a-Si under uniaxial tension. The solid symbol lines represent the loading path; the open symbol lines represent the unloading path. (b) The average value of Si-Si coordination (<C_{Si}>) as a function of applied strain during loading.

Another indication of the very different nature of the mechanical behavior at elevated Li concentrations in a-Si is given by the volume relaxation (see Table 8. 2).

The volume relaxation is roughly consistent with the corresponding values in c-Si for concentrations up to f = 0.25 (about 0.4% for n =1 and proportionally larger for n = 8 and 16), but is considerably higher for f = 0.5, when the volume increase is twice as large as would have been expected from the proportional relation up to f = 0.25. This is indicative of large changes in the structure, which includes formation of nano-pores that can easily accommodate the presence of several Li atoms and will respond differently than the uniform solid to external stress, consistent with recent experimental observations on Si nanowires.[67]

Figure 8. 4 shows the dependence of Young's modulus on Li concentration. The solid squares represent the average values of the elastic stiffness constants along the *x-, y-* and *z*-directions and the error bars the effect of the anisotropy of the amorphous structure due to the finite size of the model and the non-uniform distribution of Li atoms on the scale of the supercell. The open circles represent Young's modulus of pure c-Si (black symbol) and of the stable configuration of c-Si with 4 Li atoms (orange symbol). Evidently, Young's modulus decreases with increasing Li concentration. The inset in Figure 8. 4 shows the Si coordination for different Li concentrations at zero strain. The softening effect induced by lithiation is correlated with an increase of coordination defects at higher Li concentrations, as evidenced by the increasing fraction of three-fold coordinated Si atoms; this finding is consistent with experimental measurements[92] and other *ab-initio* calculations.[50]

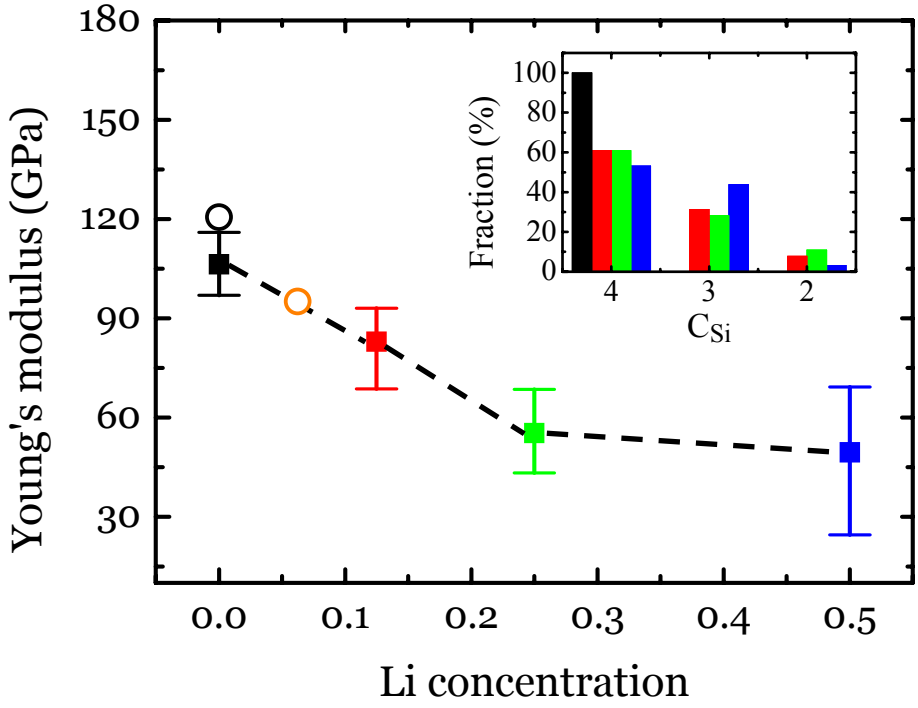

Figure 8. 4. Dependence of the Young's modulus on the concentration of Li. The error bars represent variations due to the anisotropy of the amorphous model structure. The open symbols represent Young's modulus of the pure c-Si lattice (black circle) and of the stable configuration of c-Si with 4 Li atoms (orange circle). The inset shows the distribution of Si coordination (given as percentage of total number of atoms) in a-Si for different Li concentrations at zero strain. The color of each bar in the inset corresponds to the Li concentration of the same color on the large plot.

The large plastic deformation observed in our simulations can be traced to the Li-assisted breaking and reforming of Si-Si bonds. To illustrate this process, we show in Figure 8. 5 four snapshots along the loading path for the case of Li concentration f = 0.50. The snapshots show the atom positions at various loading strains. Two Si atom pairs, labeled D, E and F, G, are shown enlarged for better contrast. The snapshots clearly show the evolution of bonding between these two silicon pairs: silicon atoms D-E experience bonding/non-bonding/bonding changes from the initial state to the final state, while silicon atoms F-G undergo non-bonding/bonding/non-bonding changes during the same deformation.

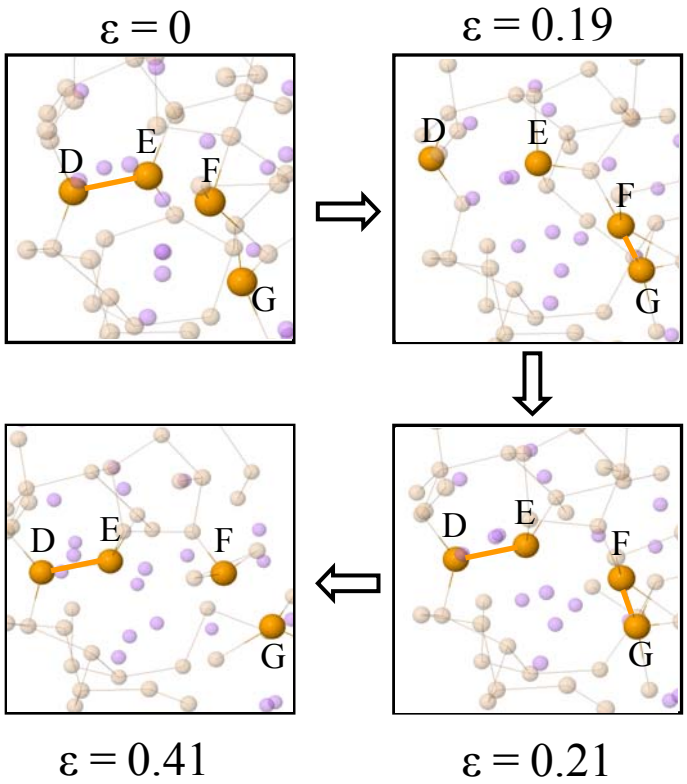

Figure 8. 5. The Si-Si bond breaking and reforming process during deformation of lithiated silicon at Li concentration f = 0.50. The four snapshots correspond to the states of various strain values ε , as indicated. The two Si atom pairs D-E and F-G that undergo bonding/non-bonding/bonding and non-bonding/bonding/non-bonding transitions are enlarged for better contrast.

8.4 Summary

In conclusion, we have studied the effects of Li in both crystalline and amorphous Si, using first-principles calculations based on Density Functional Theory. Our main findings are: first, *Td* interstitial positions are the lowest-energy sites for Li insertion into c-Si, and that when four Li atoms surround a single Si-Si bond the covalent bond readily breaks and the two Si dangling bonds are essentially saturated by the formation of weak bonds of mixed ionic-covalent character with the nearby Li atoms. Also, in a-Si with sufficiently high Li concentration (roughly f = 0.125 or higher) the structure undergoes a brittle-to-ductile transition with significantly lower

Young's modulus, and plastic deformation becomes relatively easy. The essence of these results is that the chemical interactions of lithiation give rise to pronounced effects on the mechanical behavior of silicon structures. In particular, as the stresses induced by lithiation are limited by the yield strength, the fracture failure of the silicon electrode can be largely remediated by taking advantage of the plasticity of lithiated silicon. At the microscopic scale, we have identified and described by specific examples the atomistic mechanism responsible for plastic deformation, which consists of continuous Si-Si bond breaking and reformation in the presence of Li; we suggest that this process may also be responsible for the steady flow at the macroscopic scale.

Chapter 9

Reactive flow in silicon electrodes assisted by the insertion of lithium

9.1 Introduction

In the quest to develop high-energy density Li-ion batteries, materials that can absorb large amounts of Li are of great interest. Silicon shows remarkable ability to absorb Li, making it a very promising anode material.[24] This, however, comes at the cost of very large deformation of the Si structure upon lithiation and a concurrent drastic change in mechanical properties, from the brittle nature of pure crystalline Si to an amorphous material that can undergo plastic flow in the lithiated form. This behavior is typical during the electrochemical cycling of high-capacity electrodes, such as lithium alloy anodes,[24] conversion oxides,[117] and sulfur cathodes,[150] all of which exhibit significant structural transformations and property changes induced by the Li insertion reaction.

The large amount of absorption of Li by Si results in a large volumetric expansion and severe structural changes. The lithiation-induced stress and fracture often lead to the loss of active materials and rapid decay of capacity, which limit its commercialization.[10] This mode of failure can be mitigated by manipulating the structural optimization and deformation patterns of nanostructured Si anodes. Recent experiments and theories show evidence that the large deformation of lithiated silicon can be accommodated by plastic flow, which may avert fracture of

nanostructured silicon.[52], [61], [66] To develop feasible nanostructured anodes, it is crucial to understand the lithiation, deformation, and stresses from a fundamental perspective.

Since the chemical interaction between Li and Si is local, first-principles quantum mechanical calculations can capture the microscopic mechanism of the lithiation reaction. The local chemical effects lead to the macroscopic mechanical behavior, such as plastic flow of lithiated silicon. Lithiation and plastic flow are both nonequilibrium processes. We extend the continuum theory of plasticity and formulate a yield condition by placing driving forces for lithiation and plasticity on the same footing. In-situ experimental measurements of the stress evolution in an a-Si thin film during a lithiation and delithiation cycle serve both as the motivation for the theoretical work as well as a detailed quantitative test of the theory.

Previous atomistic studies include examining the energetics of Li in bulk crystalline silicon and silicon nanowires,[128], [137]-[143] characterizing the elastic properties of the bulk,[50] and reproducing the volumetric and electric potential responses during lithiation and delithiation.[135], [136] First-principles calculations have also been employed to illustrate the deformation mechanism of plasticity in lithiated silicon.[66] Here we present atomistic studies on the concurrent process of Li insertion and plastic deformation of amorphous lithiated silicon. Both the atomic insertion driven by the chemomechanical load and the plasticity driven by the mechanical load contribute to the reactive flow of lithiated silicon. We propose a yield function to describe the plastic behavior. We correlate structural changes at the

atomic scale with the macroscopic response and study the transition of electronic properties of Si upon Li insertion, from the semiconductor state to the metallic state.

9.2 Stress measurement in an a-Si thin film electrode

We begin with a description of the experimental results that motivated this study. The experimental measurements are mainly contributed from my colleague Matt Pharr. We measure the stress evolution in an a-Si thin film electrode during the first lithiation and delithiation cycle by the wafer curvature method. The solid electrolyte interface (SEI) layer could have significant effect on the stress measurement, an effect that might be minimized in the first lithiation cycle. Li insertion and extraction result in a state of biaxial stress in the a-Si thin film deposited on a thick substrate. The thin film exerts forces on the substrate that result in elastic bending of the substrate. The average stress in the film can be deduced from the curvature of the substrate using Stoney's equation.[53] The electrochemical measurements are carried out in a custom three-electrode beaker cell as illustrated in Figure A. 1. In-situ stress measurements are performed with a multi-beam optical sensor (MOSS). We describe the details of fabrication of amorphous silicon thin film electrodes, assembly of electrochemical cells, electrochemical measurements and stress measurements in the experimental section. Similar experimental set-ups have been reported by other groups.[52], [151], [152]

The evolution of the biaxial stress in the a-Si thin film is shown in Figure 9. 1. During the initial lithiation, the compressive stress increases linearly in the first stage,

indicating an elastic response. The stress reaches an elastic limit of ~2GPa for $Li_{0.25}Si$. We note that the elastic limit is higher than that reported in a previous study,[52] which may be due to neglecting the effect of the refractive index difference between the electrolyte and air in the previous study. With further lithiation, plastic flow sets in to accommodate the additional volume expansion. The compressive flow stress decreases, reaching a value of ~1GPa for Li_2Si at the cut-off potential 0.01V vs. Li/Li+. The low lithiation capacity might be due to the fast charging rate (1C) in the experiment. Upon delithiation, the unloading is initially elastic within a narrow range of Li composition. The stress reaches ~1GPa in tension due to the plastic flow of lithiated silicon. The flow stress increases slightly with further delithiation, reaching a value of ~1.5GPa at the cut-off potential 2V. The delithiation capacity is lower than that during lithiation; the irreversible capacity is often attributed to the formation of SEI.[24]

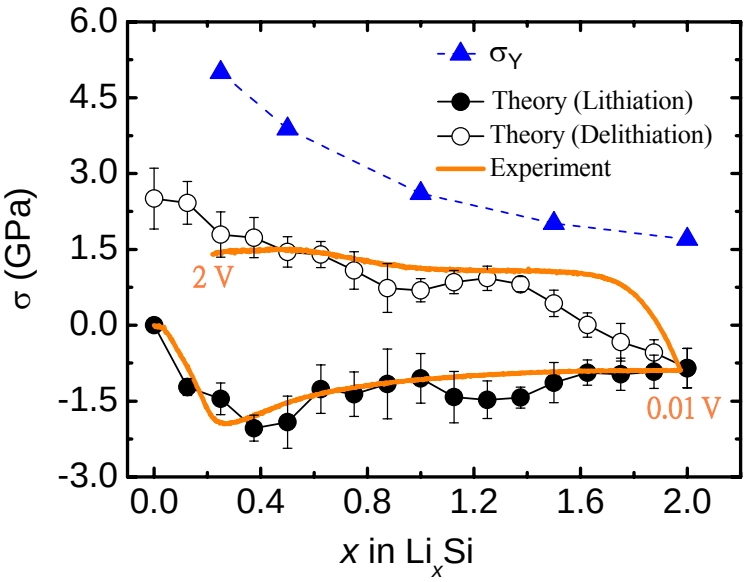

Figure 9. 1. Evolution of the biaxial stress in an a-Si thin film electrode during a lithiation and

Figure 9. 1 (Continued) delithiation cycle: The orange line shows the in-situ measurement of the biaxial stress in the first lithiation cycle by the wafer curvature method. The electrode is cycled at 1C rate between 2 and 0.01V vs. Li/Li+. The black lines with symbols (filled for lithiation, open for delithiation) show the evolution of the biaxial stress in an a-Si thin film electrode during a lithiation and delithiation cycle based on first-principles calculations. The errors bars represent standard deviations obtained from several configurations at each Li concentration. The yield strength of lithiated Si at a given Li concentration, obtained by uniaxial tension simulations, is shown by triangles (the dashed line connecting the triangles is a guide to the eye).

9.3 Stress modeling by first-principles calculations

We simulate the stress evolution in an a-Si thin-film electrode subject to a lithiation and delithiation cycle by employing first-principles computational methods. Such simulations allow a close inspection of the microscopic mechanism of lithiation and the associated deformation behavior. The first-principles calculations based on Density Functional Theory (DFT) were performed using the SIESTA code.[144] The amorphous structure contains 64 Si atoms with periodic boundary conditions. This choice of supercell is consciously relatively small, because we are interested in exploring a large number of possible configurations of Si structures with various Li concentrations. Our choice of supercell affords such studies at a reasonable balance of computational cost and accuracy. The atomic structures, system energy and mechanical stresses are calculated using a local-basis set of double-ς polarized atomic orbitals with an energy cutoff of 70 Ry (~952 eV). In energy optimization calculations, both the atomic coordinates and the supercell shape were fully relaxed. The energy optimization was considered complete when the magnitude of the force on each atom was smaller than 0.04 eV $Å^{-1}$.

The a-Si structure employed here was generated by quenching the liquid

phase with explicit molecular dynamics using the environment dependent interatomic potential (EDIP) for Si,[145] as described in more detail in our previous work.[66] To simulate the behavior of the a-Si thin film bonded to a thick substrate, we constrain the in-plane deformation of the unit cell, with the lithiation-induced volume change accommodated by out-of-plane expansion (*z*-direction) of the unit cell. Kinetic effects, such as the long-range process of Li diffusion in Si, were considered in a separate calculation of the relevant energy barriers. We found that the lowest energy barrier for a single Li atom diffusion in the a-Si network is around 0.4 eV, significantly lower than that in the c-Si lattice (0.55 eV).[66], [128] In the modeling of stress, we assume that diffusion is fast enough to allow for a uniform distribution of Li. A more detailed study of Li diffusion kinetics will be reported elsewhere.

At each Li concentration, we place Li atoms at energetically favorable positions in the a-Si network. To simulate an a-Si thin film, we constrain the deformation in the in-plane directions (*x-, y*-directions), and apply an incremental stretch to *z*-direction with energy minimization at each step of the stretch. The structure resulting from energy minimization corresponds to the zero stress state in the *z*-direction. In order to eliminate the large variations in the calculation of in-plane stresses, we considered five possible configurations of lithiated silicon at a given Li concentration with different distributions of Li in each. We first identified 32 unique lowest-energy positions for a Li atom insertion into the a-Si network. When the Li content is below $Li_{0.5}Si$, we vary the occupancy of the 32 positions to control Li concentration. In structures that have higher Li content than full occupancy of the 32

positions of lowest energy, we examine the number of Li neighbors of each Si atom and place the additional Li atoms around the Si atoms that have the lowest number of Li neighbors. The Li concentration was changed in increments of 8 Li atoms inserted (removed) at each lithiation (delithiation) step.

Due to the constraint in the in-plane directions of the unit cell, a biaxial stress is generated during lithiation and delithiation of the a-Si thin film. The evolution of the biaxial stress obtained from our first-principles calculations is shown in Figure 9. 1. The solid-symbol line represents the stress evolution during lithiation and the open-symbol line represents the stress during delithiation; the symbols represent the average stress of the five configurations considered at each step during lithiation and delithiation while the error bars represent standard deviations. The agreement between the calculations and the experimental measurements is remarkable. In the calculation, during lithiation the biaxial compressive stress reaches an elastic limit of ~2GPa at $Li_{0.375}Si$. With further lithiation, lithiated silicon exhibits plastic flow. The compressive flow stress decreases from ~2GPa to ~1GPa when the Li composition increases to Li_2Si. Upon delithiation, lithiated silicon first unloads elastically, over a wider range of Li composition compared with the experiment. The discrepancy in the elastic unloading might be due to the creation of nano-pores, or to artificial limitations introduced by the relatively small size of our model system. Nevertheless, the agreement in the elastic unloading behavior between experimental measurements and theoretical predictions is still reasonable, if not as satisfactory as in the initial lithiation range. Following the elastic response, the biaxial stress reaches a value of

~1GPa in tension, and the magnitude of the stress steadily increases with further delithiation. The high stress level at low Li concentrations might be due to an elastic response; at sufficiently low Li concentrations, the structure is too brittle to flow.[66]

We first address the question of whether or not the stress generated during the lithiation cycle is equal to the yield strength of the structure. We determine the yield strength of lithiated silicon for various Li concentrations through simulations of uniaxial tension. For each Li concentration, we first perform energy minimization of the lithiated silicon without any constraint. A given stress level is then prescribed along the x direction of the structure, and the nominal strain after full relaxation is measured. The stress-strain response curves are shown in Figure A. 2. More details of the simulation are described in our previous work.[66] The yield strength obtained through this procedure is shown Figure 9. 1; the magnitude of yield strength at a fixed Li concentration is about *twice* as high as the stress generated during the lithiation cycle. The difference between the yield strength and the biaxial stress is attributed to lithiation-assisted plastic deformation: the lithiation reaction enhances plasticity of lithiated silicon by lowering the stress needed to induce plastic flow.

In order to account for these effects, we consider the following model: when an element of a Si electrode is connected to a reservoir of Li with chemical potential μ, it absorbs a number of Li ions and deforms, Figure 9. 2(a). The material element deforms by two mechanisms: elastic and inelastic. Elastic deformation involves small changes of the relative positions of atoms but does not change the identity of neighboring atoms or the concentration of Li. Inelastic deformation involves mixing

and rearranging atoms. The elastic deformation, typically less than 10%, is negligible compared with the large lithiation-induced strain in Si, and therefore the volumetric expansion during lithiation is mainly accommodated by inelastic deformation.

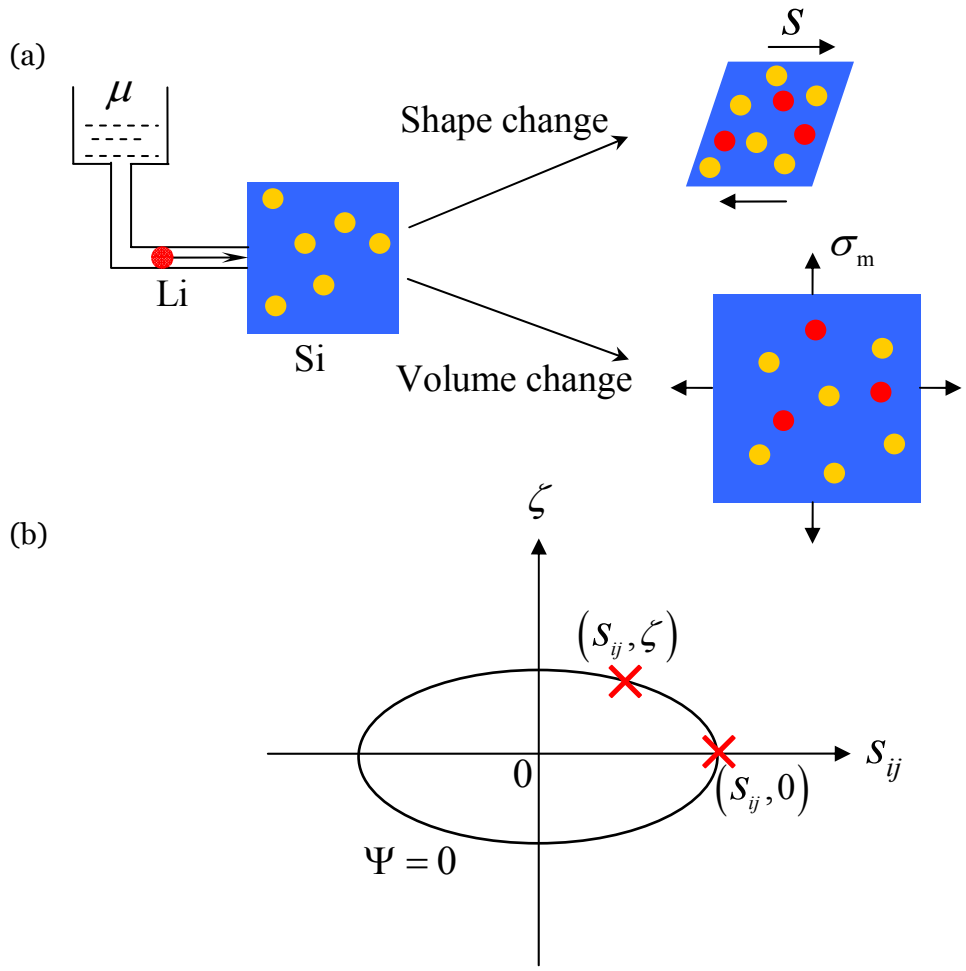

Figure 9. 2. (a) The two types of inelastic deformation of Si during lithiation — change of shape by plastic flow, and change of volume by insertion of Li. Plastic flow is induced by the presence of deviatoric stresses. Insertion is driven by the chemical potential μ of Li in the reservoir and the mean stress σ_{m}. (b) A yield function $\Psi\left(s_{ij},\zeta\right)$ is sketched in the space of $\left(s_{ij},\zeta\right)$; the condition $\Psi=0$ defines the yield surface. $\left(s_{ij},\zeta\right)$ represents the inelastic deformation driven by both the mechanical load s_{ij} and the chemomechanical load ζ, as modeled in the thin film a-Si during lithiation cycle; $\left(s_{ij},0\right)$ represents the inelastic deformation due only to the mechanical load s_{ij}, as modeled in the uniaxial tension simulation.

Here we focus on the inelastic deformation induced by a cycle of lithiation and delithiation. We distinguish two mechanisms of inelasticity of lithiated silicon – shape change by plastic flow and volumetric change by insertion reaction of Li, as shown schematically in Figure 9. 2(a). Under the constraints mentioned, a field of stress is induced in the electrode upon lithiation. Plastic flow is caused by the presence of deviatoric stresses. The plastic flow characterizes the shape change, but conserves the volume of the electrode. This picture is reminiscent of shear flow of a metal or a liquid of small molecules. Insertion of Li induces a volume change in Si. This process is driven both by the chemical potential of Li as determined by the reservoir of Li atoms and by the mean stress generated during Li insertion; this load is referred to as the chemomechanical load. The insertion reaction and plastic flow are concurrent during lithiation. We call this concurrent process "reactive flow". Reactive flow of solids is commonly observed in many other systems, such as oxidation of aluminum and concrete structures with alkali-silica reactions.[153], [154] A full theory of reactive flow of solids is described elsewhere.[155]

Let σ_{ij} be the stress applied to the silicon electrode, $\sigma_m = (\sigma_{11} + \sigma_{22} + \sigma_{33})/3$ the mean stress, and $s_{ij} = \sigma_{ij} - \sigma_m \delta_{ij}$ the deviatoric stress, where δ_{ij} is the Kronecker delta. The chemical potential of Li in the Si electrode is $\mu_0 + kT \ln a - \Omega \sigma_m$, where μ_0 is the chemical potential of Li in the reference state, k the Boltzmann constant, T the absolute temperature, a the activity of Li in the silicon electrode, and Ω the partial molar volume of Li in Si. A compressive mean stress retards Li insertion, and a tensile stress promotes Li insertion. When Li in

the reservoir and Li in the Si electrode are not in equilibrium, the chemical potential is unbalanced. Let μ be the chemical potential of Li in the reservoir. The difference in the chemical potential between Li in the reservoir and that in the silicon electrode defines the driving force for reaction. We write the driving force in the form

$$\zeta = \frac{\mu - \mu_0 - kT \ln a}{\Omega} + \sigma_m . \tag{9.1}$$

When $\zeta > 0$, the imbalance in the chemical potential promotes lithiation. When $\zeta < 0$, the imbalance in the chemical potential promotes delithiation. When $\zeta = 0$, the reaction reaches equilibrium.

We now regard both the reaction and flow as nonequilibrium thermodynamic processes. The driving force for reaction is ζ and the driving force for flow is s_{ij}. Associated with ζ is the work-conjugate variable $\Omega \delta C$, which represents the volumetric response of Si upon lithiation. Associated with s_{ij} is the work-conjugate variable $\delta \varepsilon_{ij}^{p}$, which represents the incremental plastic strain. We formulate the yield condition by placing the driving forces for reaction and flow on the same footing. Let the chemomechanical yield function be $\Psi(\mathbf{s}, \zeta)$. The condition $\Psi(\mathbf{s}, \zeta) = 0$ defines the yield surface in the linear space spanned by s_{ij} and ζ. As an example, we extend the formulation of von Mises to describe reactive flow by adopting a particular form of the chemomechanical yield function:

$$\Psi = \frac{3}{2} s_{ij} s_{ij} + q\zeta^2 - \sigma_Y^2 , \tag{9.2}$$

where σ_Y is the yield strength of lithiated silicon under uniaxial tension condition. In general, σ_Y varies with the Li concentration and the inelastic strains, while q is a dimensionless positive constant that indicates the relative contributions of the

chemomechanical stress and the deviatoric stress to the scalar measure of the driving force for reactive flow. The value of q can be determined through a free swelling experiment, under which reactive flow due to the deviatoric stress is eliminated.

The yield surface Ψ is shown schematically in Figure 9. 2(b), represented by an ellipse in the plane spanned by (s_{ij}, ζ). We mark two important locations on the yield surface by crosses. The first point $(s_{ij}, 0)$, on the horizontal axis, represents the case of reactive flow of lithiated silicon being driven only by the mechanical force, as modeled in the uniaxial tension simulation. Under uniaxial tension, we have $s_{11} = \frac{2}{3}\sigma_Y$, $s_{22} = s_{33} = -\frac{1}{3}\sigma_Y$, and the value of the yield strength of lithiated silicon σ_Y as a function of Li concentration, is taken from the results shown in Figure 9. 1. The second point (s_{ij}, ζ) represents inelastic deformation of lithiated silicon driven by both the mechanical load s_{ij} and the chemomechanical load ζ. This situation is modeled in a thin film a-Si electrode subject to a lithiation cycle, shown in Figure 9. 1. A biaxial stress is induced by Li insertion into a-Si thin film; under plastic flow, $\sigma_{11} = \sigma_{22} = \tilde{\sigma}_Y$, such that $s_{11} = s_{22} = \frac{1}{3}\tilde{\sigma}_Y$, $s_{33} = -\frac{2}{3}\tilde{\sigma}_Y$. Here we differentiate between the yield strength of lithiated silicon under uniaxial tension σ_Y and the flow stress $\tilde{\sigma}_Y$ under the lithiation reaction. Their values are different, as previously mentioned (they are represented by the triangles and circles, respectively, in Figure 9. 1). The chemomechanical driving force ζ of Eq. (9. 1) can be calculated once the chemical potential of Li in the reservoir μ and the activity coefficient a are given. If we neglect the entropy contribution to the chemical potential of Li in the first-principles simulations, $\Omega\zeta$ might be represented by $-E_f$, the formation energy being defined

as $E_f = E_{\mathrm{Li}_x\mathrm{Si}} - E_{\mathrm{Si}} - xE_{\mathrm{Li}}$, where $E_{\mathrm{Li}_x\mathrm{Si}}$ represents the free energy of $\mathrm{Li}_x\mathrm{Si}$, E_{Si} the free energy of the a-Si structure at the reference state, and E_{Li} the free energy of Li atoms in the bulk Li metal, taken to be the natural reservoir for Li. The particular value that ζ may assume does not affect our main findings. The important insight from this analysis, as depicted in Figure 9. 1 and Figure 9. 2, is that the chemomechanical driving force can lower the stress needed for plastic flow. That is, during concurrent Li insertion and plastic deformation, the lithiation reaction promotes plastic flow.

9.4 Structural characterizations in atomistic simulations

The findings discussed so far concern the overall behavior of the system. In order to elucidate the origin of this behavior, we examine the atomic structures involved in the changes of mechanical behavior of Si during a lithiation cycle. We begin with the evolution of volumetric strain, shown in Figure 9. 3(a). During lithiation, Si expands relatively slowly in the first stage. A large volume change takes place starting at $\mathrm{Li}_{0.375}\mathrm{Si}$, with the slope of the volumetric strain remaining almost constant beyond this point. At low Li concentration, Li insertion is mainly accommodated by the insertion into interstitial sites in the a-Si network. The presence of Li does not alter the Si network significantly. Therefore, the Li insertion-induced volume change is relatively small, and the biaxial stress response is linear in the elastic regime. With further lithiation, Li insertion is accommodated by gradually rearranging the a-Si structure through Si-Si bond breaking. Li atoms have a high mobility in the a-Si network that makes it possible to induce Si-Si bond breaking and re-formation, which

in turn allows the system to accommodate plastic flow of lithiated silicon, without further increase of the stress level. At the completion of a lithiation cycle, an irreversible volumetric strain of 8% is induced. We attribute this structural change to the creation of nano-pores. The volume change might reach a steady state after a few cycles.[136] Figure 9. 3(b) shows the evolution of Si-Si and Si-Li bond lengths that accompany these changes in volume. To define atomic bonds, a physically meaningful measure of atomic coordination is needed. We define two Si atoms to be bonded if their distance is within 10% of the covalent bond length in bulk c-Si, which corresponds to a largest bond distance 2.63 Å. We also define a Si atom to be bonded with a Li atom if their distance is smaller than 3.05 Å, a value determined by examining the distribution of Si-Li pairs in the a-Si network with the Li occupancy corresponding to the 32 unique lowest energy positions for Li atoms. In Figure 9. 3(b) we show the average values of the Si-Si bond length $\langle b_{\text{Si-Si}} \rangle$ and the Si-Li bond length $\langle b_{\text{Si-Li}} \rangle$. Both types of bonds remain almost constant during the lithiation cycle, with the average Si-Si bond length at ~2.45 Å and the average Si-Li bond length at ~2.78 Å. The average values of Si-Si coordination $\langle C_{\text{Si-Si}} \rangle$ and Si-Li coordination $\langle C_{\text{Si-Li}} \rangle$ as a function of Li composition are shown in Figure 9. 3(c). The atomic coordination is indicative of the deformation behavior of lithiated silicon. At low Li concentration, the Si-Si coordination changes slowly, corresponding to the elastic behavior. After $Li_{0.375}Si$, both the Si-Si coordination and the Si-Li coordination change linearly, which indicates a constant rate of Si-Si bond breaking and Si-Li bond formation. After a complete cycle of Li insertion and extraction, a fraction of Si-Si

bonds, around 10%, are not recovered, representing the structural damage to the a-Si network induced by the lithiation cycle.

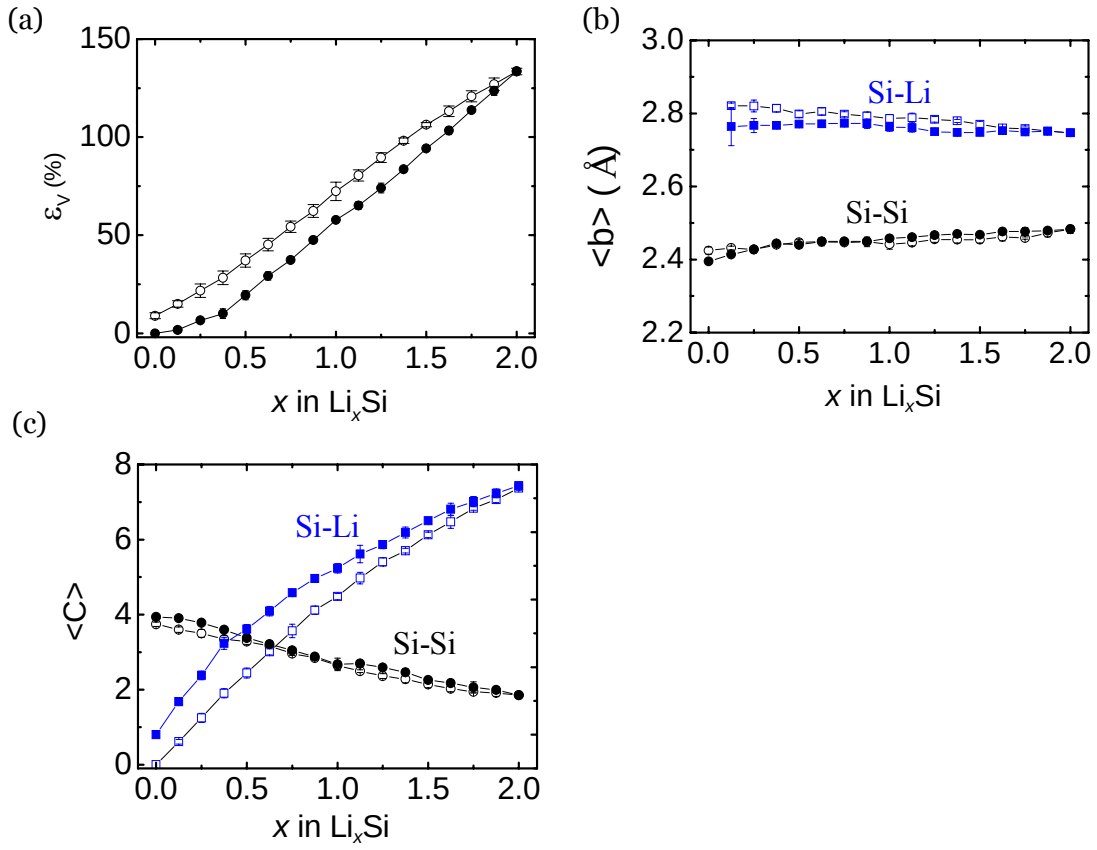

Figure 9. 3. Structural features of an a-Si thin film during lithiation and delithiation cycle: (a) the volumetric strain, (b) the average values of Si-Si bond length and Si-Li bond length, (c) the average values of Si-Si coordination and Si-Li coordination. Solid symbol lines represent paths during lithiation, and open symbol lines represent paths during delithiation. The error bars represent standard deviations obtained from several structures at each Li concentration.

To illustrate the structural change mentioned so far, we show in Figure 9. 4 three representative atomic structures at Li concentrations of x = 0.125 (Li_8Si_{64}), 1.0 ($Li_{64}Si_{64}$), and 2.0 ($Li_{128}Si_{64}$). In the first, with $\langle C_{\text{Si-Si}} \rangle \approx 4$, the small amount of Li present in the structure leaves the network of Si-Si bonds essentially undisturbed; in the second, with Li:Si ratio equal to 1:1 and $\langle C_{\text{Si-Si}} \rangle \approx 3$, the network of Si-Si bonds has been significantly altered, but a fairly well defined network of such bonds still exists and spans the size of the cell; in the third, with the Li:Si ratio equal to 2:1 $\langle C_{\text{Si-Si}} \rangle \approx 2$,

the Si-Si network has been essentially destroyed and only small pockets of Si-Si bonds remain in the structure.[139]

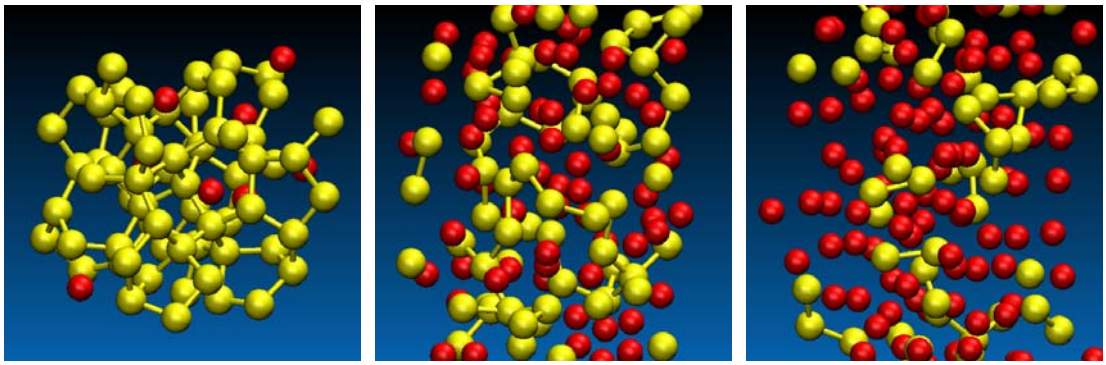

Figure 9. 4. Examples of atomic-scale structure at different Li concentrations: x = 0.125 (Li_8Si_{64}, left panel), 1.0 ($Li_{64}Si_{64}$, central panel), and 2.0 ($Li_{128}Si_{64}$, right panel). Yellow spheres represent Si atoms and red spheres represent Li atoms.

Another indication of the changes to the structure upon lithiation is the overall character of the electronic properties. By analogy to studies of the crystalline-to-amorphous phase transition that occurs with the electrochemical insertion of Li into c-Si,[128] an improved understanding of the semiconducting-to-metallic phase transition of a-Si upon lithiation can help relate the structural properties of a-Si anodes to (macroscopically) measured electrochemical performance. In Figure 9. 5 we show the density of states (DOS) of lithiated a-Si for a representative structure at four different concentrations of Li, x = 0.125 (Li_8Si_{64}), 0.25 ($Li_{16}Si_{64}$), 0.375 ($Li_{24}Si_{64}$), and 0.5 ($Li_{32}Si_{64}$). The corresponding DOS of the pure a-Si structure, which has semiconducting character with a clear gap between occupied and unoccupied states, is superimposed on each of the lithiated structures. A clear trend can be observed in these results: as the concentration of Li increases, a transition from the semiconducting to metallic phase occurs; this observation does not depend on the structure at a particular Li concentration. The

main features of the transition include: (i) electronic states are introduced in and around the band gap region as the band tails of a-Si broaden, a signature of bonding disorder; (ii) electronic states with energy around 2 eV below the Fermi level are depleted, which also reflects bonding distortion, since this is the energy range that characterizes Si covalent bonds; (iii) electronic states are introduced in the energy range between -5 eV and -2 eV that correspond predominantly to *sp*-states of Li. Similar observations have been reported in the work of Wan *et al.* [128]on the lithiation of c-Si. The semiconducting-to-metallic phase transition of a-Si during lithiation is closely correlated with the brittle-to-ductile transition behavior observed in this material.

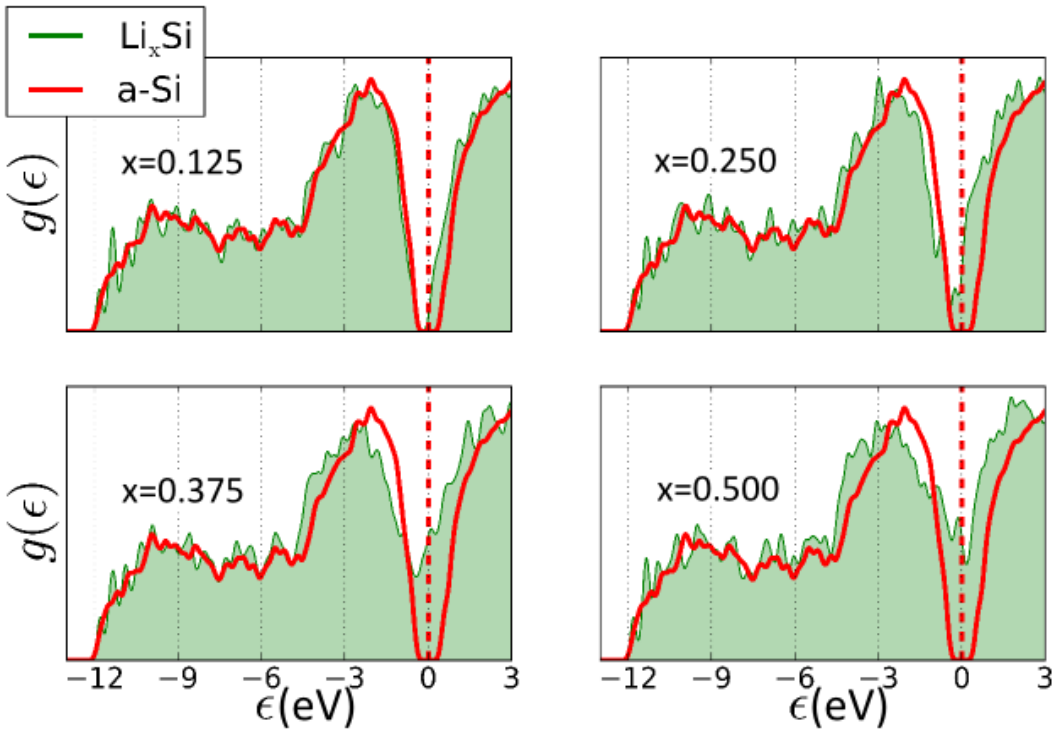

Figure 9. 5. Density of states of pure a-Si (red solid line) and lithiated silicon (green) at Li concentrations of x = 0.125 (Li8Si64), 0.25 (Li16Si64), 0.375 (Li24Si64), and 0.5 (Li32Si64). The vertical dashed line marks the middle of the band gap or Fermi level of pure a-Si, defined as the zero of the energy scale.

9.5 Summary

We have studied the microscopic mechanism of plastic deformation of a-Si electrodes and stresses accompanying the lithiation reaction, using first-principles calculations based on Density Functional Theory. We described the concurrent process of the Li insertion reaction and plastic flow of lithiated silicon. We note that reactive flow of solids is observed in many other physical systems but its theoretical treatment is largely undeveloped. Lithiation of silicon provides a useful model system to study the interplay of local chemical reactions and macroscopic mechanical deformation. The essence of the results in this paper is that the chemical reaction promotes plastic deformation, enabling a material to flow at a lower level of stress. We proposed a phenomenological model to describe the reactive flow of lithiated silicon and examined in detail the local atomic structures and electronic properties to elucidate the origin of the macroscopic mechanical behavior. The agreement between our theoretical treatment and experimental measurement is quite remarkable, despite the limitations of the atomistic model which come chiefly from the size of the periodic supercell to model a-Si.

9.6 Experimental section

The Si thin-film electrode is prepared using a DC magnetron sputtering system (AJA International). A 50 nm Ti thin film was first sputtered for 5 minutes from a Ti target (50.8 mm diameter) onto a 175 μm thick glass substrate at 100 W power and at a pressure of 3 mTorr of Argon. A 300 nm copper film was then

deposited for 15 minutes from a Cu target (50.8 mm diameter) on the Ti underlayer at 200 W power and at a pressure of 5 mTorr of Argon. The Cu film serves as the current collector, and the Ti underlayer is used to improve the adhesion between the Cu film and the glass substrate. A 100 nm Si film was subsequently deposited for 33 minutes from a Si target (50.8 mm diameter) at 100 W power and at a pressure of 5 mTorr of Argon. All depositions were performed at room temperature. After deposition, x-ray diffraction was used to verify the amorphous structure of the Si thin film.

The Si thin film electrode was assembled in a custom three electrodes electrochemical cell (Figure A. 1) with pure Li as reference and counter electrodes. 1M $LiPF_6$ in 1:1 (vol %) ethylene carbonate:diethyl carbonate was used as the electrolyte. Electrochemical measurements were performed with a VersaSTAT 3 galvanostat from Princeton Applied Research. The cell was cycled galvanostatically at a rate of 1C between 2 and 0.01 V *vs.* Li/Li^+. The data acquisition rate was 1 Hz for all electrochemical measurements. The lower limit of 0.01V was chosen to avoid formation of the crystalline $Li_{15}Si_4$ phase.

Stress in the silicon thin film electrode was measured by monitoring the substrate curvature during the electrochemical lithiation cycle. The average stress in the film can be deduced from the curvature of the substrate using Stoney's equation

$$\sigma = \frac{M_s h_s^2}{6 h_f} \kappa, \tag{9.3}$$

where σ is the average stress in the film, h_s and h_f are the thicknesses of the substrate and film respectively, κ is the change in curvature of the substrate as a

result of the stress, and M_s is the biaxial elastic modulus of the substrate. Note that knowledge of film properties other than film thickness is not required to calculate stresses using Stoney's equation. The film thickness h_f is taken as a function of the charge state $h_f = h_f^0\ (1+2.7m)$, where m is the state of charge and h_f^0 is the initial film thickness. This expression takes into account 370% volumetric expansion of Si upon full lithiation. Because of the constraints in the in-plane directions by the thick substrate, lithiation-induced deformation in Si is entirely accommodated by out-of-plane expansion. The curvature of the substrate was monitored with a multi-beam optical sensor (MOSS) from k-Space Associates (Figure A. 1). The MOSS sensor employs an array of parallel laser beams to measure the curvature of a substrate. The array of laser beams allows simultaneous multi-point illumination and detection, which in turn greatly reduces measurement noise caused by fluid motion in the electrochemical cell or by ambient vibrations. The curvature of a substrate is calculated from a geometric relation

$$\kappa = \frac{d - d_0}{2 d_0 L} \frac{n_e}{n_a}, \tag{9.4}$$

where d is the distance between two adjacent laser spots on the CCD camera, d_0 is the initial distance between the laser spots, and L is the distance between the beaker cell and the CCD camera. Since the laser passes through the electrolyte and an optical window, refraction of the laser beams must be taken into account. In Eq. (9. 4), n_e represents the refraction index of the electrolyte, and n_a represents the refraction index of air. In the stress calculations, we take $n_e = 1.42$ for the electrolyte[156] and $n_a = 1.0$ for air.

Chapter 10

Conclusions and outlook

10.1 Summary and concluding remarks

This thesis studies the deformation mechanism, stress and fracture of solid electrodes along with the lithiation reaction in Li-ion batteries. We consider both elastic and inelastic hosts of lithium. In particular, in high-capacity Li-ion batteries, the lithiation-induced deformation is mainly accommodated by the inelastic deformation. We formulate a theory that couples diffusion and large elastic-plastic deformation based on continuum theory. The effect of mechanics on the chemical reaction is one of our focuses in the discussions. We apply the developed theory into two promising anode structures, and analyze the features of the stress field and fracture during the lithiation and delithiation cycle. In addition, during lithiation of crystalline silicon, we recognize that the local reaction between Li and Si is the rate-limiting step, rather than the diffusion of Li through the amorphous phase. Such mechanism brings novel features of the mechanical behavior of lithiated silicon, and can well capture intriguing observations of anisotropic morphologies in recent experiments. Furthermore, we employ first-principles computational methods to explore the microscopic lithiation mechanism and the associated deformation behaviors in silicon. These simulations allow us to better understand the atomistic mechanisms underlying the macroscopic behaviors. Here I briefly summarize the main conclusions in the previous chapters.

- We study fracture of elastic electrodes, $LiCoO_2$ as an example, using a combination of diffusion kinetics and fracture mechanics. A "fracture map" is outlined to show how material properties, electrode particle size, and charging rate affect fracture of electrodes in Li-ion batteries. We predict the critical rate of charging and size of the particle, below which fracture is averted.
- We model an inelastic host of Li by considering diffusion, elastic-plastic deformation, and fracture based on continuum theory of finite deformation. We explore the effect of plastic yielding, stress on the lithiation reaction, and charging rates. It is shown that fracture is averted for a small and soft host—an inelastic host of a small feature size and low yield strength. We apply this theorem into two promising nanostructured Si anodes. Possible failures caused by fracture and debonding are discussed.
- We develop a model of concurrent reaction and plasticity during lithiation of crystalline silicon. We identify the driving force for the movement of the reaction front, and accommodate the reaction-induced volumetric expansion by plastic deformation of the lithiated silicon. We derive the conditions under which the lithiation-induced stress stalls the reaction. The model also accounts for observed lithiated silicon of anisotropic morphologies.
- We further explore the microscopic deformation mechanism of

lithiated silicon based on first-principles calculations. Li insertion leads to breaking of Si-Si bonds and formation of weaker bonds between neighboring Si and Li atoms, which results in a decrease in Young's modulus, a reduction in strength, and a brittle-to-ductile transition with increasing Li concentration. The large plastic deformation is attributed to continuous Li-assisted breaking and reforming of Si-Si bonds. In addition, we model the reactive flow of amorphous silicon during lithiation cycle. We show that the lithiation reaction promotes plastic deformation of lithiated silicon by lowering the stress needed to flow.

10.2 Outlook of future work

Li-ion battery is an emerging filed that is full of challenges and opportunities. A comprehensive understanding of the concurrent chemical and mechanical processes is necessary for development of future high-density batteries. In terms of basic research, high-capacity electrodes particularly provide excellent models to explore the interplay between mechanics and electrochemistry. Interdisciplinary research does not only help to improve the performance of Li-ion batteries, it also provides important insight into the generic interactions between the guest species and host materials.

Beyond the work in this thesis, the following questions remain interesting to explore in future work.

- Fatigue caused by cyclic lithiation is a significant failure mechanism of electrodes in commercial Li-ion batteries. This mode of failure has been recognized decades ago.[18], [157] However, very little work attempts to characterize the fatigue behavior of electrodes so far. The experimental measurement of mechanical fatigue remains challenging because of the complex effects of electrochemical reactions. From the theoretical perspective, we have developed a theory that describes cyclic plasticity of electrodes; it would be interesting to clarify how much lithiation-induced plasticity contributes to the fatigue in the cyclic life of electrodes.
- Although a large volume of mechanical modeling has been reported, a systematic measurement of the mechanical properties of electrodes is lacking. Basic parameters, such as the fracture energy, yield strength, and viscosity, especially as a function of state of charge, are needed to make predictions of practical systems.
- Reactive flow of solids is a common phenomenon in nature, examples mentioned in Ref. [155]. Theoretical framework that describes this phenomenon, however, is largely undeveloped. Reactive flow of lithiated silicon gives a good example. Also the atomistic modeling based on first-principles methods seems to provide a unique way to examine the concurrent process of chemical reaction and plasticity. It would be interesting to quantify the yield function, as sketched in

Figure 9. 2, by first-principles calculations. Furthermore, these calculations can be extended to other systems, such as the reactive flow during oxidation of aluminum.

- It would be interesting to study lithium insertion into other alloy anodes, such as Sn, Ag, Al, etc. One interesting observation is that the partial molar volume of Li in various lithium alloys remains almost constant.[108] This apparently involves local interactions between Li and host atoms, while the atomic structure of host materials seems not significant on the lithiation-induced expansion. A quantitative understanding of such behavior is worth studying.
- The overall capacity of Li-ion batteries is often limited by the cathode. High-capacity cathode materials, such as sulfur, have attracted intensive interest in recent years. For sulfur, the capacity fade is mainly attributed to the dissolution of intermediate lithium polysulfide products in the electrolyte, and large volume expansion (~80%) during cycling.[158] The volume expansion of sulfur upon lithiation is accommodated by the structural reconstruction (i.e., inelastic deformation) from molecular chain like structure (sulfur) to ionic crystal (Li_2S). Such structural transformations at atomistic level, and associated mechanical behaviors, are poorly understood.
- Recently, sodium-ion battery shows promise as a potential alternative to the current lithium-ion batteries.[159], [160] Sodium is one of the most

abundant elements on earth and exhibits similar chemistry of lithium. The knowledge we have of Li-ion batteries might be applied to study interesting behaviors of Na-ion batteries.

Bibliography

[1] Department of energy. Basic Research Needs to Assure a Secure Energy Future 2003.

[2] Department of Energy. Basic Research Needs for Electrical Energy Storage 2007.

[3] Winter M, Brodd RJ. What are batteries, fuel cells, and supercapacitors? Chemical Reviews 2004; 104: 4245.

[4] Tarascon JM, Armand M. Issues and challenges facing rechargeable lithium batteries. Nature 2001; 414: 359.

[5] Armand M, Tarascon JM. Building better batteries. Nature 2008; 451: 652.

[6] Whittingham MS. Materials challenges facing electrical energy storage. Mrs Bulletin 2008; 33: 411.

[7] Tollefson J. CHARGING UP THE FUTURE. Nature 2008; 456: 436.

[8] Huggins RA. Advanced Batteries - Materials Science Aspects, Springer, 2009

[9] Linden D, Reddy TB. Handbook of Batteries, 3rd Edition, McGraw-Hill Inc., 2002

[10] Huggins RA, Nix WD. Decrepitation model for capacity loss during cycling of alloys in rechargeable electrochemical systems. Ionics 2000; 6: 57.

[11] Aifantis KE, Hackney SA, Dempsey JP. Design criteria for nanostructured Li-ion batteries. Journal of Power Sources 2007; 165: 874.

[12] Christensen J, Newman J. Stress generation and fracture in lithium insertion

materials. Journal of Solid State Electrochemistry 2006; 10: 293.

[13] Christensen J, Newman J. A mathematical model of stress generation and fracture in lithium manganese oxide. Journal of the Electrochemical Society 2006; 153: A1019.

[14] Zhang XC, Sastry AM, Shyy W. Intercalation-induced stress and heat generation within single lithium-ion battery cathode particles. Journal of the Electrochemical Society 2008; 155: A542.

[15] Hu YH, Zhao XH, Suo ZG. Averting cracks caused by insertion reaction in lithium-ion batteries. Journal of Materials Research 2010; 25: 1007.

[16] Zhao KJ, Pharr M, Vlassak JJ, Suo ZG. Fracture of electrodes in lithium-ion batteries caused by fast charging. Journal of Applied Physics 2010; 108: 073517.

[17] Beaulieu LY, Eberman KW, Turner RL, Krause LJ, Dahn JR. Colossal reversible volume changes in lithium alloys. Electrochemical and Solid State Letters 2001; 4: A137.

[18] Wang HF, Jang YI, Huang BY, Sadoway DR, Chiang YT. TEM study of electrochemical cycling-induced damage and disorder in LiCoO2 cathodes for rechargeable lithium batteries. Journal of the Electrochemical Society 1999; 146: 473.

[19] Wang DY, Wu XD, Wang ZX, Chen LQ. Cracking causing cyclic instability of LiFePO4 cathode material. Journal of Power Sources 2005; 140: 125.

[20] Takamura T, Ohara S, Uehara M, Suzuki J, Sekine K. A vacuum deposited Si

film having a Li extraction capacity over 2000 mAh/g with a long cycle life. Journal of Power Sources 2004; 129: 96.

[21] Chan CK, Peng HL, Liu G, McIlwrath K, Zhang XF, Huggins RA, Cui Y. High-performance lithium battery anodes using silicon nanowires. Nature Nanotechnology 2008; 3: 31.

[22] Arora P, White RE, Doyle M. Capacity fade mechanisms and side reactions in lithium-ion batteries. Journal of the Electrochemical Society 1998; 145: 3647.

[23] Kasavajjula U, Wang CS, Appleby AJ. Nano- and bulk-silicon-based insertion anodes for lithium-ion secondary cells. Journal of Power Sources 2007; 163: 1003.

[24] Zhang WJ. A review of the electrochemical performance of alloy anodes for lithium-ion batteries. Journal of Power Sources 2011; 196: 13.

[25] Zhang WJ. Lithium insertion/extraction mechanism in alloy anodes for lithium-ion batteries. Journal of Power Sources 2011; 196: 877.

[26] Haftbaradaran H, Gao HJ, Curtin WA. A surface locking instability for atomic intercalation into a solid electrode. Applied Physics Letters 2010; 96: 091909

[27] Haftbaradaran H, Song J, Curtin WA, Gao HJ. Continuum and atomistic models of strongly coupled diffusion, stress, and solute concentration. Journal of Power Sources 2011; 196: 361.

[28] Tang M, Belak JF, Dorr MR. Anisotropic Phase Boundary Morphology in Nanoscale Olivine Electrode Particles. Journal of Physical Chemistry C 2011; 115: 4922.

[29] Nazri GA, Pistoia G., Lithium Batteries, Springer, 2003.

[30] Lazarraga MG, Mandal S, Ibanez J, Amarilla JM, Rojo JM. LiMn2O4-based composites processed by a chemical-route microstructural, electrical, electrochemical, and mechanical characterization. Journal of Power Sources 2003; 115: 315.

[31] Chen GY, Song XY, Richardson TJ. Electron microscopy study of the LiFePO4 to FePO4 phase transition. Electrochemical and Solid State Letters 2006; 9: A295.

[32] Gabrisch H, Wilcox J, Doeff MM. TEM study of fracturing in spherical and plate-like LiFePO4 particles. Electrochemical and Solid State Letters 2008; 11: A25.

[33] Wilson JR, Cronin JS, Barnett SA, Harris SJ. Measurement of three-dimensional microstructure in a LiCoO2 positive electrode. Journal of Power Sources 2011; 196: 3443.

[34] Cheng YT, Verbrugge MW. The influence of surface mechanics on diffusion induced stresses within spherical nanoparticles. Journal of Applied Physics 2008; 104: 083521.

[35] Cheng YT, Verbrugge MW. Evolution of stress within a spherical insertion electrode particle under potentiostatic and galvanostatic operation. Journal of Power Sources 2009; 190: 453.

[36] Deshpande R, Cheng YT, Verbrugge MW. Modeling diffusion-induced stress in nanowire electrode structures. Journal of Power Sources 2010; 195: 5081.

[37] Golmon S, Maute K, Lee SH, Dunn ML. Stress generation in silicon particles during lithium insertion. Applied Physics Letters 2010; 97: 033111.

[38] Cheng YT, Verbrugge MW. Diffusion-Induced Stress, Interfacial Charge Transfer, and Criteria for Avoiding Crack Initiation of Electrode Particles. Journal of the Electrochemical Society 2010; 157: A508.

[39] Woodford WH, Chiang Y-M, Carter WC. "Electrochemical Shock" of Intercalation Electrodes: A Fracture Mechanics Analysis. Journal of the Electrochemical Society 2010; 157: A1052.

[40] Bhandakkar TK, Gao HJ. Cohesive modeling of crack nucleation under diffusion induced stresses in a thin strip: Implications on the critical size for flaw tolerant battery electrodes. International Journal of Solids and Structures 2010; 47: 1424.

[41] Bhandakkar TK, Gao HJ. Cohesive modeling of crack nucleation in a cylindrical electrode under axisymmetric diffusion induced stresses. International Journal of Solids and Structures 2011; 48: 2304.

[42] Evans AG. Microfracture from Thermal-Expansion Anisotropy .1. Single-Phase Systems. Acta Metallurgica 1978; 26: 1845.

[43] Lu TC, Yang J, Suo Z, Evans AG, Hecht R, Mehrabian R. Matrix Cracking in Intermetallic Composites Caused by Thermal-Expansion Mismatch. Acta Metallurgica Et Materialia 1991; 39: 1883.

[44] Hutchinson JW, Suo Z. Mixed-Mode Cracking in Layered Materials. Advances in Applied Mechanics 1991; 29: 63.

[45] Jo M, Hong YS, Choo J, Cho J. Effect of LiCoO2 Cathode Nanoparticle Size on High Rate Performance for Li-Ion Batteries. Journal of the Electrochemical Society 2009; 156: A430.

[46] Wang Y, Cao GZ. Developments in nanostructured cathode materials for high-performance lithium-ion batteries. Advanced Materials 2008; 20: 2251.

[47] Reimers JN, Dahn JR. Electrochemical and Insitu X-Ray-Diffraction Studies of Lithium Intercalation in Li_xCoO_2. Journal of the Electrochemical Society 1992; 139: 2091.

[48] Xie J, Imanishi N, Matsumura T, Hirano A, Takeda Y, Yamamoto O. Orientation dependence of Li-ion diffusion kinetics in LiCoO2 thin films prepared by RF magnetron sputtering. Solid State Ionics 2008; 179: 362.

[49] Hart FX, Bates JB. Lattice model calculation of the strain energy density and other properties of crystalline $LiCoO_2$. Journal of Applied Physics 1998; 83: 7560.

[50] Shenoy VB, Johari P, Qi Y. Elastic softening of amorphous and crystalline Li-Si Phases with increasing Li concentration: A first-principles study. Journal of Power Sources 2010; 195: 6825.

[51] Kim H, Han B, Choo J, Cho J. Three-Dimensional Porous Silicon Particles for Use in High-Performance Lithium Secondary Batteries. Angewandte Chemie-International Edition 2008; 47: 10151.

[52] Sethuraman VA, Chon MJ, Shimshak M, Srinivasan V, Guduru PR. In situ measurements of stress evolution in silicon thin films during electrochemical

lithiation and delithiation. Journal of Power Sources 2010; 195: 5062.

[53] Freund LB, Suresh S. Thin film materials. Cambridge University Press, Cambridge. 2003.

[54] Maranchi JP, Hepp AF, Evans AG, Nuhfer NT, Kumta PN. Interfacial properties of the a-Si/Cu : active-inactive thin-film anode system for lithium-ion batteries. Journal of the Electrochemical Society 2006; 153: A1246.

[55] Duduta M, Ho B, Wood VC, Limthongkul P, Brunini VE, Carter WC, Chiang YM. Semi-Solid Lithium Rechargeable Flow Battery. Advanced Energy Materials 2011; 1: 511.

[56] Bradwell DJ, Kim H, Sirk AHC, Sadoway DR. Magnesium-Antimony Liquid Metal Battery for Stationary Energy Storage. Journal of the American Chemical Society 2012; 134: 1895.

[57] Deshpande RD, Li JC, Cheng YT, Verbrugge MW. Liquid Metal Alloys as Self-Healing Negative Electrodes for Lithium Ion Batteries. Journal of the Electrochemical Society 2011; 158: A845.

[58] Hill R. The Mathematical Theory of Plasticity. Oxford University Press, 1950.

[59] Ding N, Xu J, Yao YX, Wegner G, Fang X, Chen CH, Lieberwirth I. Determination of the diffusion coefficient of lithium ions in nano-Si. Solid State Ionics 2009; 180: 222.

[60] Boukamp BA, Lesh GC, Huggins RA. All-Solid Lithium Electrodes with Mixed-Conductor Matrix. Journal of the Electrochemical Society 1981; 128: 725.

[61] Zhao KJ, Pharr M, Vlassak JJ, Suo ZG. Inelastic hosts as electrodes for high-capacity lithium-ion batteries. Journal of Applied Physics 2011; 109: 016110.

[62] Sethuraman VA, Srinivasan V, Bower AF, Guduru PR. In Situ Measurements of Stress-Potential Coupling in Lithiated Silicon. Journal of the Electrochemical Society 2010; 157: A1253.

[63] Lee EH. Elastic-Plastic Deformation at Finite Strains. Journal of Applied Mechanics 1969; 36: 1.

[64] Silberstein MN, Boyce MC. Constitutive modeling of the rate, temperature, and hydration dependent deformation response of Nafion to monotonic and cyclic loading. Journal of Power Sources 2010; 195: 5692.

[65] Ben Amar M, Goriely A. Growth and instability in elastic tissues. Journal of the Mechanics and Physics of Solids 2005; 53: 2284.

[66] Zhao KJ, Wang WL, Gregoire J, Pharr M, Suo ZG, Vlassak JJ, Kaxiras E. Lithium-Assisted Plastic Deformation of Silicon Electrodes in Lithium-Ion Batteries: A First-Principles Theoretical Study. Nano Letters 2011; 11: 2962.

[67] Choi JW, McDonough J, Jeong S, Yoo JS, Chan CK, Cui Y. Stepwise Nanopore Evolution in One-Dimensional Nanostructures. Nano Letters 2010; 10: 1409.

[68] Choi NS, Yao Y, Cui Y, Cho J. One dimensional Si/Sn - based nanowires and nanotubes for lithium-ion energy storage materials. Journal of Materials Chemistry 2011; 21: 9825.

[69] Haftbaradaran H, Xiao XC, Verbrugge MW, Gao HJ. Method to deduce the

critical size for interfacial delamination of patterned electrode structures and application to lithiation of thin-film silicon islands. Journal of Power Sources 2012; 206: 357.

[70] Yu CJ, Li X, Ma T, Rong JP, Zhang RJ, Shaffer J, An YH, Liu Q, Wei BQ, Jiang HQ. Silicon Thin Films as Anodes for High-Performance Lithium-Ion Batteries with Effective Stress Relaxation. Advanced Energy Materials 2012; 2: 68.

[71] Soni SK, Sheldon BW, Xiao XC, Verbrugge MW, Ahn D, Haftbaradaran H, Gao HJ. Stress Mitigation during the Lithiation of Patterned Amorphous Si Islands. Journal of the Electrochemical Society 2012; 159: A38.

[72] Yao Y, McDowell MT, Ryu I, Wu H, Liu NA, Hu LB, Nix WD, Cui Y. Interconnected Silicon Hollow Nanospheres for Lithium-Ion Battery Anodes with Long Cycle Life. Nano Letters 2011; 11: 2949.

[73] McDowell MT, Lee SW, Ryu I, Wu H, Nix WD, Choi JW, Cui Y. Novel Size and Surface Oxide Effects in Silicon Nanowires as Lithium Battery Anodes. Nano Letters 2011; 11: 4018.

[74] Hertzberg B, Alexeev A, Yushin G. Deformations in Si-Li Anodes Upon Electrochemical Alloying in Nano-Confined Space. Journal of the American Chemical Society 2010; 132: 8548.

[75] Xiao XC, Lu P, Ahn D. Ultrathin Multifunctional Oxide Coatings for Lithium Ion Batteries. Advanced Materials 2011; 23: 3911.

[76] Chen HX, Xiao Y, Wang L, Yang Y. Silicon nanowires coated with copper layer as anode materials for lithium-ion batteries. Journal of Power Sources 2011;

196: 6657.

[77] Liu Y, Hudak NS, Huber DL, Limmer SJ, Sullivan JP, Huang JY. In Situ Transmission Electron Microscopy Observation of Pulverization of Aluminum Nanowires and Evolution of the Thin Surface Al2O3 Layers during Lithiation-Delithiation Cycles. Nano Letters 2011; 11: 4188.

[78] He Y, Yu XQ, Wang YH, Li H, Huang XJ. Alumina-Coated Patterned Amorphous Silicon as the Anode for a Lithium-Ion Battery with High Coulombic Efficiency. Advanced Materials 2011; 23: 4938.

[79] Leung K, Qi Y, Zavadil KR, Jung YS, Dillon AC, Cavanagh AS, Lee SH, George SM. Using Atomic Layer Deposition to Hinder Solvent Decomposition in Lithium Ion Batteries: First-Principles Modeling and Experimental Studies. Journal of the American Chemical Society 2011; 133: 14741.

[80] Choi NS, Yew KH, Lee KY, Sung M, Kim H, Kim SS. Effect of fluoroethylene carbonate additive on interfacial properties of silicon thin-film electrode. Journal of Power Sources 2006; 161: 1254.

[81] Hu YS, Demir-Cakan R, Titirici MM, Muller JO, Schlogl R, Antonietti M, Maier J. Superior storage performance of a Si@SiOx/C nanocomposite as anode material for lithium-ion batteries. Angewandte Chemie-International Edition 2008; 47: 1645.

[82] Chan CK, Ruffo R, Hong SS, Cui Y. Surface chemistry and morphology of the solid electrolyte interphase on silicon nanowire lithium-ion battery anodes. Journal of Power Sources 2009; 189: 1132.

[83] Holzapfel M, Buqa H, Scheifele W, Novak P, Petrat FM. A new type of nano-sized silicon/carbon composite electrode for reversible lithium insertion. Chemical Communications 2005: 1566.

[84] Holzapfel M, Buqa H, Krumeich F, Novak P, Petrat FM, Veit C. Chemical vapor deposited silicon/graphite compound material as negative electrode for lithium-ion batteries. Electrochemical and Solid State Letters 2005; 8: A516.

[85] Wu H, Chan G, Choi JW, Ryu I, Yao Y, McDowell MT, Lee SW, Jackson A, Yang Y, Hu L, Cui Y. Nat. Nanotechnol (2012), DOI: 10.1038/NNANO.2012.35.

[86] Wu H, Zheng GY, Liu NA, Carney TJ, Yang Y, Cui Y. Engineering Empty Space between Si Nanoparticles for Lithium-Ion Battery Anodes. Nano Letters 2012; 12: 904.

[87] Hwang TH, Lee YM, Kong BS, Seo JS, Choi JW. Electrospun Core-Shell Fibers for Robust Silicon Nanoparticle-Based Lithium Ion Battery Anodes. Nano Letters 2012; 12: 802.

[88] Li X, Meduri P, Chen X, Qi W, Engelhard MH, Xu W, Ding F, Xiao J, Wang W, Wang C, Zhang J, Liu J. J. Mater. Chem. (2012) DOI: 10.1039/c0xx00000x.

[89] Timoshenko S, Goodier JN. Theory of Elasticity, 3rd Edition. Mcgraw-Hill College, Blacklick, OH. 1970.

[90] Zhao KJ, Pharr M, Cai SQ, Vlassak JJ, Suo ZG. Large Plastic Deformation in High-Capacity Lithium-Ion Batteries Caused by Charge and Discharge. Journal of the American Ceramic Society 2011; 94: S226.

[91] Hertzberg B, Benson J, Yushin G. Ex-situ depth-sensing indentation

measurements of electrochemically produced Si-Li alloy films. Electrochemistry Communications 2011; 13: 818.

[92] Sethuraman VA, Chon MJ, Shimshak M, Van Winkle N, Guduru PR. In situ measurement of biaxial modulus of Si anode for Li-ion batteries. Electrochemistry Communications 2010; 12: 1614.

[93] http://accuratus.com/alumox.html.

[94] Cui ZQ, Gao F, Qu JM. A finite deformation stress-dependent chemical potential and its applications to lithium ion batteries. Journal of the Mechanics and Physics of Solids 2012; 60: 1280.

[95] Limthongkul P, Jang YI, Dudney NJ, Chiang YM. Electrochemically-driven solid-state amorphization in lithium-silicon alloys and implications for lithium storage. Acta Materialia 2003; 51: 1103.

[96] Xun S, Song X, Wang L, Grass ME, Liu Z, Battaglia VS, Liu G. The Effects of Native Oxide Surface Layer on the Electrochemical Performance of Si Nanoparticle-Based Electrodes. Journal of the Electrochemical Society 2011; 158: A1260.

[97] Arico AS, Bruce P, Scrosati B, Tarascon JM, Van Schalkwijk W. Nanostructured materials for advanced energy conversion and storage devices. Nature Materials 2005; 4: 366.

[98] Li H, Wang ZX, Chen LQ, Huang XJ. Research on Advanced Materials for Li-ion Batteries. Advanced Materials 2009; 21: 4593.

[99] Pitchai R, Thavasi V, Mhaisalkar SG, Ramakrishna S. Nanostructured cathode

materials: a key for better performance in Li-ion batteries. Journal of Materials Chemistry 2011; 21: 11040.

[100] Liu XH, Zhong L, Huang S, Mao SX, Zhu T, Huang JY. Size-Dependent Fracture of Silicon Nanoparticles During Lithiation. Acs Nano 2012; 6: 1522.

[101] Ryu I, Choi JW, Cui Y, Nix WD. Size-dependent fracture of Si nanowire battery anodes. Journal of the Mechanics and Physics of Solids 2011; 59: 1717.

[102] Lee SW, McDowell MT, Berla LA, Nix WD, Cui Y. Fracture of crystalline silicon nanopillars during electrochemical lithium insertion. Proceedings of the National Academy of Sciences of the United States of America 2012; 109: 4080.

[103] Magasinski A, Dixon P, Hertzberg B, Kvit A, Ayala J, Yushin G. High-performance lithium-ion anodes using a hierarchical bottom-up approach. Nature Materials 2010; 9: 353.

[104] Cui LF, Ruffo R, Chan CK, Peng HL, Cui Y. Crystalline-Amorphous Core-Shell Silicon Nanowires for High Capacity and High Current Battery Electrodes. Nano Letters 2009; 9:4 91.

[105] Notten PHL, Roozeboom F, Niessen RAH, Baggetto L. 3-D integrated all-solid-state rechargeable batteries. Advanced Materials 2007; 19: 4564.

[106] Baggetto L, Niessen RAH, Roozeboom F, Notten PHL. High energy density all-solid-state batteries: A challenging concept towards 3D integration. Advanced Functional Materials 2008; 18: 1057.

[107] Choi JW, Hu LB, Cui LF, McDonough JR, Cui Y. Metal current collector-free freestanding silicon-carbon 1D nanocomposites for ultralight anodes in lithium

ion batteries. Journal of Power Sources 2010; 195: 8311.

[108] Obrovac MN, Christensen L, Le DB, Dahnb JR. Alloy design for lithium-ion battery anodes. Journal of the Electrochemical Society 2007; 154: A849.

[109] Cui LF, Yang Y, Hsu CM, Cui Y. Carbon-Silicon Core-Shell Nanowires as High Capacity Electrode for Lithium Ion Batteries. Nano Letters 2009; 9: 3370.

[110] Si Q, Hanai K, Imanishi N, Kubo M, Hirano A, Takeda Y, Yamamoto O. Highly reversible carbon-nano-silicon composite anodes for lithium rechargeable batteries. Journal of Power Sources 2009; 189: 761.

[111] Cui LF, Hu LB, Choi JW, Cui Y. Light-Weight Free-Standing Carbon Nanotube-Silicon Films for Anodes of Lithium Ion Batteries. Acs Nano 2010; 4: 3671.

[112] Lu ZW, Zhang LQ, Liu XJ. Microstructure and electrochemical performance of Si-SiO2-C composites as the negative material for Li-ion batteries. Journal of Power Sources 2010; 195: 4304.

[113] Hu LB, Wu H, Gao YF, Cao AY, Li HB, McDough J, Xie X, Zhou M, Cui Y. Silicon-Carbon Nanotube Coaxial Sponge as Li-Ion Anodes with High Areal Capacity. Advanced Energy Materials 2011; 1: 523.

[114] Obrovac MN, Christensen L. Structural changes in silicon anodes during lithium insertion/extraction. Electrochemical and Solid State Letters 2004; 7: A93.

[115] Hatchard TD, Dahn JR. In situ XRD and electrochemical study of the reaction of lithium with amorphous silicon. Journal of the Electrochemical Society 2004;

151: A838.

[116] Liu XH, Zhang LQ, Zhong L, Liu Y, Zheng H, Wang JW, Cho JH, Dayeh SA, Picraux ST, Sullivan JP, Mao SX, Ye ZZ, Huang JY. Ultrafast Electrochemical Lithiation of Individual Si Nanowire Anodes. Nano Letters 2011; 11: 2251.

[117] Huang JY, Zhong L, Wang CM, Sullivan JP, Xu W, Zhang LQ, Mao SX, Hudak NS, Liu XH, Subramanian A, Fan HY, Qi LA, Kushima A, Li J. In Situ Observation of the Electrochemical Lithiation of a Single SnO2 Nanowire Electrode. Science 2010; 330: 1515.

[118] Demczyk BG, Wang YM, Cumings J, Hetman M, Han W, Zettl A, Ritchie RO. Direct mechanical measurement of the tensile strength and elastic modulus of multiwalled carbon nanotubes. Materials Science and Engineering a-Structural Materials Properties Microstructure and Processing 2002; 334: 173.

[119] Chon MJ, Sethuraman VA, McCormick A, Srinivasan V, Guduru PR. Real-Time Measurement of Stress and Damage Evolution during Initial Lithiation of Crystalline Silicon. Physical Review Letters 2011; 107: 045503.

[120] Liu XH, Zheng H, Zhong L, Huan S, Karki K, Zhang LQ, Liu Y, Kushima A, Liang WT, Wang JW, Cho JH, Epstein E, Dayeh SA, Picraux ST, Zhu T, Li J, Sullivan JP, Cumings J, Wang CS, Mao SX, Ye ZZ, Zhang SL, Huang JY. Anisotropic Swelling and Fracture of Silicon Nanowires during Lithiation. Nano Letters 2011; 11: 3312.

[121] Lee SW, McDowell MT, Choi JW, Cui Y. Anomalous Shape Changes of Silicon Nanopillars by Electrochemical Lithiation. Nano Letters 2011; 11: 3034.

[122] Goldman JL, Long BR, Gewirth AA, Nuzzo RG. Strain Anisotropies and Self-Limiting Capacities in Single-Crystalline 3D Silicon Microstructures: Models for High Energy Density Lithium-Ion Battery Anodes. Advanced Functional Materials 2011; 21: 2412.

[123] Nye JF. Physical Properties of Crystals: Their Representation by Tensors and Matrices, Oxford University Press, New York. 1985.

[124] Subramanian VR, Ploehn HJ, White RE. Shrinking core model for the discharge of a metal hydride electrode. Journal of the Electrochemical Society 2000; 147: 2868.

[125] Subramanian VR, White RE. New separation of variables method for composite electrodes with galvanostatic boundary conditions. Journal of Power Sources 2001; 96: 385.

[126] Stephanie Golmon, Kurt Maute, Se-Hee Lee, Dunn ML. Stress generation in silicon particles during lithium insertion. Applied Physics Letters 2010; 97: 033111.

[127] Deshpande R, Cheng Y-T, Verbrugge MW, Timmons A. Diffusion Induced Stresses and Strain Energy in a Phase-Transforming Spherical Electrode Particle. Journal of the Electrochemical Society 2011; 158: A718.

[128] Wan WH, Zhang QF, Cui Y, Wang EG. First principles study of lithium insertion in bulk silicon. Journal of Physics-Condensed Matter 2010; 22: 415501.

[129] Bockris J O'M, Reddy AKN, Gamboa-Aldeco M. Modern Electrochemistry, Vol.

2A, Fundamentals of Electrodics, 2nd ed., Kluwer Academic/Plenum Publishers. 2000.

[130] Park MH, Kim MG, Joo J, Kim K, Kim J, Ahn S, Cui Y, Cho J. Silicon Nanotube Battery Anodes. Nano Letters 2009; 9: 3844.

[131] Krishnan R, Lu TM, Koratkar N. Functionally Strain-Graded Nanoscoops for High Power Li-Ion Battery Anodes. Nano Letters 2011; 11: 377.

[132] Song T, Xia JL, Lee JH, Lee DH, Kwon MS, Choi JM, Wu J, Doo SK, Chang H, Il Park W, Zang DS, Kim H, Huang YG, Hwang KC, Rogers JA, Paik U. Arrays of Sealed Silicon Nanotubes As Anodes for Lithium Ion Batteries. Nano Letters 2010; 10: 1710.

[133] Bower AF, Guduru PR, Sethuraman VA. A finite strain model of stress, diffusion, plastic flow, and electrochemical reactions in a lithium-ion half-cell. Journal of the Mechanics and Physics of Solids 2011; 59: 804.

[134] Deshpande R, Qi Y, Cheng YT. Effects of Concentration-Dependent Elastic Modulus on Diffusion-Induced Stresses for Battery Applications. Journal of the Electrochemical Society 2010; 157: A967.

[135] Chevrier VL, Dahn JR. First Principles Model of Amorphous Silicon Lithiation. Journal of the Electrochemical Society 2009; 156: A454.

[136] Huang S, Zhu T. Atomistic mechanisms of lithium insertion in amorphous silicon. Journal of Power Sources 2010; 196: 3664.

[137] Chou CY, Kim H, Hwang GS. A Comparative First-Principles Study of the Structure, Energetics, and Properties of Li-M (M = Si, Ge, Sn) Alloys. Journal of

Physical Chemistry C 2011; 115: 20018.

[138] Kim H, Chou CY, Ekerdt JG, Hwang GS. Structure and Properties of Li-Si Alloys: A First-Principles Study. Journal of Physical Chemistry C 2011; 115: 2514.

[139] Johari P, Qi Y, Shenoy VB. The Mixing Mechanism during Lithiation of Si Negative Electrode in Li-Ion Batteries: An Ab lnitio Molecular Dynamics Study. Nano Letters 2011; 11: 5494.

[140] Zhang QF, Zhang WX, Wan WH, Cui Y, Wang EG. Lithium Insertion In Silicon Nanowires: An ab Initio Study. Nano Letters 2010; 10: 3243.

[141] Jung SC, Han YK. Facet-dependent lithium intercalation into Si crystals: Si(100) vs. Si(111). Physical Chemistry Chemical Physics 2011; 13: 21282.

[142] Zhang QF, Cui Y, Wang EG. Anisotropic Lithium Insertion Behavior in Silicon Nanowires: Binding Energy, Diffusion Barrier, and Strain Effect. Journal of Physical Chemistry C 2011; 115: 9376.

[143] Ng MF, Sullivan MB, Tong SW, Wu P. First-Principles Study of Silicon Nanowire Approaching the Bulk Limit. Nano Letters 2011; 11: 4794.

[144] Soler JM, Artacho E, Gale JD, Garcia A, Junquera J, Ordejon P, Sanchez-Portal D. The SIESTA method for ab initio order-N materials simulation. Journal of Physics-Condensed Matter 2002; 14: 2745. We use the PBE exchange-correlation functional, norm-conserving pseudopotentials, and reciprocal-space mesh cutoff equivalent to a 20 Å (10 Å) real-space period for the crystalline (amorphous) supercell.

[145] Juan YM, Kaxiras E, Gordon RG. Use of the Generalized Gradient Approximation in Pseudopotential Calculations of Solids. Physical Review B 1995; 51: 9521.

[146] Tuttle B, Adams JB. Energetics of hydrogen in amorphous silicon: An ab initio study. Physical Review B 1998; 57: 12859.

[147] Farid B, Godby RW. Cohesive Energies of Crystals. Physical Review B 1991; 43: 14248.

[148] Bazant MZ, Kaxiras E, Justo JF. Environment-dependent interatomic potential for bulk silicon. Physical Review B 1997; 56: 8542.

[149] Mo Y, Bazant MZ, Kaxiras E. Sulfur point defects in crystalline and amorphous silicon. Physical Review B 2004; 70: 205210.

[150] Bruce PG, Freunberger SA, Hardwick LJ, Tarascon JM. Li-O-2 and Li-S batteries with high energy storage. Nature Materials 2012; 11: 19.

[151] Soni SK, Sheldon BW, Xiao XC, Tokranov A. Thickness effects on the lithiation of amorphous silicon thin films. Scripta Materialia 2010; 64: 307.

[152] Pyun SI, Go JY, Jang TS. An investigation of intercalation-induced stresses generated during lithium transport through $Li_{1-\delta}CoO2$ film electrode using a laser beam deflection method. Electrochimica Acta 2004; 49: 4477.

[153] Oh J, Thompson CV. The role of electric field in pore formation during aluminum anodization. Electrochimica Acta 2011; 56: 4044.

[154] Ulm FJ, Coussy O, Li KF, Larive C. Thermo-chemo-mechanics of ASR expansion in concrete structures. Journal of Engineering Mechanics-Asce 2000;

126: 233.

[155] Brassart L, Suo ZG. Submitted for publication. 2012.

[156] McAuthur M. A. An in-situ investigation of solid electrolyte interphase formation on electrode materials for lithium-ion batteries using spectroscopic ellipsometry. Thesis for the Degree of Master of Science, Dalhousie University, 2011.

[157] Ohzuku T, Tomura H, Sawai K. Monitoring of particle fracture by acoustic emission during charge and discharge of $LiMnO_2$ cells. Journal of the Electrochemical Society 1997; 144: 3496.

[158] Zheng GY, Yang Y, Cha JJ, Hong SS, Cui Y. Hollow Carbon Nanofiber-Encapsulated Sulfur Cathodes for High Specific Capacity Rechargeable Lithium Batteries. Nano Letters 2011; 11: 4462.

[159] Kim SW, Seo DH, Ma XH, Ceder G, Kang K. Electrode materials for rechargeable sodium-ion batteries: potential alternatives to current lithium-ion batteries. Advanced Energy Materials 2012 DOI: 10.1002/aenm.201200026.

[160] Slater MD, Kim DH, Lee E, Johnson CS. Sodium-ion batteries. Advanced Functional Materials 2012 DOI: 10.1002/adfm.201200691.

Appendix

Appendix A: Notes on numerical procedure of large plastic deformation caused by charge and discharge

We rewrite the governing equations in the form used in our numerical simulation. It has been assumed that neither elastic nor plastic deformation causes any volumetric change. It has been also assumed that Ω is a constant. Consequently, the volumetric change of a material element is

$$\lambda_r \lambda_\theta^2 = 1 + \Omega C . \tag{A1}$$

A combination of (A1), (4. 19) and (4. 20) gives that

$$r(R,t) = \left[3\int_0^R (1+\Omega C) R^2 dR \right]^{1/3} . \tag{A2}$$

Here we have used a condition due to the spherical symmetry of the problem, $r(0,t) = 0$.

The kinetic model (4. 25) can be written in terms of the nominal quantities:

$$J = -\frac{CD}{kT\lambda_r^2} \frac{\partial \mu(R,t)}{\partial R} . \tag{A3}$$

A combination of (A3) and (4. 24) gives

$$J = -\frac{CD}{(1+\Omega C)^2} \left(\frac{r}{R} \right)^4 \frac{\partial}{\partial R} \left[\log \frac{\gamma C}{1+\Omega C} - \frac{\Omega(\sigma_r + 2\sigma_\theta)}{3kT} \right] \tag{A4}$$

Recall that the flux satisfies the boundary conditions $J(0,t) = 0$ and $J(A,t) = \pm J_0$. The sign of the latter condition depends on whether the particle is being charged or discharged.

The stress $(\sigma_\theta - \sigma_r)$ and the plastic stretch evolve according to the ideal

elastic-plastic model, Figure 4. 3 (b). When $|\sigma_r - \sigma_\theta| < \sigma_Y$, the plastic stretch λ_r^p remains fixed, and the elastic stretch is given by $\log \lambda_r^e = (\sigma_r - \sigma_\theta)/E$, which is written as

$$\sigma_r - \sigma_\theta = E \log\left(\Lambda^{-1/3} \lambda_r / \lambda_r^p\right). \tag{A5}$$

When $\sigma_r - \sigma_\theta = \pm\sigma_Y$, the elastic stretch is fixed at $\log \lambda_r^e = \pm\sigma_Y / E$, and the plastic stretch adopts a value

$$\lambda_r^p = \lambda_r \Lambda^{-1/3} \exp\left(\mp \frac{\sigma_Y}{E}\right). \tag{A6}$$

Integrating (4. 23), we obtain that

$$\sigma_r(R,t) = 2\int_A^R \frac{(\sigma_r - \sigma_\theta)(1+\Omega C)R^2}{r^3} dR \tag{A7}$$

Here we have used the boundary condition $\sigma_r(A,t) = 0$.

We use the finite difference method, and divide the interval $0 \le R \le A$ into small elements. The initial condition $C(R,0)$ is prescribed; for example, we set $C(R,0) = 0$ to simulate the process of lithiation, and set $C(R,0) = C_{\max}$ to simulate the process of delithiation. The initial values of the function $J(R,0)$ are set with $J(0,0) = 0$ and $J(A,0) = \pm J_0$ at the boundaries, and $J(R,0) = 0$ at the interior points. We then evolve all functions with a time step Δt. At a given time t, the functions $C(R,t)$ and $J(R,t)$, along with the boundary conditions $J(0,t) = 0$ and $J(A,t) = \pm J_0$, are inserted into (4. 21) to calculate $C(R,t+\Delta t)$. The result is then inserted into (A2) to calculate $r(R,t+\Delta t)$. The field $\sigma_r(R,t+\Delta t)$ is calculated by the integrating (A7), where $(\sigma_\theta - \sigma_r)$ is determined by the uniaxial stress-strain relation. We then calculate $J(R,t+\Delta t)$ by using (A4). This procedure is repeated for the next time step to evolve the fields.

Appendix B: Stresses in coated-hollow Si nanowires

We derive the stress field in a hollow silicon nanowire coated with a stiff shell. The geometry of the cross section is represented in Figure 5. 3. We represent a material element in the reference configuration, Figure 5. 3 (a), by its distance *R* from the center. At time *t*, it moves to a place at a distance *r* from the center, Figure 5. 3 (b). The function *r(R, t)* specifies the deformation kinematics of the silicon nanowire. Due to the constraint imposed by the shell, lithiated silicon is assumed to deform under the plane-strain conditions. To focus on the main ideas, we neglect the elasticity of both the core and the shell; we model the lithiated silicon as a rigid-plastic material. Consequently, the expansion of lithiated silicon is entirely due to lithiation. Consider an annulus of the lithiated silicon between the radii *B* and *r*. This annulus is lithiated from the annulus of pristine silicon between the radii *B* and *R*. We assume that the rate of lithiation is slow relative to diffusion of Li in the core, so that Li atoms have enough time to homogenize in the core. That is, the ratio of the volume of the lithiated silicon over the volume of pristine silicon $\tilde{\beta}$, is taken to be homogeneous and evolves in time. Upon full lithiation, $\tilde{\beta}$ reaches $\beta = 4$ for silicon. Thus,

$$B^2 - r^2 = \tilde{\beta}\left(B^2 - R^2\right), \tag{B1}$$

This equation gives the function *r(R, t)* once the function $\tilde{\beta}(t)$ is given. That is, $\tilde{\beta}(t)$ fully specifies the kinematics of the silicon nanowire,

$$r = \sqrt{B^2 - \tilde{\beta}\left(B^2 - R^2\right)}. \tag{B2}$$

The stretches can be calculated as

$$\lambda_r = \frac{\partial r}{\partial R} = \frac{R\tilde{\beta}}{r}, \quad \lambda_\theta = \frac{r}{R}, \quad \lambda_z = 1, \tag{B3}$$

We decompose the stretches by writing

$$\lambda_r = \lambda_r^p \tilde{\beta}^{1/3}, \quad \lambda_\theta = \lambda_\theta^p \tilde{\beta}^{1/3}, \quad \lambda_z = \lambda_z^p \tilde{\beta}^{1/3} \tag{B4}$$

where $\tilde{\beta}$ represents the volume change due to the insertion of Li, and the plastic stretch λ^p represents the shape change during lithiation. The volume change has been assumed to be isotropic for amorphous silicon. We can calculate the strain components from the stretches,

$$\varepsilon_r = \log \lambda_r, \quad \varepsilon_\theta = \log \lambda_\theta, \quad \varepsilon_z = \log \lambda_z \tag{B5}$$

The incremental plastic deformation is given by

$$\begin{aligned}
\delta\varepsilon_r^p &= \delta \log \lambda_r - \frac{1}{3}\delta \log \tilde{\beta} = \left(\frac{1}{6} + \frac{1}{2}\frac{B^2}{r^2}\right)\frac{\delta\tilde{\beta}}{\tilde{\beta}}, \\
\delta\varepsilon_\theta^p &= \delta \log \lambda_\theta - \frac{1}{3}\delta \log \tilde{\beta} = \left(\frac{1}{6} - \frac{1}{2}\frac{B^2}{r^2}\right)\frac{\delta\tilde{\beta}}{\tilde{\beta}}, \\
\delta\varepsilon_z^p &= \delta \log \lambda_z - \frac{1}{3}\delta \log \tilde{\beta} = -\frac{1}{3}\frac{\delta\tilde{\beta}}{\tilde{\beta}}
\end{aligned} \tag{B6}$$

The equivalent plastic strain is

$$\delta\varepsilon_{eq}^p = \sqrt{\frac{2}{3}\delta\varepsilon_{ij}^p \delta\varepsilon_{ij}^p} = \frac{\delta\tilde{\beta}}{\tilde{\beta}}\sqrt{\frac{1}{9} + \frac{1}{3}\frac{B^4}{r^4}}. \tag{B7}$$

We adopt the flow rule

$$s_{ij} = \frac{2}{3}\frac{\sigma_Y}{\delta\varepsilon_{eq}^p}\delta\varepsilon_{ij}^p, \tag{B8}$$

where s_{ij} is the deviatoric stress, defined as $s_{ij} = \sigma_{ij} - \frac{1}{3}\sigma_{ii}\delta_{ij}$, and σ_Y the yield strength of lithiated silicon. Therefore,

$$
\begin{aligned}
s_r &= \frac{\sigma_Y}{\sqrt{\frac{1}{9}+\frac{1}{3}\frac{B^4}{r^4}}}\left(\frac{1}{9}+\frac{1}{3}\frac{B^2}{r^2}\right), \\
s_\theta &= \frac{\sigma_Y}{\sqrt{\frac{1}{9}+\frac{1}{3}\frac{B^4}{r^4}}}\left(\frac{1}{9}-\frac{1}{3}\frac{B^2}{r^2}\right), \quad , \\
s_z &= -\frac{2}{9}\frac{\sigma_Y}{\sqrt{\frac{1}{9}+\frac{1}{3}\frac{B^4}{r^4}}}
\end{aligned}
\tag{B9}
$$

and

$$
\sigma_r - \sigma_\theta = s_r - s_\theta = \frac{2\sigma_Y}{\sqrt{r^4/B^4+3}} \quad . \tag{B10}
$$

Consider the force balance of a material element in lithiated silicon

$$
\frac{\partial \sigma_r}{\partial r} + \frac{\sigma_r - \sigma_\theta}{r} = 0 , \tag{B11}
$$

the radial stress can be obtained by integrating Eq. (B11), it gives

$$
\sigma_r = -\frac{\sqrt{3}}{3}\sigma_Y \log\frac{\sqrt{r^4+3B^4}-\sqrt{3}B^2}{r^2} + D, \qquad a \le r \le B \tag{B12}
$$

where D is the integration constant. With the traction-free boundary condition, $\sigma_r(a,\ t) = 0$,

$$
\sigma_r = -\frac{\sqrt{3}}{3}\sigma_Y\left(2\log\frac{a}{r} + \log\frac{\sqrt{r^4+3B^4}-\sqrt{3}B^2}{\sqrt{a^4+3B^4}-\sqrt{3}B^2}\right), \qquad a \le r \le B \tag{B13}
$$

The stresses along hoop and axial directions are obtained from Eq. (B10) and (B9),

$$
\begin{aligned}
\sigma_\theta &= \sigma_r - \frac{2\sigma_Y}{\sqrt{r^4/B^4+3}} \\
\sigma_z &= \sigma_r - \frac{\sigma_Y}{\sqrt{r^4/B^4+3}} - \frac{\sigma_Y}{\sqrt{3B^4/r^4+1}},
\end{aligned}
\tag{B14}
$$

Therefore the radial stress at the interface $r = B$ is given by,

$$
\sigma_r = -\frac{\sqrt{3}}{3}\sigma_Y\left(2\log\frac{a}{B} + \log\frac{\left(2-\sqrt{3}\right)B^2}{\sqrt{a^4+3B^4}-\sqrt{3}B^2}\right). \tag{B15}
$$

In the fully lithiated state of a hollow silicon nanowire, $a \ll B$. The radial stress at the

interface can then be approximated by a Taylor expansion, which gives

$$\sigma_r \approx \frac{2\sqrt{3}}{3}\sigma_Y \log\frac{a}{B}. \tag{B16}$$

The stress field in the elastic shell can be solved using the familiar solution of Lamé problem,[89] it gives,

$$\begin{aligned}
\sigma_r &= -\frac{2\sqrt{3}}{3}\sigma_Y\left(\log\frac{a}{B}\right)\left(\frac{B^2}{C^2-B^2}\right)\left(1-\frac{C^2}{r^2}\right),\\
\sigma_\theta &= -\frac{2\sqrt{3}}{3}\sigma_Y\left(\log\frac{a}{B}\right)\left(\frac{B^2}{C^2-B^2}\right)\left(1+\frac{C^2}{r^2}\right), \qquad B<r\le C\\
\sigma_z &= -\frac{2\sqrt{3}}{3}\sigma_Y\left(\log\frac{a}{B}\right)\left(\frac{2\nu B^2}{C^2-B^2}\right).
\end{aligned} \tag{B17}$$

Similar to the analysis of a sphere, the energy release rate in the coating shell takes the following solution

$$G_f = \frac{8}{3}\frac{{\sigma_Y}^2}{E_s}\left(\log\frac{B}{a}\right)^2\left(\frac{B^2}{C^2-B^2}\right)^2\left(1+\frac{C^2}{B^2}\right)^2(C-B). \tag{B18}$$

During delithiation, the tensile radial stress in silicon at the interface becomes

$$\sigma_r \approx \frac{2\sqrt{3}}{3}\sigma_Y \log\frac{B}{a}. \tag{B19}$$

Thus, using Eq. (5. 14), the energy release rate for interfacial debonding takes the solution

$$G_d = \frac{4\pi}{3}\frac{{\sigma_Y}^2}{E_e}\left(\log\frac{B}{a}\right)^2(C-B). \tag{B20}$$

Appendix C: Supplemental figures for reactive flow in silicon electrodes assisted by the insertion of lithium

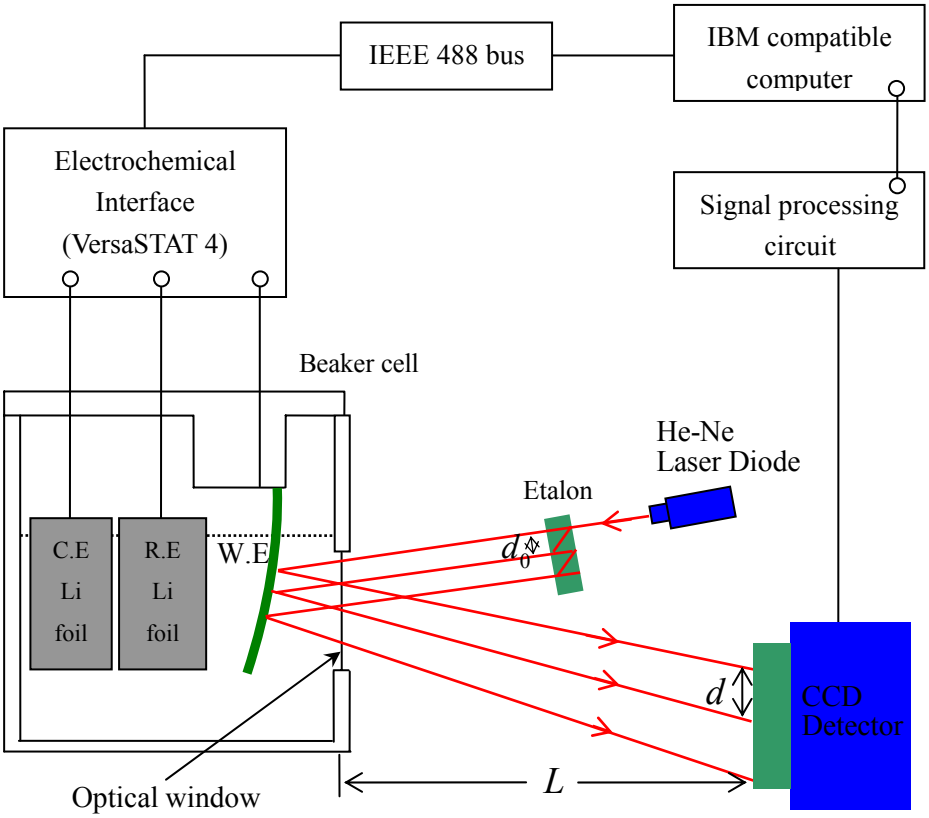

C. E.: counter electrode. R. E.: reference electrode. W. E.: working electrode
Electrolyte: 1$LiPF_6$ solution

Figure A. 1. A custom electrochemical cell with *in-situ* multi-beam stress sensor

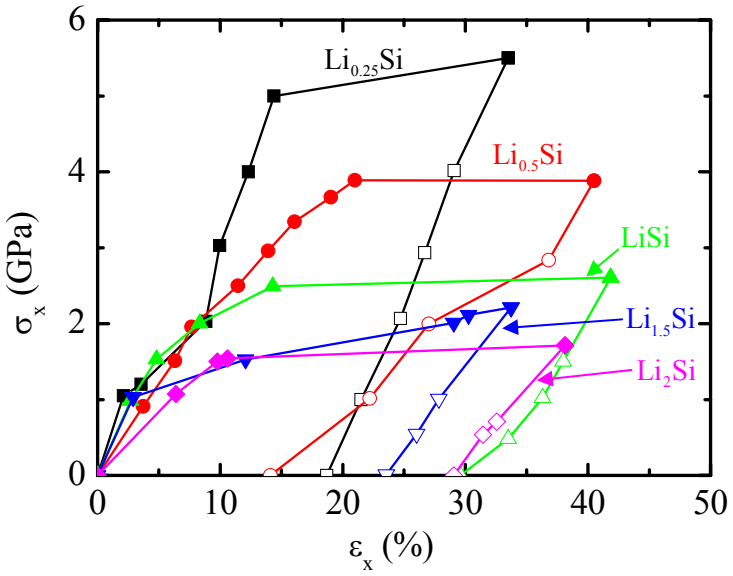

Figure A. 2. Stress-strain responses of lithiated a-Si under uniaxial tension with different Li concentrations.